

TRACING THE MAGMATIC TO HYDROTHERMAL EVOLUTION OF THE MOUNT ROSA COMPLEX,
COLORADO: TEXTURAL AND CHEMICAL EVIDENCE USING ZIRCON

by

Alyssa Smith

A thesis submitted to the Faculty and Board of Trustees of the Colorado School of Mines in partial fulfillment of the requirements for the degree of Master of Science (Geochemistry).

Golden, Colorado

Date _____

Signed: _____

Alyssa Smith

Signed: _____

Dr. Katharina Pfaff
Thesis Advisor

Golden, Colorado

Date _____

Signed: _____

Dr. M. Stephen Enders
Professor and Department Head
Department of Geology and Geological Engineering

ABSTRACT

Located ~15 km west of the city of Colorado Springs, the ~1.04 Ga Mount Rosa Complex (MRC) consists of a diverse groups of peraluminous to peralkaline granitic rocks hosted in the ~1.08 Ga Pikes Peak Batholith. From oldest to youngest, the MRC comprises the following rock units: the peraluminous Pikes Peak biotite granite (PPG), fayalite-bearing quartz syenite, granitic dikes, peralkaline Na-amphibole Mount Rosa granite (MRG), mafic dikes, and type-(I) and type-(II) NYF-type pegmatites. All rock units in the MRC are highly elevated in REEs and HFSEs compared to other A-type magmatic systems. In order to better understand the magmatic to hydrothermal evolution of the enigmatic MRC, zircons from each rock unit were analyzed using transmitted light microscopy, BSE imaging, EDS spot analyses, automated mineralogy bright phase searches, SEM-CL imaging, EMPA, and Raman spectroscopy to document their textural and chemical variations across all rock units.

Based on petrography and automated mineralogy, zircons were divided into 5 categories: Type 1A: euhedral early magmatic zircon, type 1B: early magmatic sieved textured zircon, type 1C: early magmatic patchy zircon, type 2: pegmatitic wallrock zircon, and type 3: hydrothermal zircon. Type 1A zircon occurs in the PPG, fayalite-bearing quartz syenite, and type-(I) pegmatites. Type 1A zircons exhibit concentric zoning and oftentimes have metamict zones. Type 1B zircon is isolated to certain areas of the MRG and is characterized by an abundance of large inclusions. Type 1C zircon is found in the granitic dikes, areas of the MRG where type 1B zircon is not found, and mafic dikes. Type 1C zircons display patchy erratic zoning and host small but abundant REE-bearing mineral inclusions. Type 2 zircons are mostly found in type-(II) pegmatite rims, and are inferred to be magmatic zircons with a hydrothermal overprint, causing unusual zoning. Type 3 zircons are found in the core of some type-(II) pegmatites, and are characterized as hydrothermal zircons that make up a complex array of vein networks. Contrary to prior suggestions, chemical and textural zircon data from all rock units within the complex suggests the peralkaline MRG is co-magmatic with the peraluminous PPG. Chemically, all zircon types display enrichment in REE and HFSE relative to mantle-derived zircons, with increasing enrichment in the younger rock units (mafic dikes, type-(I) pegmatites, and type-(II) pegmatites). Additionally, the zircons of the peraluminous granitic dikes are strikingly similar to the zircons of the peralkaline Mount Rosa granite and mafic dikes, proposing a similar origin.

Enrichment in REEs and HFSEs in the peraluminous PPG relative to other mantle derived magmas suggests its origin to be enriched mantle with potential crustal contamination during emplacement. As a result, the original peraluminous melt was rich in volatiles, alkalis, REEs and HFSEs. Fractional

crystallization of the melt caused the parental peraluminous melt to become enriched in volatiles and incompatible elements, resulting in the development of a peralkaline melt. The peralkaline granitic rocks differ mineralogically and can be described as a (I) early more primitive peralkaline mineral assemblage consisting of Na-Fe amphibole, albite, microcline, quartz, biotite, and sieve textured type 1B zircon and (II) a more evolved transitional peralkaline mineral assemblage with albite, microcline, quartz, F-rich biotite (siderophyllite), Na-Fe amphibole, fluorite, acicular astrophyllite, and patchy type 1C zircon. Type-(I) pegmatites, being mineralogically simple and very similar to the mineralogy of the MRG, are interpreted to represent the final melt of the (I) early primitive peralkaline melt. Type-(II) pegmatites, however, show a more evolved mineral assemblage that includes all minerals of type-(I) pegmatites, but also includes astrophyllite, monazite, and sulfides as well as complex fluorides such as cryolite, weberite, and Y-rich fluorite. Late stage aegirinization and Ca-F metasomatism is responsible for remobilizing and redistribution REEs and Zr (and other HFSE) throughout the MRC.

TABLE OF CONTENTS

ABSTRACT	iii
LIST OF FIGURES AND TABLES	vi
ACKNOWLEDGEMENTS	ix
CHAPTER 1: INTRODUCTION	1
1.1 Overview of Zircon	1
1.2 Overview of Pegmatites	3
1.3 Overview of Mount Rosa Pegmatites.....	6
1.4 Overview of Rare Earth and High Field Strength Elements.....	8
CHAPTER 2: TRACING THE MAGMATIC TO HYDROTHERMAL EVOLUTION OF THE MOUNT ROSA COMPLEX, COLORADO: TEXTURAL AND CHEMICAL EVIDENCE USING ZIRCON	10
2.1 Introduction.....	10
2.2 Geologic Setting.....	11
2.3 Mount Rosa Complex and Associated Rock Types.....	14
2.4 Analytical Methods.....	17
2.5 Results	20
2.5.1 Petrography	21
2.5.2 Mineral Chemistry	43
2.5.3 Raman Spectroscopy.....	45
2.6 Discussion	55
2.6.1 Zircon Chemistry of the MRC.....	56
2.6.2 Evolution of the MRC.....	68
2.7 Conclusions.....	84
CHAPTER 3: CONCLUSIONS AND OUTLOOK.....	88
3.1 Conclusions.....	88
REFERENCES.....	90
APPENDIX A: EMPA ZIRCON DATA.....	95
APPENDIX B: ADDITIONAL BRIGHT PHASE SCANS	100

LIST OF FIGURES AND TABLES

Figure 1.1	Angular relationships and lengths between cations and anions illustrative of a typical zircon (after Robinson et al. 1971)	2
Figure 2.1	Overview Precambrian map of North America (after Smith et al. 1999)	12
Figure 2.2	Overview map of the Pikes Peak Batholith (after Zito and Hanson, 2014)	13
Figure 2.3	Geologic map of the Mount Rosa Complex	14
Figure 2.4	Hand sample of AS-19	17
Figure 2.5	Bright phase scan of the Pikes Peak granite, thin section PP-MR01	23
Figure 2.6	Pikes Peak Granite zircon viewed optically	23
Figure 2.7	BSE images of zircons found in the Pikes Peak Granite	24
Figure 2.8	CL images of zircons found in the Pikes Peak Granite	24
Figure 2.9	Fayalite-bearing Quartz Syenite zircon viewed optically	25
Figure 2.10	BSE images of zircons found in the Fayalite-bearing Quartz Syenite	25
Figure 2.11	CL images of zircons found in the Fayalite-bearing Quartz Syenite	26
Figure 2.12	Bright phase scan of the Fayalite-bearing Quartz Syenite, thin section PP-MR31	27
Figure 2.13	Granitic Dike zircon viewed optically	28
Figure 2.14	BSE images of zircons found in the Granitic Dike	28
Figure 2.15	CL images of zircons found in the Granitic Dike	28
Figure 2.16	Bright phase scan of thin section PP-MR25	29
Figure 2.17	Mount Rosa Granite sieve zircon viewed optically	30
Figure 2.18	BSE images of sieve zircons found in the Mount Rosa Granite	30
Figure 2.19	CL images of sieve zircons found in the Mount Rosa Granite	31
Figure 2.20	Bright phase scan of thin section PP-2016-07	32
Figure 2.21	Mount Rosa Granite patchy zircon viewed optically	32
Figure 2.22	BSE images of patchy zircons found in the Mount Rosa Granite	33
Figure 2.23	CL images of patchy zircons found in the Mount Rosa Granite	34
Figure 2.24	Bright phase scan of the Mafic Dike, thin section PP-MR58	35
Figure 2.25	BSE images of zircons found in the Mafic Dike	36

Figure 2.26	CL images of zircons found in the Mafic Dike	36
Figure 2.27	Bright phase scan of the type-(I) pegmatites, thin section AS-19	37
Figure 2.28	Type-(I) pegmatite zircon viewed optically	38
Figure 2.29	BSE images of zircons found in the Type-(I) Pegmatite	38
Figure 2.30	CL images of zircons found in the Type-(I) Pegmatite	39
Figure 2.31	BSE images of wallrock zircons found in the Type-(II) Pegmatite	40
Figure 2.32	CL images of wallrock zircons found in the Type-(II) Pegmatite	41
Figure 2.33	Type-(II) Pegmatite fine grained zircon viewed optically	41
Figure 2.34	BSE images of hydrothermal zircons found in the Type-(II) Pegmatite	42
Figure 2.35	CL images of hydrothermal zircons found in the Type-(II) Pegmatite	42
Figure 2.36	Compositional distributions of elemental data in zircons	49
Figure 2.37	EMPA FeO, Y ₂ O ₃ , HfO ₂ , and P ₂ O ₅ element maps for zircons	52
Figure 2.38	Elemental trend plots using EMPA data for zircons	53
Figure 2.39	Raman spectroscopy data for zircons	55
Figure 2.40	Zircon distribution based on type 1A, 1B, 1C, 2, and 3	59
Figure 2.41	Zircon substitution plots	60
Figure 2.42	Type 1A zircon traverse plots	64
Figure 2.43	Type 1C zircon traverse plots	65
Figure 2.44	Type 2 zircon traverse plots	66
Figure 2.45	Type 3 zircon traverse plots	70
Figure 2.46	Metamict zircon traverse plots	73
Figure 2.47	Field images of Mount Rosa Granite heterogeneity	77
Figure 2.48	EMPA biotite data collected from Persson (2017)	78
Figure 2.49	Type-(II) Pegmatite transect	83
Figure 2.50	Simplified diagram illustrating the proposed processes responsible for the formation of the Mount Rosa Complex	88
Table 1.1	Summary table of the different classes and subclasses of pegmatites with the corresponding geochemical signatures and minerals	7

Table 2.1	Detection Limits and standard deviation for all elements analyzed using EMPA	20
Table 2.2	Summary of all samples and analytical techniques used in this study	22
Table 2.3	Representative EMPA compositions of zircons from individual rock units within the Mount Rosa Complex	45
Table 2.4	Representative EMPA compositions of metamict zircon zones	51
Table 2.5	Summary table of individual zircon groups	57

ACKNOWLEDGEMENTS

I would like to express a great appreciation to my advisor Dr. Katharina Pfaff. Your advice and support over the past two years taught me to think like a researcher and produce a thesis I am proud of. You deserve more thanks than I can possibly offer. To my committee member Dr. Ric Wendlandt, thank you so much for many fantastic conversations. I am so grateful to have learned from you, and will miss receiving the incredible amount of information you provided each time I posed a question. Finally, special thanks is extended to my third committee member, Dr. Alex Gysi. I am so fortunate to have a committee member who worked passionately on a location similar to my research. To be able to talk about textural and chemical similarities was incredibly valuable, and your willingness to share your observations will always be appreciated. While words alone will never be able to express my gratitude for my fantastic committee, I again must say, thank you all so much!

Beyond my committee, I want to extend additional thanks to several other individuals. First, to Heather Lowers at the USGS, who assisted me in the collection of all my SEM-CL images. Then, to Julian Allaz at ETH Zurich (formally at the University of Colorado, Boulder), who willingly standardized the EMPA to 21 elements and assisted in my data collection. And finally, two individuals that are currently at the University of Colorado, Boulder, Markus Raschke, who assisted me with Raman spectroscopy and aided in the understanding and interpretation of my data and to Nigel Kelley, who offered insight to zircon textures and chemistry numerous times. This project would not have been possible without any of you.

As a final expression of gratitude, I would like to extend a warm thank you to my parents Cheryl Saha and Richard Smith. You both encouraged me to explore my interest in geology at a young age, and humored my desire to bring rocks home from various vacations and rock shops. I would never be where I am today without your constant support, both financially and emotionally, and I hope you both know how much I love and appreciate you. And finally, a huge thank you to three amazing friends Aric Snellstrom, Spencer Aertker and Asha Mahtama. You are all so incredible and I cannot imagine these past two years without you by my side.

CHAPTER 1: INTRODUCTION

The 1.04 Ga Mount Rosa Complex (MRC) hosts a diverse suite of peraluminous to peralkaline rock units with an abundance of rare earth element (REE) bearing minerals (i.e. bastnasite, allanite, xenotime, monazite), other high field strength elements (HFSE; i.e. Zr, Ti, Nb, Ta), and NYF-type pegmatites. Zircon, an accessory mineral found in all rock units in the MRC, is able to capture changes in melt chemistry throughout the evolution of the complex. In this study, zircons from all rock units were chosen in order to observe their textural and chemical characteristics. Through polarized light microscopy, automated mineralogy, FE-SEM (BSE and EDS), SEM-CL, EMPA, and Raman analyses, the complex's evolution from peraluminous to peralkaline, and the transition to hydrothermal could be captured. Additionally, this study provides insight into the origin and remobilization processes of REEs and HFSEs.

1.1 Overview of Zircon

Zircon is a common accessory mineral in all rock types, and a powerful tool to elucidate the complex evolution of magmatic systems (Gagnevin et al. 2010). Zircon is known to be highly stable as it has been observed in a wide variety of geologic settings as well as being recognized as the oldest material on Earth (Ayers et al. 2012). Generally, events responsible for initial zircon formation are preserved, while additional segments of later growth periods continue to form around the original grain. The combination of mineral chemistry and textural variations provides information to decipher various pieces of information such as age and chemical evolution.

In nature, zirconium is present as +4 valence state with a small ionic radius of $r = 0.84 \text{ \AA}$ (Ayers et al. 2012). Zirconium is classified as a high field strength element (HFSE) due to its high ionic potential. Both Zr and Si in the zircon structure are tetravalent (Hoskin and Schaltegger, 2003). Zircon, ZrSiO_4 , is a tetragonal mineral, typically with a length to width ratio of 1:5 (Corfu et al. 2003). Zircons grow as a chain of alternating SiO_4 tetrahedra joined with ZrO_8 triangular dioctahedra extending parallel to the c-axis (Robinson et al. 1971). These chains are joined by edge-sharing dioctahedra. Structurally, zircon is defined by two cation sites, a 4-coordinated Si-site with the distorted 8-coordinated Zr-site (Hoskin and Schaltegger, 2003). Stoichiometrically, zircon (ZrSiO_4) is composed of 67.2 wt% ZrO_2 and 32.8 wt% SiO_2 . Zircons are characterized by their (100) cleavage, prismatic habit, and high birefringence. Zircon is naturally sp^2 hybridized since the average bond angle at oxygen is 120° (Robinson et al. 1971). The oxygen sits in a planar array with one Si at 1.622 \AA , one Zr at 2.131 \AA , and a final Zr at 2.628 \AA (Fig. 1.1).

Zircon is most commonly found in Si-saturated igneous rocks (Hoskin and Schaltegger, 2003). Crystal morphology and zircon textures alone can be useful to decipher a rock's history, but can also be combined with its chemistry to fingerprint an evolving magma. Magmas oftentimes reach saturation in zircon early, resulting in the nicely developed crystal faces typically associated with zircon. In cases where zircons crystallized in highly fractionated magmas, only partially developed faces are observed (Corfu et al. 2003). Oftentimes, small, needle-shaped crystals form due to local Zr saturation, however early Zr-saturated melts generate large, euhedral crystals commonly depicting the 1:5 length-to-width ratio (Hoskin and Schaltegger, 2003).

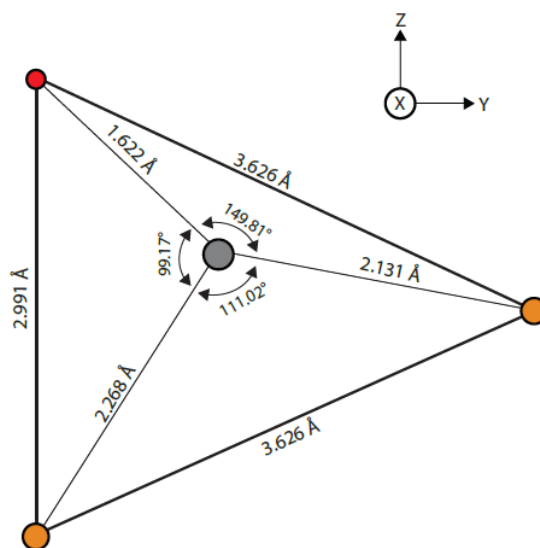


Figure 1.1: Angular relationships and lengths between cations and anions illustrative of a typical zircon. Zirconium is red, silica is orange, and oxygen is gray. Modified from Robinson et al. 1971.

Zoning is a common feature observed in zircon crystals, which can best be observed in backscatter electron images (BSE) and cathodoluminescence (CL) images. Zoning is known to be a result of compositional variations within the zircon structure and importantly highlights varying amounts of elements usually not typical of the zircon structure (U, Th, Hf, REE, etc; Corfu et al. 2003). Concentric zoning is the most commonly observed, in which younger layers of zircon grow upon older layers and the changing chemistry depicts various zoned layers. Sector zoning is described as sections of the same zircon crystal with varying densities and compositions. Many models have been proposed for the formation of this more rare form of zircon zonation such as unequal growth rates or slow diffusion rates, but a general

consensus has yet to be determined (Corfu et al. 2003). Xenocrystic cores are commonly observed in igneous zircons with subsequent zircon growths forming concentric layers around the original core. If older cores or zones are enriched in radioactive elements such as U, fracturing of younger, subsequent layers that are more rigid will be observed (Corfu et al. 2003).

Metamictization of zones with higher concentrations of radioactive elements occurs as a secondary process to the crystal as the crystal structure is damaged due to radiation (Nasdala et al. 2001). Decay of radioactive elements incorporated into the crystallographic structure, oftentimes U and Th, creates the release of daughter isotopes, which is a low energy process but is paired with a heavy α -recoil (Geisler et al. 2007). Additionally, light α -particles of high energy are released, resulting in displacements within the structure. Structural defects in zircon crystals allows for the incorporation of water (>15 wt. %) rather than the usual <0.01 wt. % in natural zircon (DeHoog et al. 2014). Furthermore, areas of structural defects are prone to alteration and enhanced dissolution, resulting in chemical transport (Geisler et al. 2007).

Prior to the 1980s, zirconium was believed to be immobile due to a high charge-to-ionic-radius ratio, causing the mineral to be incompatible during magmatic fractionation (Pearce and Cann, 1973; Finlowbates and Stumpfl, 1981; Yang et al. 2014). More recently, experimental and field evidence has revised this assumption. REE, HFSE and Y have a strong bond with hydrous magmas rich in ligands such as F, Si, and alkalis (Aja et al. 1995; Veskler et al. 2005; Yang et al. 2014). High concentrations of HFSE are associated with F-rich rocks in areas such as Strange Lake, Canada, the Baerzhe alkaline granite pluton, Asia, Thor Lake, Canada, and the Sierra Blanca Peaks, Texas, which further supports this hypothesis and provides a transport mechanism (Rubin et al. 1989; 1993; Sheard et al, 2012; Gysi and Jones, 2013; Yang et al, 2014). Hydrothermal zircons can display oscillatory zoning, sector zoning, or no zoning at all, while chemically, these zircons can contain elevated concentrations of trace elements (Schaltegger, 2007).

1.2 Overview of Pegmatites

By definition, a pegmatite is “an igneous rock, commonly of granitic composition, that is distinguished from other igneous rocks by its extremely coarse but variable grain size, or by an abundance of crystals with skeletal, graphic, or other strongly directional growth habits” (London, 2008). Pegmatites can cluster along batholith boundaries and display coarse grained, elongated crystals growing radially from the wall to the core (Thomas et al, 2012).

Interest in pegmatites began back in the 19th century, and many models have been suggested regarding their formation and economic enrichments. Generally, most models fit a certain category of pegmatite however; a consensus has yet to be reached that is applicable to all pegmatites. Today, many models are proposed using a combination of experimental and field evidence (Jahns and Burnham, 1969; London, 2008, Thomas et al, 2012). Fluid inclusion data suggests pegmatites are characterized by a high concentration of H₂O (20-50 % g/g) during formation as well as elevated in fluxing elements (Thomas et al, 2012). In order to reduce viscosity and stimulate large crystal growth, fluxing elements such as B, P, F, CO₂, Cl, etc. must be present to increase elemental diffusion, increase crystal growth rates, and suppress nuclei for crystallization (London, 2009). London (2008) suggests pegmatitic textures form first via the crystallization of the anhydrous minerals along the border, wall, and coarse feldspar zones of a pegmatite, and then the accumulation of fluxed elements occurs through constitutional zone refining. This constitutional zone refining is also an important aspect to the skeletal nature of minerals. Pegmatites are generally characterized by large quartz cores, which suggests high SiO₂ concentrations, leaving some to believe a silica gel must be present in the final stages of crystallization since a hydrothermal solution would dilute the SiO₂ concentration (Thomas and Davidson, 2008; Thomas et al, 2012). Additionally, a silica gel would support the high enrichment of trace elements in certain pegmatites since it is an effective ion-exchange material (Thomas et al, 2012).

Pegmatites are believed to crystallize at low to intermediate pressures and temperatures up to granulite conditions (Černý and Ercit, 2005). The fluids responsible for pegmatite formation are believed to behave water-like at high temperatures, but the rheology of the fluids can change dramatically during cooling over a small temperature interval (Thomas et al, 2012). Authors suggest the fluid responsible for pegmatite crystallization is of high viscosity, which allows for the growth of large, unbroken crystals attached to pegmatite walls (London, 2008; Thomas et al, 2012). Temperatures as low as 262°C have been suggested for pegmatite crystallization (Thomas, 1994).

Overall, the consensus for pegmatite formation is that a melt separates from a larger granitic parent system (Thomas et al, 2012). In order for the melt to become isolated, it must migrate between grain boundaries or channels. Upon isolation, the melt must be low in viscosity and have a favorable wetting property; elevated in H₂O especially in lower temperatures (18.1 % g/g at 550°C; McKenzie, 1985). Following separation, researchers debate the timeframe a pegmatite takes to fully crystallize. The crystallization timescale was largely believed to be very slow for large crystal growth (Webber et al., 1998), however Morgan and London (1999) suggest rapid crystallization of less than a month.

Granitic pegmatites typically display enrichment in Li, Be, Rb, Cs, Nb, Ta, Sn, REE, B, P, and F up to weight percent levels, which is attributed to the unusual non-granitic mineral assemblages. Researchers agree pegmatite mineralogy and geochemistry (pegmatite type) is related to the tectonic setting and granitic host rock (Martin and De Vito, 2005). The following five classes of granitic pegmatites (with subdivisions within each class) are recognized based on mineralogy, pressure/temperature conditions of formation, and host-rocks (Table 1.1; Černý and Ercit, 2005, London, 2008):

1. The abyssal class is reserved for pegmatites forming at temperatures between upper amphibolite to granulite conditions (700–800°C), but relatively low pressures (5-6 kbar), so pegmatite formation must occur at intermediate depths. These pegmatites typically display complex textures including graphic granite, and can display migmatitic leucosome layers. Four subclasses (HREE, LREE, U, and BBe) make up the abyssal class, each name corresponding to the subclass unique geochemical signature (Table 1.1).
2. The muscovite class pegmatites are defined by high pressure (6-8 kbar) conditions of formation and are sourced from partial melting. These pegmatites do not display any economic importance since their mineralogy is composed of feldspar, quartz, and mica. These pegmatites are conformable to the granitic host rock.
3. The muscovite-rare element class pegmatites are described as a hybrid between the muscovite class and the rare earth element class. This class includes two sub-classes, distinguished based on mineralogy and mineral assemblages. These pegmatites develop between 500 and 700°C and 4-6 kbars of pressure that form as intrusive bodies uncomfortable to the host rock. The mineral assemblage contains economic grade muscovite and sub-economic concentrations of REEs.
4. The rare element class pegmatites are generated from granitic plutons between intermediate to shallow depths and show economic concentrations off REEs. Two different sub-classes (REL-REE and REL-Li) are observed, which are subdivided based on their emplacement settings and elemental signatures, making this the most diverse class of the five (Table 1.1). The rare element pegmatites generally form at lower temperatures (500-650°C) and pressures (2-4 kbar).
5. The miarolitic class pegmatites are distinguished by the presence of cavities, created by the trapping of gas bubbles during exsolution from a parent pegmatite body. Two sub-classes (MI-REE and MI-Li) are recognized for these type of pegmatites, based on geochemical signatures. These pegmatites form at the lowest pressures (1.5-2 kbar) and temperatures (400-650°C) of all five classes, allowing for the formation of the miaroles. These pegmatites are recognized as the best for rare minerals and gem quality specimens.

In addition to the five classes pegmatites can fall into, two pegmatite families are also recognized: Niobium-Yttrium-Fluorine (NYF) and Lithium-Cesium-Tantalum (LCT; Černý and Ercit, 2005, London, 2008). These families correspond to the primary chemical enrichments due to fractionation.

1. NYF-type pegmatites display enrichment in heavy rare earth elements (HREE), Be, Ti, Sc, and Zr in addition to Nb, Y, and F, and are believed to be sourced from melting of the crust in rift zones with mantle contamination. These pegmatites display alkaline compositions and are depleted in P and light REE and are typically associated with A-type-(anorogenic) granites. The fluorine enrichment is accredited to be sourced from amphibole and mica melting reactions at the base of the continental crust.
2. LCT-type pegmatites can be enriched in Be, B, F, P, Mn, Ga, Rb, Nb, Sn, and Hf in addition to Li, Cs, and Ta. These pegmatites are peraluminous with elevated Li concentrations in aluminosilicates. These pegmatites are typically related to I-type-(igneous protolith) and S-type-(sedimentary protolith) granites. Li is sourced from melting reaction of micas and Li remains as a restite in the source. Additionally, these pegmatites are characterized by a high quantity of phosphate minerals due to high P concentrations.

1.3 Overview of Mount Rosa Pegmatites

The Mount Rosa Complex is located at the southernmost end of the Pikes Peak Batholith, southwest of Colorado Springs, Colorado. The complex is host to six rock units (Pikes Peak Granite, Fayalite-bearing Quartz Syenite, Granitic Dikes, Mount Rosa Granite, Mafic Dikes, and Pegmatites), which transition from peraluminous to peralkaline. Additionally, all rock units display elevated concentrations of REE-bearing minerals and high field strength elements. An extensive study of the Mount Rosa area conducted by Gross (1962) included detailed mapping and descriptions of the mineralogy and petrology of various rock types. Focus was placed on the relationship between the high concentration of pegmatites, especially in the area of St. Peter's Dome and their granitic host rocks (Gross, 1962; Gross and Heinrich, 1965; Gross and Heinrich, 1966). The pegmatites within the Mount Rosa area are diverse, ranging from small, unzoned pegmatites to wide, occasionally zoned pegmatites (Gross and Heinrich, 1966). The pegmatites of the Mount Rosa Complex are classified as miarolitic, some falling in to the more specific miarolitic-rare earth element (MI-REE) subclass (Černý and Ercit, 2005). Additionally, the pegmatites in the MRC are classified as NYF type due to their elevated concentration of Ti, Y, Sc, REE, Zr, U, Th, F and Nb > Ta (Martin and De Vito, 2005; Černý and Ercit, 2005).

Table 1.1: Summary table of the different classes and subclasses of pegmatites with the corresponding geochemical signatures and minerals

Class	Subclass	Geochemical Signature	Typical Minerals
Abyssal	AB-HREE	HREE, Y, Nb, Zr, U, Ti	Y-Nb-oxide, uraninite, zircon, allanite
	AB-LREE	LREE, U, Th, Ti	Allanite, monazite, uraninite, thorite
	AB-U	U, Th, Zr, LREE	Uraninite, thorite, zircon, allanite
	AB-BBe	B, Be	Dumortierite, grandidierite, kornepurine, werdingite, chrysoberyl, sapphirine
Muscovite		Ca, Ba, Sr, Fe>Mn	Muscovite, biotite, almandine-spessartine, kyanite, sillimanite
Muscovite-Rare Element	MSREL-REE	Be, Y, REE, Ti, U, Th, Nb, Ta	Muscovite, fergusonite, samarskite, monazite, beryl, almandine-spessartine
	MSREL-Li	Li, Be, Nb	Beryl, cassiterite, columbite, lepidolite
Rare-Element	REL-REE (Allanite-monazite, euxenite, gadolinite)	Be, Y, REE, U, Th, Nb>Ta, F	Allanite, monazite, zircon, rutile, fluorite, ilmenite, euxenite, xenotime, gadolinite, fergusonite, samarskite
	REL-Li (Beryl, complex, albite-spodumene, albite)	Li, Rb, Cs, Be, Ga, Sn, Hf, Nb, Ta, B, P, F	Beryl, columbite, tantalite, rutile, triplite, triphylite, spodumene, petalite, lepidolite, topaz, microlite, tourmaline, amblygonite, spodumene
Miarolitic	MI-REE	Y, REE, Ti, U, Th, Zr, Nb, F	Topaz, amazonite, zinnwaldite, fluorite, beryl, zircon, xenotime, monazite
	MI-Li	Li, Be, B, F, Ta>Nb	Tourmaline, beryl, topaz, lepidolite, spodumene, petalite, spessartine, microlite

Subclass colors: Black - Neutral pegmatites, Red - NYF-type pegmatites, Blue - LCT-type pegmatites
Rare-Element subclass bold font corresponds to the subclass with the subtypes in parentheses
Summary table from Černý and Ercit, (2005) and London, (2008).

Historically, pegmatites of the Mount Rosa area have been divided into two categories: Pikes Peak-type pegmatites and Mount Rosa-type pegmatites (Gross and Heinrich, 1966). The pegmatites in the Mount Rosa Complex have a N-NW strike, are around 2 meters in width, and are composed of alkali granite. Two pegmatite types are found within the complex. The first of the two pegmatite types were originally referred to as “exterior” pegmatites (Gross and Heinrich, 1966) are found in the Pikes Peak Granite, have irregular contacts with the wall rock, lack miarolitic cavities, are poorly zoned, and are

mineralogically “simple” (Gross, 1962; Gross and Heinrich, 1966; Zito and Hanson, 2014). Gross and Heinrich (1966) interpreted these exterior pegmatites to have been sourced from residual melt from the overall Mount Rosa Complex. The second type, which Gross and Heinrich (1966) referred to as “interior” pegmatites, are coarser grained, have sharp contacts with the host rock, are poorly zoned, and are mineralogically more “complex” (Gross and Heinrich, 1966). A recent study conducted by Persson (2017) revisited the pegmatite classification in the Mount Rosa Complex:

Type-(I) pegmatites are mineralogically “simple”, composed of classic granitic minerals like quartz, alkali feldspar and albite with minor amounts of biotite, Fe-Ti oxides, zircon, and Na-amphibole (Persson, 2017). These pegmatites are narrow (generally < 1 ft wide), are moderately to poorly zoned, and have irregular to well-defined contacts with the host rock. Mirolitic cavities filled with quartz and microcline can be characteristic of these pegmatites, but are not always observed (Gross 1962). Oftentimes, type-(I) pegmatites display a pinch-and-swell geometry (Persson, 2017).

Type-(II) pegmatites are described as mineralogically more complex, fine grained, with moderate to good zonation (Persson, 2017). They include the same mineral assemblage observed in type-(I) pegmatites with the addition of REE-bearing minerals such as columbite, monazite, astrophyllite, and cryolite and large amounts of fluorite (Persson, 2017). Where present, cryolite is generally concentrated near the core of these pegmatites and produces a vuggy texture where it weathers out. These pegmatites also host magmatic (rim) and hydrothermal (core) zircons. Oftentimes, the type-(II) pegmatites display a brecciated texture, and can range from narrow to up to 6 feet in width (Persson, 2017).

1.4 Overview of Rare Earth and High Field Strength Elements

Internationally, the demand for rare earth elements (REE) as well as other high field strength elements (HFSE) has increased exponentially and concern regarding supply and expense continues to rise (USGS, 2014). Rare Earth Elements and other HFSEs are necessary components when building most devices advanced in technology such as smart phones, solar panels, and batteries.

REEs are defined as 17 metallic elements, including atomic numbers 57 (lanthanum) through 71 (lutetium), plus yttrium and scandium with further subdivisions into light REEs and heavy REEs (Geological Society of London, 2011). Yttrium is oftentimes classified as a REE due to its similarity in chemical and physical properties to the heavy REEs, as well as its common co-occurrence with other heavy REEs. Scandium also displays similar physical and chemical properties, however it generally does not occur with

the other REEs in nature. REEs can be further subdivided into 1) light REE (La-Gd) and 2) heavy REE (Tb-Lu). Yttrium is considered a heavy REE due to similar physical and chemical properties.

HFSE are defined as tetravalent (3+) and pentavalent (5+) transition metals characterized by their relatively small ionic radius and intermediate electronegativity values (Finlowbates and Stumpfl, 1981). Importantly, the HFSE class includes all REE with the addition of Zr, Nb, Hf, Th, U, and Ta. These elements have a high charge-to-ionic-radius ratio, making bonding to most elements difficult. However recent research has determined HFSE to have a strong bond in hydrous magmas, rich in ligands (Veskler et al., 2005). The main mechanism for REE and HFSE enrichment is thought to be due to their incompatibility in magmatic melts, causing them to remain in the melt as rock forming minerals crystallize (Gysi and Williams-Jones, 2013; USGS, 2014). Concentrations in the remaining melt will continue to increase, forcing REE/HFSE-bearing minerals to crystallize and/or to be potentially transported along fractures or permeable rocks if hydrothermal fluid is present (Gysi and Williams-Jones, 2013). Today, few deposits are considered economic, but many areas have elevated concentrations of these elements and could be of value in the future.

Despite the naming convention, REEs are actually more abundant than silver, gold, or platinum with the exception of promethium due to its radioactivity and short half-life (Geological Society of London, 2011, USGS, 2014). Cerium is the most abundant in the crust at 43 ppm; much higher than other elements such as copper at 27 ppm, while thulium is the least abundant at 0.28 ppm. All REEs possess a tetravalent charge (3+) with similar ionic radii, however cerium can be quadravalent (4+) while europium can be divalent (2+). Additionally, five REEs are radioactive: ^{138}La , ^{144}Nd , ^{147}Sm , ^{152}Gd , and ^{176}Lu . Economic REE deposits are most common in carbonatites followed by alkaline igneous rocks.

CHAPTER 2: TRACING THE MAGMATIC TO HYDROTHERMAL EVOLUTION OF THE MOUNT ROSA COMPLEX, COLORADO: TEXTURAL AND CHEMICAL EVIDENCE USING ZIRCON

2.1 Introduction

Due to its stability in a variety of geologic environments, zircon is a common accessory mineral in most rock types. Zircon's sensitivity to changing pressure, temperature, and magmatic chemistry make it a valuable accessory mineral when attempting to unravel the evolution of a given magmatic system (Gagnevin et al., 2010; Zhang and Xu, 2016). Texturally, zoning is an important feature in many zircons, which develops as the chemistry of the magma evolves and the zircon uptakes varying amounts of elements (i.e. REE, HFSE, and U; Hoskin and Schaltegger, 2003). The presence of these elements can be used to fingerprint the coexisting melt as well as provide valuable geochronology data through the use of U-Pb dating (Hoskin and Schaltegger, 2003). Backscatter electron imaging and SEM-CL imaging allows for distinct zones to be easily identified, allowing the preserved textures to be better understood when paired with chemical data. Chemical variations highlight magmatic fluctuations from the initial state of growth (core) to the final stages of zircon crystallization (rim). These various geologic events can be either zircon forming or resorbing. Additionally, REE trace elements can provide information about magmatic oxidation states while Ti contents can be used as a thermometer (DeHoog et al., 2014). When paired together, chemical and textural data provide a better understanding of the magmatic history.

Discrepancies in zircon textures has inspired many studies to better understand the origins of specific zircon textures (Corfu et al., 2003). Zircon remains stable during magmatic, metamorphic and erosional processes over time, and have the ability to record these events, albeit careful attention must be placed in order to eliminate bias. Gagnevin et al. (2010) successfully used zircon in a variety of different rock types from the Monte Capanne pluton, Italy. Their conclusions suggest magma mixing between peraluminous and metaluminous melts within the plutonic body, which created diffusion-limited dissolution-recrystallization textures. The authors conclude that all rock units in the Monte Capanna complex are co-genetic regardless of the complex rock variability. Other studies use zircon to decipher the evolution of a magmatic to hydrothermal fluid, responsible for enriching HFSE and REE at Thor Lake, Canada and Strange Lake, Canada, which are both peralkaline complexes with elevated REE and HFSE (Sheard et al., 2012; Hoshino et al., 2012; Gysi et al., 2016).

The 1.04 Ga Mount Rosa Complex (MRC) is located at the southernmost end of the much larger 1.08 Ga A-type Pikes Peak Batholith, southwest of Colorado Springs, Colorado. The MRC transitions from

a peraluminous to peralkaline melt and respective rock units (Smith et al., 1999). Collectors have reported many unusual F-bearing minerals such as cryolite (Na_3AlF_6) and astrophyllite ($(\text{K}_2\text{NaFe}^{2+}_7\text{Ti}_2\text{Si}_8\text{O}_{28}(\text{OH})_4\text{F})$) as well as hydrothermal zircon in the later peralkaline units and the NYF-type pegmatites in the area (Zito and Hanson, 2014). Zircon occurs in all six rock units in the MRC. This study focuses on the use of chemical and textural variations in zircon to better understand the transition from a peraluminous to a peralkaline melt, and subsequent hydrothermal processes of the MRC. Additionally, new data paired with previous geologic studies in the area (Gross and Heinrich, 1965; Gross and Heinrich, 1966; Smith et al., 1999; Persson, 2017) and similar complexes (i.e. Strange Lake, Canada) provides a better understanding of the evolution from peraluminous to peralkaline and the formation of NYF-type pegmatites in the MRC.

2.2 Geologic Setting

The Pikes Peak Batholith (PPB) is located in central Colorado, USA, and is classified as an anorogenic (A-type) granitic body emplaced between 1.08 and 1.04 Ga (Smith et al. 1999). Smith et al. (1999) state that all rock units of the MRC have high $\text{Fe}/(\text{Fe}+\text{Mg})$ ratios, high $\text{K}_2\text{O}/\text{Na}_2\text{O}$ ratios, elevated K_2O , and elevated incompatible trace element concentrations (Zr, Nb, Y, Hf, Ta, Ga, and REE), which are consistent with A-type granite characteristics. Prior to emplacement, the Yavapai Orogeny (1.79 Ga) took place in which volcanic-plutonic sediments and greywacke-pelite facies were deposited and consolidated creating a >1,000 km-wide belt stretching across the southern margin of the Archean Wyoming craton (Fig. 2.1; Reed et al., 1978; Karlstrom and Bowring, 1987; Smith et al., 1999). Transtensional-transpressional events occurring at 1.4 Ga weakened the crust and generated mantle-derived magmas, which became emplaced within this belt, an event known as the Berthoud Orogeny (Sims and Stein, 2003). Plutonic bodies preceding the emplacement of the PPB (Longs Peak St. Vrain batholith dated at 1.4 Ga; Rb-Sr dating) and following the PPB emplacement (Enchanted Rock batholith dated at 1.03 Ga; U-Pb dating) have been recognized as A-type granites of similar age (Fig. 2.1; Anderson, 1983; Frost and Frost, 1997). Northeast trending mafic dikes located in the southwestern United States have been dated at 1.1 Ga and have led researchers to believe their presence is related to magmatic intrusions similar to that of the PPB (Fig. 2.1; Smith et al., 1999). These dikes suggest a failed emerging rift due to a midcontinent high causing lithospheric thinning, therefore allowing the emplacement of magmatic bodies (i.e. the Longs Peak St. Vrain batholith, the Pikes Peak batholith, and the Enchanted Rock batholith) in the weakened crust (Anderson, 1983; Hoffman, 1988; Smith et al., 1999). Today, the PPB has roughly 3,300 km^2 exposure at the surface due to the Laramide Orogeny, which caused uplift and glaciation <70 Ma, leading to the erosion of the overlying sediment from the Yavapai Orogeny (Smith et al., 1999).

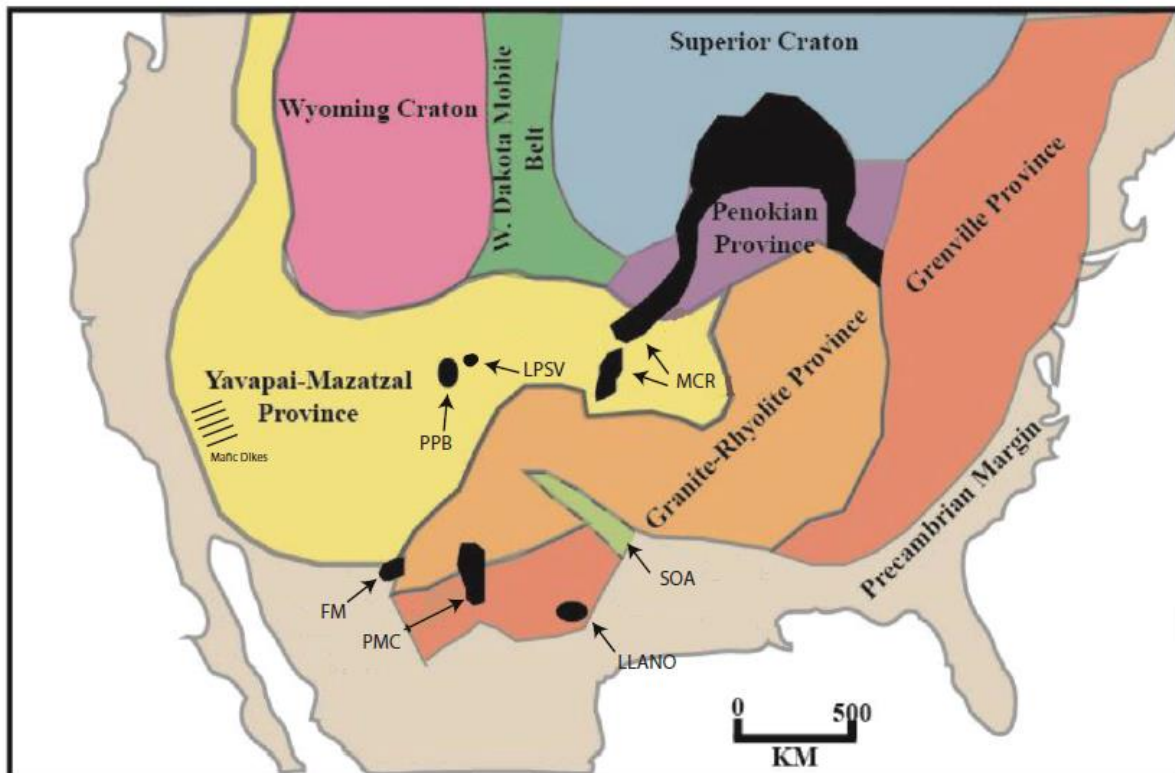


Figure 2.1: Overview map of Precambrian provinces within North America (Smith et al., 1999). Black areas represent the granites that intruded around 1.1 Ga. Labels are as follows: Mid-Continent Rift (MCR), Llano Uplift (LLANO; host to the Enchanted Rock batholith), Pecos Mountain Complex (PMC), Franklin Mountains (FM), Longs Peak St. Vrain Batholith (LPSV), and Pikes Peak Batholith (PPB). The Southern Oklahoma Aulacogen is labeled SOA.

The PPB is characterized by coarse grained biotite \pm amphibole syenogranite and monzogranite with minor amounts of gabbro, diabase, syenite and fayalite and is host to numerous but small late-stage plutons (<10% of exposure area) which can be divided into sodic and potassic intrusions (Fig. 2.2; Barker et al., 1975). Sodic intrusions are represented by Na-Fe amphibole granite while the potassic intrusions are characterized by biotite granite/quartz monzonite (Smith et al., 1999). Flow structures suggest three main intrusive centers known as the Buffalo Park (potassic), Lost Park (potassic), and Pikes Peak (sodic) intrusive center (Fig. 2.2; Hutchinson, 1976). Additionally, the Lake George ring complex is recognized for its variation between potassic and sodic series in a “ring like” structure.

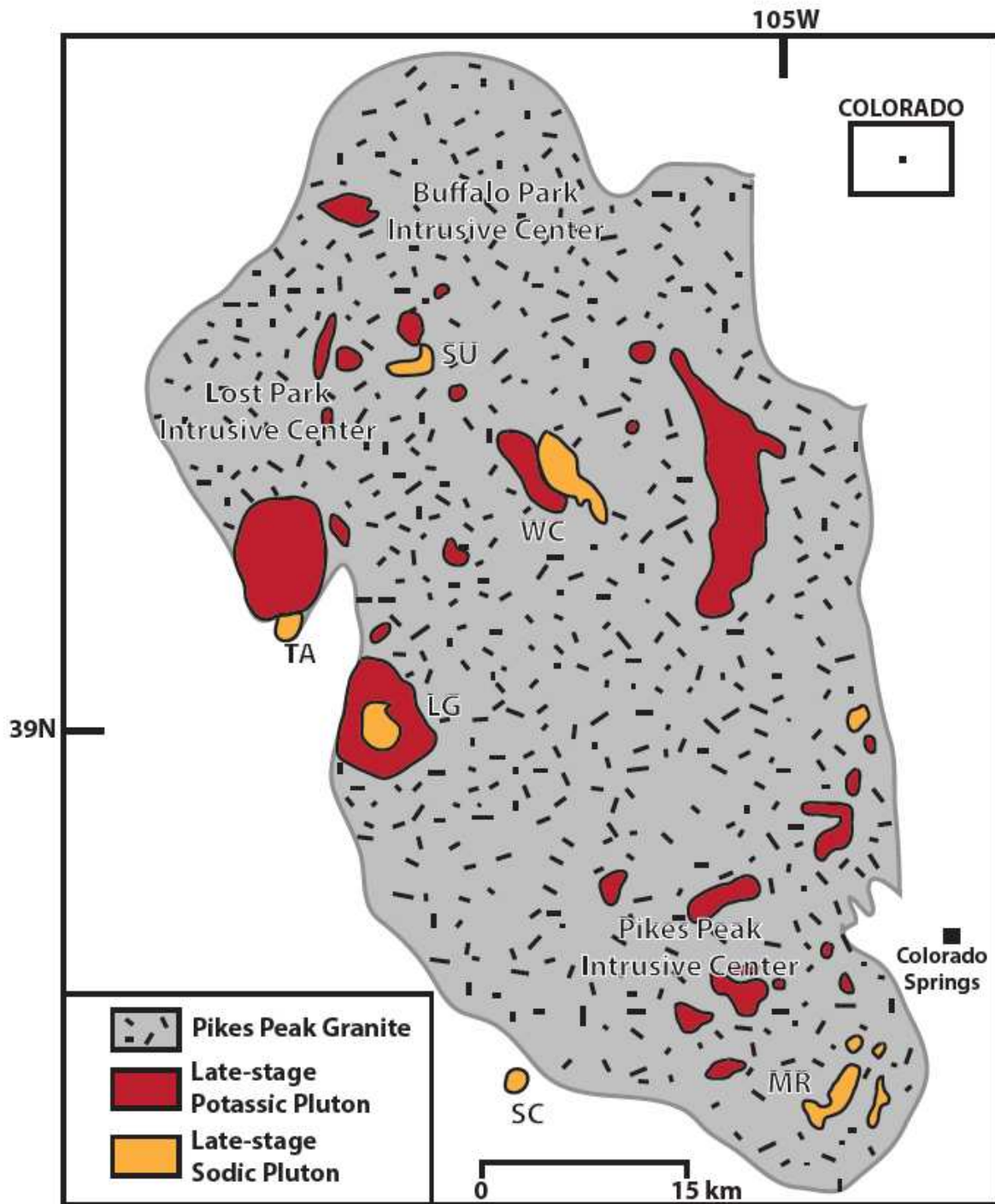


Figure 2.2: Overview map of the Pikes Peak Batholith and the associated potassic and sodic plutons. The Mount Rosa Complex (MR) is located at the southern end of the batholith and is the location of this study. TA-Tarryall, LG-Lake George Ring Complex, SC-Spring Creek, SU-Sugarloaf, and WC-West Creek (Zito and Hanson, 2014).

2.3 Mount Rosa Complex and Associated Rock Types

The 1.08 Ga Mount Rosa Complex (MRC) is located 15 km southwest of Colorado Springs, Colorado, at the southernmost end of the PPB (Fig. 2.2). The MRC comprises the youngest rocks of the PPB and is composed of rocks ranging from peraluminous to peralkaline (Smith et al., 1999). Rock types within the MRC are as follows (from oldest to youngest): peraluminous Pikes Peak biotite granite, fayalite-bearing quartz syenite, granitic dikes, peralkaline Mount Rosa Na-amphibole granite, mafic dikes, and pegmatites (Fig. 2.3; Gross and Heinrich, 1965; Keller et al., 2005; Persson, 2017). The MRC and all associated rock types are enriched in REE and HFSE such as Th, Nb, and Zr relative to primitive mantle rocks. The Mount Rosa Granite was dated at 1.04 Ga by Gross and Heinrich (1965) using U-Pb in zircon, making it the youngest dated unit within the PPB.

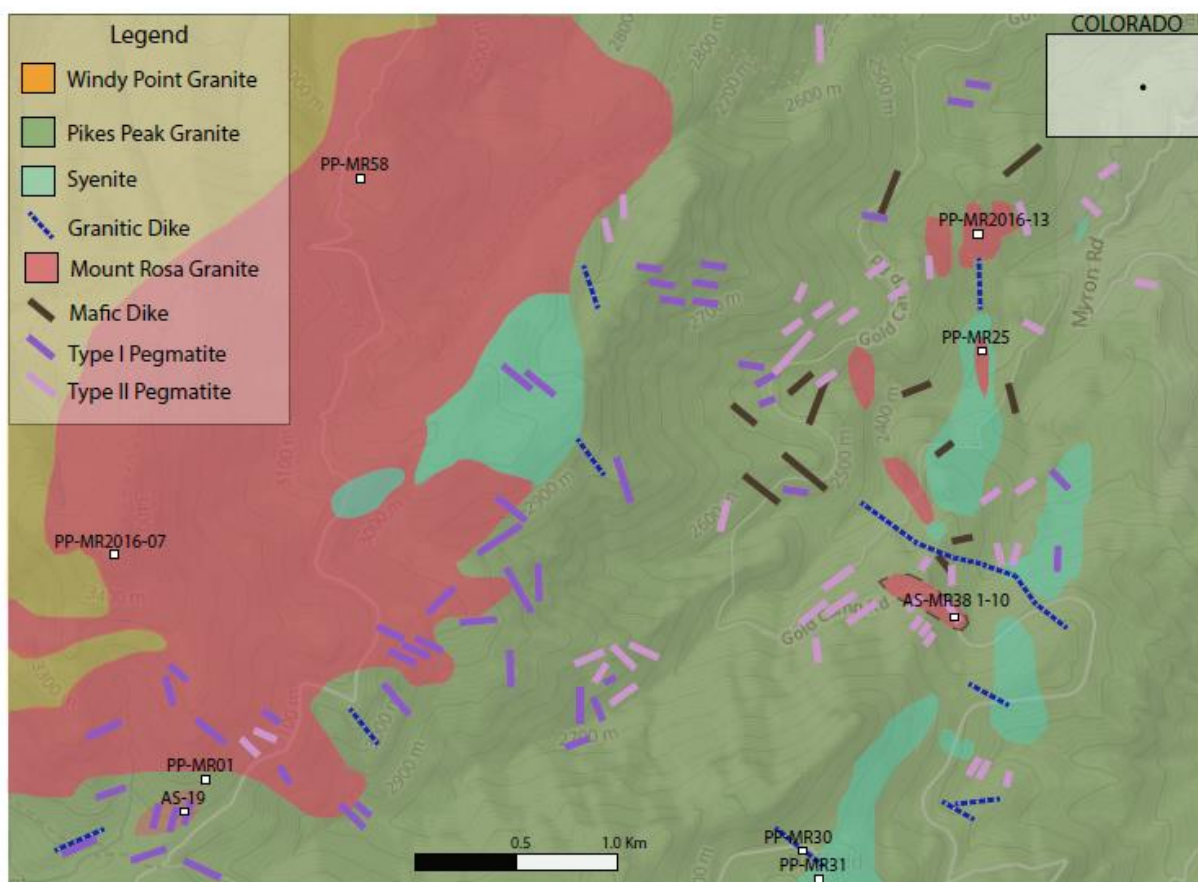


Figure 2.3: Geologic Map and sample locations within the Mount Rosa Complex, Pikes Peak Batholith, Colorado. Dashed boundaries indicate the extent of the rock unit is unknown. Mapping conducted by Gross (1962), Keller et al. (2005), and Persson (2017).

Pikes Peak Granite

The peraluminous Pikes Peak biotite granite ranges between medium to coarse grained and is generally pink (Gross and Heinrich, 1965). Gross and Heinrich (1965) describe the Pikes Peak granite to be composed of quartz, microcline, albite and biotite with minor amounts of hornblende, fluorite, and zircon. This granite can be divided into the volumetrically abundant hypersolvus granite and the less abundant subsolvus granite (Keller et al., 2005). The Pikes Peak granite is the oldest rock type in the MRC (Hoffman, 1988; Smith et al., 1999).

Fayalite-bearing quartz syenite

The fayalite-bearing quartz syenite typically has irregular, gradational contacts with the Pikes Peak granite (Gross and Heinrich, 1965; Barker et al., 1975; Persson, 2017). Typically, this unit is more resistant to weathering than surrounding units, and oftentimes forms oval-shaped bodies situated in alluvium. The syenite is gray to green when fresh but weathers to a brown and is sometimes bleached (Barker et al., 1975, Persson, 2017). Barker et al. (1975) describes the syenite as coarse grained, homogeneous, and primarily composed of quartz, plagioclase and alkali feldspar with fayalite, fluorite, zircon and Fe-Ti oxides as accessory minerals.

Granitic Dikes

The granitic dikes range from medium-grained to aplitic (Gross, 1962; Persson, 2017). The granitic dikes occur throughout the Mount Rosa Complex, and display a radial geometry, extending from the center of the Mount Rosa intrusive center (Persson, 2017). The unit is composed of both monzogranite and syenogranite (Gross and Heinrich, 1965). Granitic dikes are composed of albite, alkali feldspar, quartz, and biotite with accessory minerals of Fe-Ti oxides, arfvedsonite, and zircon.

Mount Rosa Granite

The peralkaline Mount Rosa Na-amphibole granite is pale orange where fresh, but weathers to a dull brown (Gross and Heinrich, 1965, Barker et al., 1975). Outcrops of the MRG display irregular contacts with the Pikes Peak biotite granite and researchers describe the unit as occurring in sheet and sill-like bodies (Gross and Heinrich, 1965; Persson, 2017). The mineral modal abundance is heterogeneous, which is characteristic of the Mount Rosa Na-amphibole granite. Additionally, grains can range from coarse to fine grained. Major minerals are microcline, quartz, albite, and arfvedsonite with minor amounts of biotite and zircon (Gross and Heinrich, 1965, Barker et al., 1975; Persson, 2017). Gross (1962) age dated the MRG through K^{40}/Ar^{40} methods and returned an age date of 1020-1045 Ma. Unique to the Mount Rosa Granite

is the occurrence of blobs of coarse-grained material of varying mineral abundances, coexisting with finer grained material with sharp to gradational, inconsistent boundaries within the unit, giving the impression of magma mingling.

Mafic Dikes

Volumetrically minor, the mafic dikes occur throughout the entire Mount Rosa Complex without a preferred orientation (Persson, 2017). The mineralogy includes pyroxene, biotite, quartz, albite and K-feldspar (Gross, 1962; Persson, 2017). The mafic dikes can occur as fine-grained silicic dikes or feldspar-rich, quartz-poor dikes that are generally more resistant to weathering. The mafic dikes oftentimes occur in clusters throughout the field area with a predominant makeup of hornblende diabase, clinopyroxene diabase, quartz diorite, syenite, and quartz syenite (Gross, 1962).

Pegmatites

Pegmatites within the Mount Rosa Complex have been studied as early as 1882 by Cross and Hillebrand (1882), due to the high presence of unique fluoride minerals. Gross (1962) was one of the first researchers to look at the Mount Rosa Complex as a whole, concluding that all rock types within the complex are co-magmatic. Gross (1962) subdivided the numerous pegmatites into “interior” and “exterior” pegmatites based on their physical location and host rock. Interior type pegmatites were described as being completely enclosed or in contact with the Mount Rosa Granite while exterior pegmatites are hosted in Pikes Peak granite. The pegmatites display a wide range in size and occur in clusters across the MRC (Foord and Sharp, 1984). An extensive study of the Mount Rosa area conducted by Gross (1962) included detailed mapping and descriptions of the mineralogy and petrology of all rock types. Focus was placed on the relationship between the high concentration of pegmatites, especially in the area of St. Peter’s Dome and their granitic host rocks (Gross 1962; Gross and Heinrich 1965; Gross and Heinrich 1966). Later studies classified the exterior type pegmatites of the Mount Rosa Complex as miarolitic, and potentially miarolitic-rare earth element (MI-REE) pegmatites due to their tendency to host REE-bearing accessory minerals (Foord, 1982). Martin and De Vito (2005) and Černý and Ercit (2005) classified the pegmatites in the MRC as NYF type due to their elevated concentration of Ti, Y, Sc, REE, Zr, U, Th, F and Nb > Ta.

Later research suggests the division of pegmatites in the Mount Rosa Complex into type-(I) and type-(II) pegmatites rather than interior and exterior due to their mineralogy and texture rather than host rock (Persson, 2017). Type-(I) pegmatites are composed of minerals like quartz, alkali feldspar and albite with minor amounts of biotite, Fe-Ti oxides, zircon, and Na-amphibole (Persson, 2017). They are narrow,

generally not exceeding 1 ft in width, are poor to moderately zoned, and can have irregular or well-defined contacts with the host rock. Mirolitic cavities filled with quartz and microcline can be characteristic of these pegmatites (Gross 1962). Oftentimes type-(I) pegmatites display a pinch-and-swell geometry (Persson, 2017). Additionally, type-(I) pegmatites display large opaque, red to brown euhedral zircons visible by eye (Fig. 2.4). Type-(II) pegmatites are mineralogically more complex and always display sharp contacts with the surrounding host rock. They include the same mineral assemblage observed in type-(I) pegmatites with the addition of fluoride-bearing minerals such as cryolite and an abundance of HFSE minerals, most commonly columbite. These pegmatites also host magmatic (rim) and hydrothermal zircons (core). Oftentimes, they display a brecciated texture, and can be up to 6 feet in width (Persson, 2017).



Figure 2.4: Hand sample of AS-19. Zircons can be viewed as red to brown and euhedral by eye.

2.4 Analytical Methods

The following section defines and elaborates on the analytical methods used in this study. These methods include polarized light microscopy, automated mineralogy, FE-SEM (BSE and EDS), cathodoluminescence, electron microprobe analysis, and Raman spectroscopy.

Polarized Light Microscopy

Thirty seven thin sections were studied using a polarized light microscope. Special attention was placed on the zircon morphology within each rock unit and their corresponding size, textures, and mineral

association. Also, zircon textures were noted for paragenesis and inclusions were identified when applicable. Weathering of the zircons as well as zircon concentration within each thin section was noted in order to pick the most representative thin sections for each rock unit for further analysis.

Automated Mineralogy

A sub-set of twenty one samples were analyzed using automated scanning electron microscopy in the Department of Geology and Geological Engineering at the Colorado School of Mines in Golden, Colorado, to locate zircons. The samples were loaded into the TESCAN-VEGA-3 Model LMU VP-SEM platform and the analysis was initiated using the control program TIMA3.

Four energy dispersive X-ray (EDX) spectrometers acquired spectra from minerals with a brightness between 35 and 100% with a beam stepping interval (i.e., spacing between acquisition points) of 2 μm for bright phase search scans, an accelerating voltage of 25 keV, a beam intensity of 14.3 and a working distance of 15 mm. Interactions between the beam and the sample were modeled through Monte Carlo simulation. The EDX spectra of all analysis points brighter than 35% brightness were compared with spectra held in a look-up table allowing an assignment to be made of a composition at each acquisition point. The assignment makes no distinction between mineral species and amorphous grains of similar composition. Results were output by the TIMA software as a spreadsheet giving the area percent of each composition in the look-up table. This procedure allows a compositional map to be generated. Composition assignments were grouped appropriately.

FE-SEM

The same sub-set of twenty one samples were analyzed in the FE-SEM laboratory in the Department of Geology and Geological Engineering at the Colorado School of Mines in Golden, Colorado. The laboratory is equipped with a TESCAN MIRA3 LMH Schottky field emission-scanning electron microscope. The FE-SEM features a TESCAN motorized retractable annular, single-crystal YAG backscatter electron detector and a Bruker XFlash 6/30 silicon drift detector for energy-dispersive X-ray spectrometry (EDS). Automated mineralogy bright phase search images were loaded into the MIRA3 software and cross-referenced for easy detection of relevant zircon grains. Backscatter electron imaging and EDS analysis was performed at a working distance of 10 mm, an acceleration voltage of 20 keV and a BI of 11.

Cathodoluminescence

Cathodoluminescence (CL) imaging was performed at the United States Geological Survey Denver Microbeam Laboratory in Lakewood, Colorado. All images focused on the zircons of interest in the same

21 thin sections used for automated mineralogy and BSE imaging and EDS analysis. The instrument used was a JEOL 5800LV electron microscope equipped with a cold cathode CL detector. The system ran at 15 kV during imaging.

Electron Probe Microanalyses (EMPA)

Major, minor and trace element analysis of zircons from 15 samples were performed at the Electron Microprobe Laboratory located in the Geological Sciences building at the University of Colorado Boulder in Boulder, Colorado. A JEOL-JXA-8230 was used to analyze for 21 elements. Calibration of the instrument using 17 standards (natural and synthetic) took place prior to analysis. The standards consist of the following: Natural (Zr,Hf)SiO₄ for Si and Zr, natural Fe₃Al₂Si₃O₁₂ (Almandine NY) for Al and Fe, natural Ca₅(PO₄)₃(OH,F) for Ca and P (Apatite Wilberforce), natural CaMgSi₂O₆ for Mg (Diopside), natural SnO₂ for Sn (Cassiterite), natural MnSiO₃ for Mn (Rhodonite), synthetic ThO₂ for Th, synthetic UO₂ for U, synthetic HfO₂ for Hf, synthetic YbPO₄ for Yb, synthetic SmPO₄ for Sm synthetic ErPO₄ for Er, synthetic DyPO₄ for Dy, synthetic PrPO₄ for Pr, synthetic NdPO₄ for Nd, synthetic CePO₄ for Ce, and synthetic YPO₄ for Y. Standards were calibrated to 5 spectrometers: Mg, Al, and Y were analyzed using spectrometer 1 (TAP), Ca, Sn, U, Th, and P were analyzed using spectrometer 2 (TAP-L), Er, Yb, and Hf were analyzed using spectrometer 3 (PET-L), Sm, Fe, Dy, and Cd were analyzed using spectrometer 4 (LiF-L), and Ce, Nd, Pr, and Mn were analyzed using spectrometer 5 (LiF-L). Samples were run at 15 kv with a beam current of 50 nA and spot size of 5 µm. Special attention was paid to the P Kβ and Zr Lβ peak overlap. A spot size of 1 micron was selected using BSE and CL images collected prior to analysis. Element maps for P, Hf, Fe, and Y were taken on three zircons. For calibration, Y was assigned both spectrometers 1 and 2 (TAP and TAP-L) for optimization, P was assigned spectrometer 3 (PET-L), Hf was assigned spectrometer 4 (LiF-L) and Fe was assigned spectrometer 5 (LiF-L). This method is semi-quantitative using the assumption of a fixed Si content of 15 elemental weight percent, which calculated the Zr content by difference for the background correction. Detection limits and standard deviation is displayed in table 2.1.

Raman Spectroscopy

Micro-Raman spectroscopy was performed on select zircons found in 8 thin sections using an upright Olympus BX10 microscope with a 50X objective and 632 nm HeNe laser located in the Department of Physics at the University of Colorado Boulder in Boulder, Colorado. The system is home-built with a 1 mW sample focus and f = 500 mm imaging spectrograph (Princeton Instruments spectrometer Acton SP500 with a PIXIX 100 liquid nitrogen cooled CCD camera). The system was calibrated on multiple spectral lines using a He-lamp.

Table 2.1: Detection limits and standard deviations for each element analyzed

	Crystalline Zircon	Metamict Zircon
Al		
Detection Limit (ppm)	30	30
Standard Deviation	24	5
Mg		
Detection Limit (ppm)	30	30
Standard Deviation	46	15
Th		
Detection Limit (ppm)	300	300
Standard Deviation	33	21
U		
Detection Limit (ppm)	250	250
Standard Deviation	51	8
Sn		
Detection Limit (ppm)	110	110
Standard Deviation	79	75
Ca		
Detection Limit (ppm)	40	40
Standard Deviation	13	1
Hf		
Detection Limit (ppm)	210	210
Standard Deviation	1	2
Fe		
Detection Limit (ppm)	70	70
Standard Deviation	5	1
Mn		
Detection Limit (ppm)	60	60
Standard Deviation	65	2
P		
Detection Limit (ppm)	560	560
Standard Deviation	29	25
Σ (REE, Y)		
Detection Limit (ppm)	330	330
Standard Deviation	145	202

2.5 Results

In total, 37 polished thin sections were used to conduct this study (Table 2.2). All samples are representative of the major rock types in the Mount Rosa Complex (MRC) and were used to characterize the corresponding zircons and associated minerals unique to each rock type. Transmitted light

petrography and automated mineralogy bright phase search scans were performed first to map out zircons within each thin section and detail their morphology, mineral association, and metamictization/alteration.

Following the initial thin section microscopy and automated mineralogy, select samples (21 thin sections in total) were analyzed using backscattered electron (BSE) and cathodoluminescence (CL) imaging to identify zoning within zircon crystals. Additionally, EDS analyses were used to identify inclusions within zircons and understand the major and minor element chemistry within individual zircon grains from different rock units.

Additionally, a subset of 16 thin sections was selected to represent all different rock units and corresponding zircon types for electron probe microanalysis. Finally, based on the outcome of the electron probe microanalysis results, 8 samples were selected for Raman analysis.

2.5.1 Petrography

Pikes Peak Granite

The zircons in the PPG are distributed heterogeneously among thin sections (Fig. 2.5). They generally occur in clusters as inclusions in biotite grains, but some are hosted in quartz. Zircons within the PPG are relatively small compared to other zircons within the MRC, ranging between 50 and 100µm in size. Optically, these zircons display concentric zoning, are clear to a light dirty brown in plane polarized light (PPL) and display bright second order birefringence in crossed polarized light (XPL; Fig. 2.6). PPG zircons are euhedral with rare inclusions, and were one of the first minerals to crystallize.

Concentric zoning is evident in most zircons and easily viewed in backscattered electron (BSE) images (Fig. 2.7) and SEM-CL (Fig. 2.8). Occasionally the cores present as patchy. Inclusions of monazite, ilmenite, and quartz can be found throughout zircons without a specific zone to be hosted in, but overall inclusions are rare (Figs. 2.7B and E). Rarely, some metamict cores are very inclusion rich and are dark in BSE images (Figs. 2.7B and E) and SEM-CL images (Figs. 2.8B and E). Inclusions in metamict cores comprise U-rich thorite, U/Th-rich Fe-oxides, allanite, and xenotime. Fracturing network outward from the metamict core into lighter zones of zircon is common.

Phosphate minerals such as monazite and xenotime occur throughout the thin section, are fairly rare, and can commonly be found in zircon grains. They exhibit euhedral grain boundaries and can often

be found associated with Nb-bearing minerals, most commonly columbite. Nb-bearing minerals crystallized near the beginning of the sequence, likely co-crystallizing with early magmatic zircon.

Table 2.2: Summary of all samples used in this study.

Sample	UTM North	UTM East	Rock Type	Thin Section Microscopy	FE-SEM	Automated Mineralogy	SEM-CL	EMPA	Raman
MR01	38.74611	104.9436	Pikes Peak Granite	✓	✓	✓	✓	✓	✓
MR09	38.7767	104.9326	Pikes Peak Granite	✓	✓	✓	✓		
MR34	38.747	104.9268	Pikes Peak Granite	✓	✓	✓	✓		
MR-2016-18	38.79128	104.9053	Pikes Peak Granite	✓					
MR14	38.75972	104.9308	Fayalite-bearing Quartz Syenite	✓					
MR31	38.7425	104.9128	Fayalite-bearing Quartz Syenite	✓	✓	✓	✓	✓	
MR30	38.7425	104.9128	Granitic Dike	✓	✓	✓	✓	✓	
MR37	38.755	104.905	Granitic Dike	✓					
MR03	38.74605	104.9442	Mount Rosa Granite	✓					
MR04	38.7444	104.9458	Mount Rosa Granite	✓					
MR06A	38.76667	104.9364	Mount Rosa Granite	✓					
MR06B	38.76667	104.9364	Mount Rosa Granite	✓					
MR16	38.74639	104.9394	Mount Rosa Granite	✓					
MR25	38.75833	104.9058	Mount Rosa Granite	✓	✓	✓	✓	✓	✓
MR-2016-06	38.76111	104.9467	Mount Rosa Granite	✓					
MR-2016-07	38.7542	104.9479	Mount Rosa Granite	✓	✓	✓	✓	✓	✓
MR-2016-08	38.7506	104.9502	Mount Rosa Granite	✓					
MR-2016-10	38.74556	104.9542	Mount Rosa Granite	✓					
MR-2016-13	38.7721	104.9082	Mount Rosa Granite	✓	✓	✓	✓	✓	✓
MR10	38.77556	104.9328	Mafic Dike	✓					
MR11	38.96922	104.9369	Mafic Dike	✓					
MR26	38.7583	104.9058	Mafic Dike	✓					
MR58	38.76856	104.9377	Mafic Dike	✓	✓	✓	✓	✓	
MR-2016-15	38.75706	104.9132	Mafic Dike	✓					
MR-2016-17	38.75712	104.9128	Mafic Dike	✓					
AS-18	38.74611	104.9436	Type I Pegmatite	✓	✓	✓			
AS-19	38.74611	104.9436	Type I Pegmatite	✓	✓	✓	✓	✓	✓
AS-MR38-01	38.7522	104.9064	Type II Pegmatite	✓	✓	✓	✓	✓	
AS-MR38-02	38.7522	104.9064	Type II Pegmatite	✓	✓	✓	✓		
AS-MR38-03	38.7522	104.9064	Type II Pegmatite	✓	✓	✓	✓	✓	✓
AS-MR38-04	38.7522	104.9064	Type II Pegmatite	✓	✓	✓	✓	✓	
AS-MR38-05	38.7522	104.9064	Type II Pegmatite	✓	✓	✓	✓	✓	✓
AS-MR38-06	38.7522	104.9064	Type II Pegmatite	✓	✓	✓	✓		
AS-MR38-07	38.7522	104.9064	Type II Pegmatite	✓	✓	✓	✓	✓	✓
AS-MR38-08	38.7522	104.9064	Type II Pegmatite	✓	✓	✓	✓	✓	
AS-MR38-09	38.7522	104.9064	Type II Pegmatite	✓	✓	✓	✓	✓	
AS-MR38-10	38.7522	104.9064	Type II Pegmatite	✓	✓	✓	✓	✓	

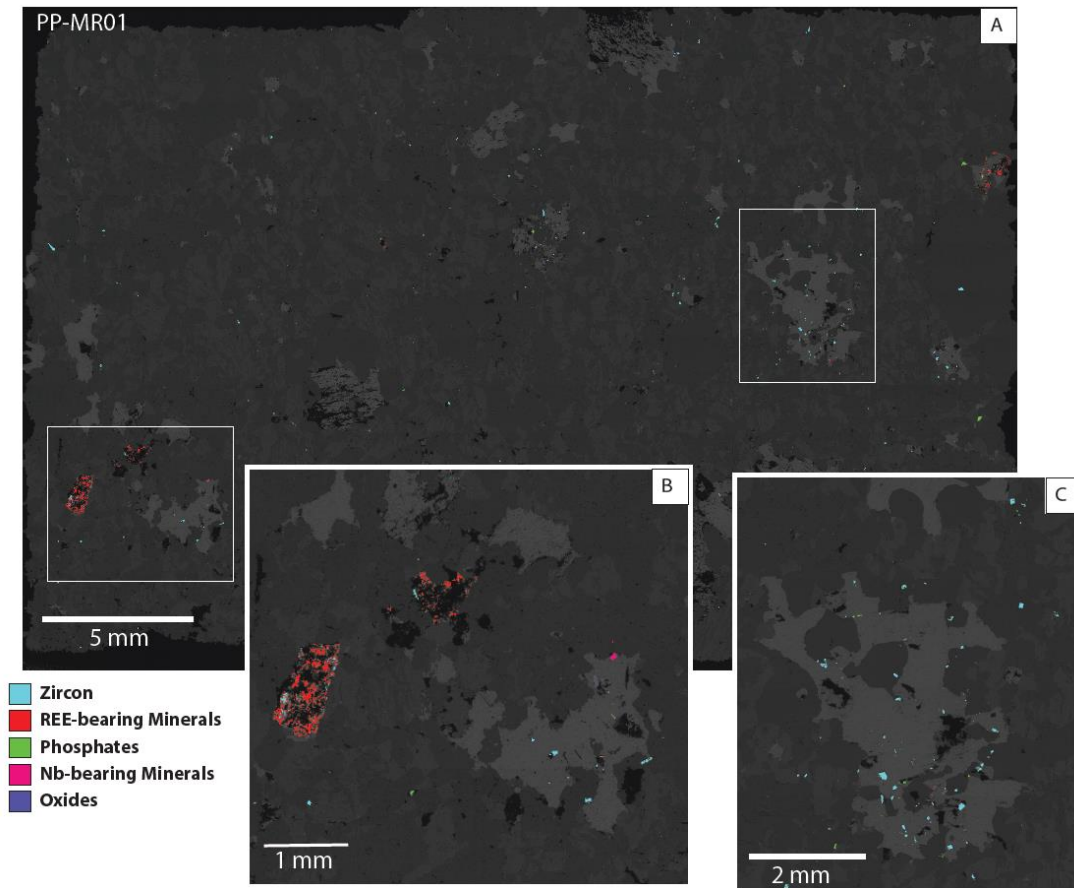


Figure 2.5: Bright phase scan of Pike Peak Granite, thin section PP-MR01. The group phosphates (green) represents xenotime and monazite, while all other REE-bearing minerals are red (parasite, bastnasite, and allanite). (A) Overview scan of thin section PP-MR01, (B) close-up image displaying REE-minerals replacing biotite phenocrysts, (C) close-up image showing zircon association with biotite.

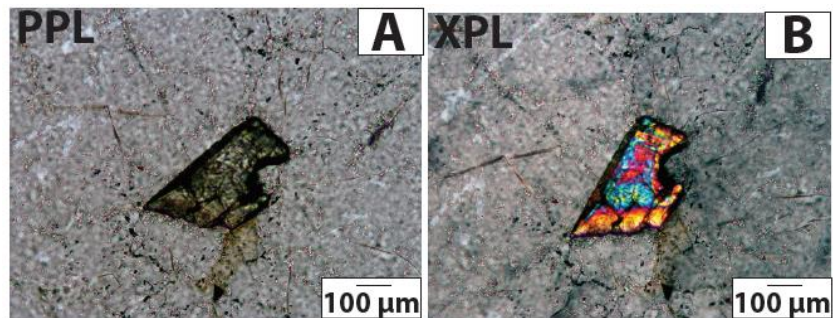


Figure 2.6: Pikes Peak Granite zircon viewed in plane polarized light (A) and cross polarized light (B).

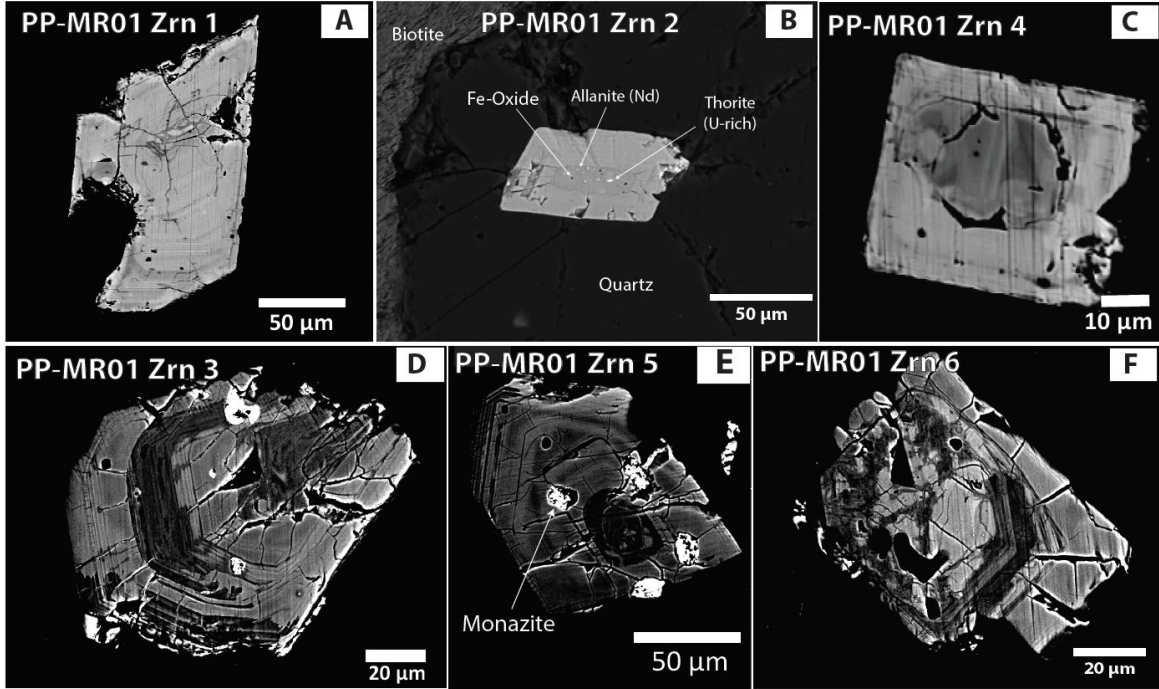


Figure 2.7: BSE images of zircons found in the Pikes Peak Granite. (A) Concentric zoned zircon with small core, (B) inclusion-rich metamict core with radial fractures rimward, (C) patchy, large core with little concentric zoning observed throughout the zircon, (D) broken, segmented zircon with metamict zones (darker areas), (E) concentric zoned zircon with metamict core and monazite inclusions, (F) patchy zircon core with metamict zones (dark areas) creating radial fractures.

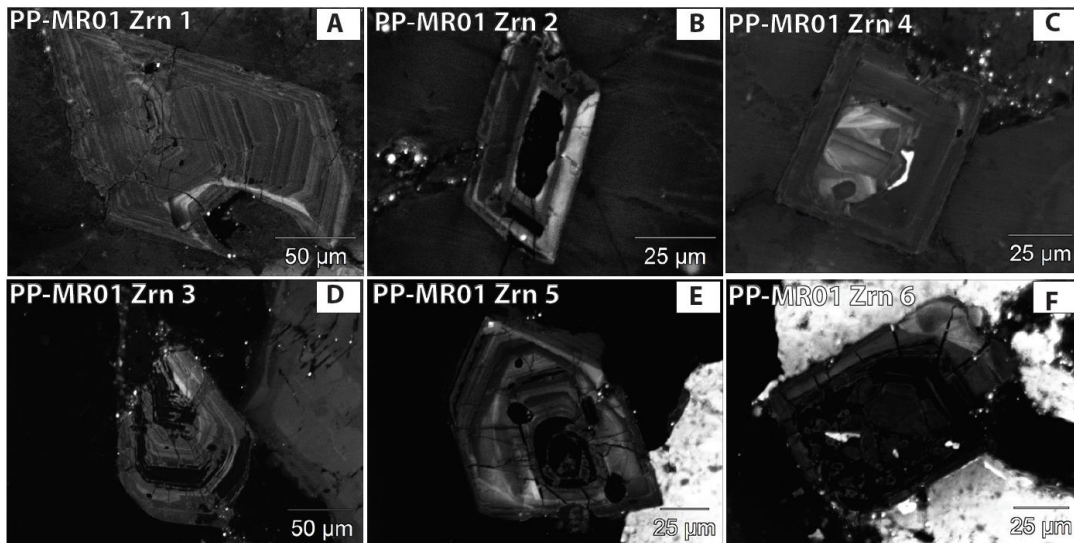


Figure 2.8: CL images of the same zircons viewed in Fig. 2.7. (A) Concentric zoned zircon with a small, dark undisturbed core, (B) dark unreactive core surrounded by a mostly unreactive rim, (C) large reactive patchy core surrounded by an unreactive rim, (D) concentric zoning with dark metamict zones, (E) concentric zoning with dark monazite inclusions, (F) mostly dark zircon with a thin reactive rim.

Fayalite-bearing Quartz Syenite

Zircons in the Fayalite-bearing Quartz Syenite occur solely in biotite grains, distributed evenly throughout the sample. The zircons are euhedral and relatively small, ranging between 50 and 100 μm . Overall, these zircons lack inclusions and were one of the first minerals to crystallize. Optically, the zircons are transparent in PPL with second order birefringence, and do not display zoning (Fig. 2.9). A combination of patchy and concentric zoning does become evident when taking BSE images (Fig. 2.10) and CL images (Fig. 2.11). Where concentric zoning is present, a central core is present, but the cores are small relative to cores of zircons observed in other units (Figs. 2.11C, D, and E). Some zircons display patchy zoning, causing a centralized core to be unrecognizable (Fig. 2.10A). Rare inclusions consist of monazite, xenotime, and apatite.

Y-rich REE minerals (mostly bastnasite and parisite), xenotime, and monazite are commonly observed and, like zircon, usually occur as inclusions in biotite (Fig. 2.12). Subordinate Nb-bearing minerals (primarily columbite) seem to have crystallized early, due to their euhedral grain boundaries and relatively similar size as the zircons.

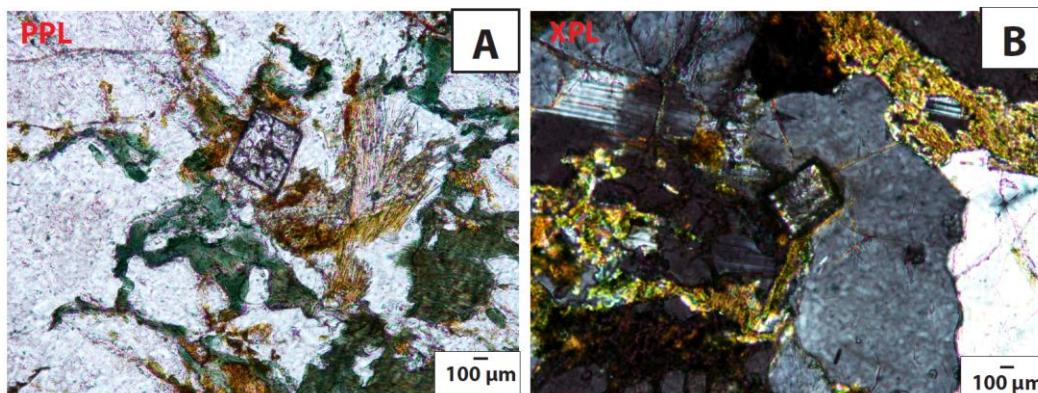


Figure 2.9: Fayalite-bearing quartz syenite zircon viewed in plane polarized light (A) and cross polarized light (B).

Granitic Dikes

The granitic dikes are volumetrically minor compared to other rock units in the MRC. Zircons are rare in this unit, but occur homogeneously throughout the sample. The few zircons present are small

(between 40-100 μm) subhedral phenocrysts that displays as light to dark brown optically (Fig. 2.13). Zircon was one of the first minerals to crystallize, and contains inclusions.

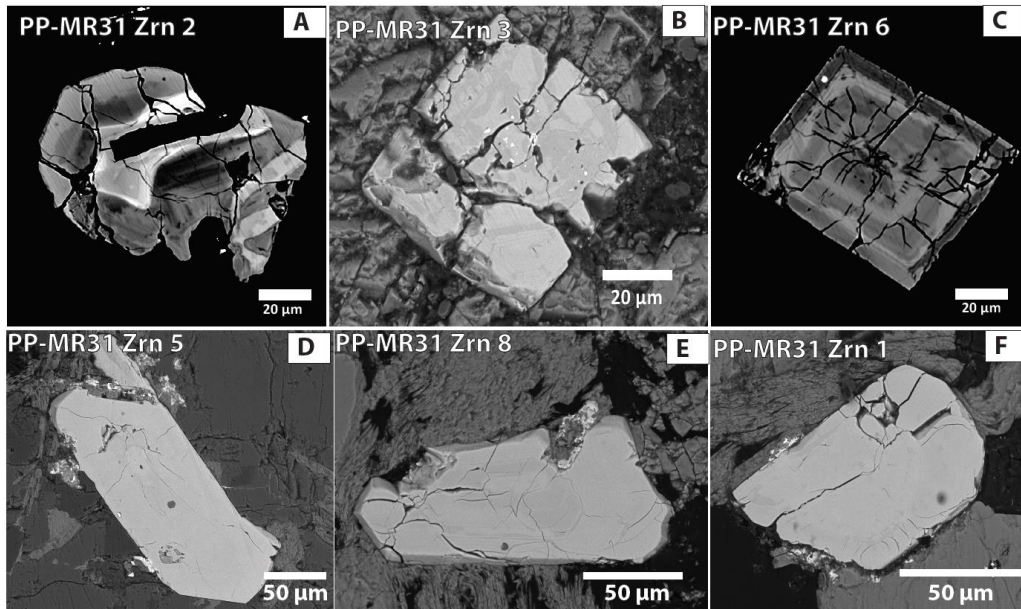


Figure 2.10: BSE images of zircons found in the fayalite-bearing quartz syenite. (A) Patchy zoned zircon without an obvious core, (B) patchy zoned zircon with monazite and xenotime inclusions concentrated in the core, (C) euhedral, concentric zoned, inclusion free zircon, (D) zircon hosted in biotite and K-feldspar, (E) slightly fractured zircon hosted in biotite, (F) inclusion free zircon with small rimward fractures.

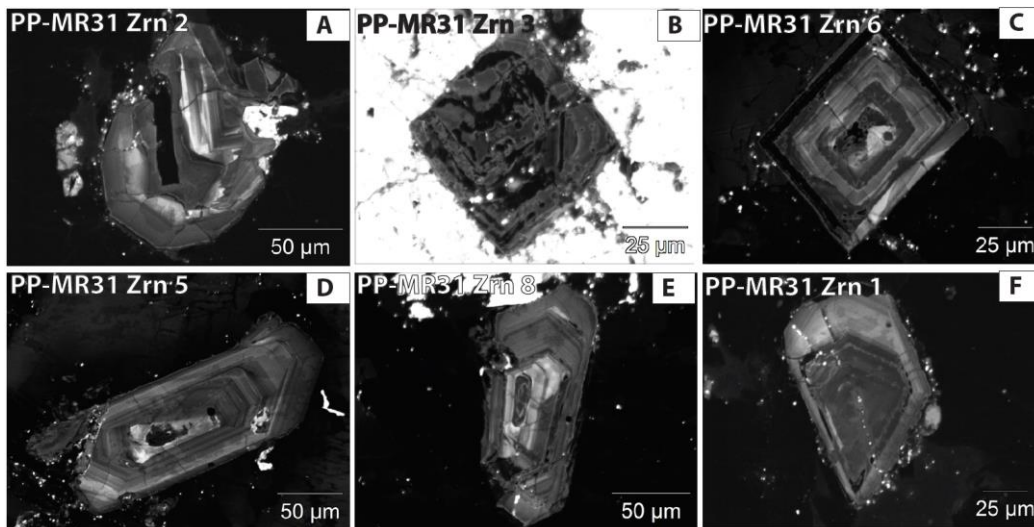


Figure 2.11: CL images of the same zircons imaged in Fig. 2.10. (A) Patchy zircon with no noticeable core, (B) patchy zircon with little reactivity, (C) concentric reactive zones with a partially reactive core, (D) concentric reactive zones with an unreactive, small core, (E) concentric zoned zircon with an partially reactive small core, (F) partially reactive large core surrounded by a more reactive rim.

When viewed optically (Fig. 2.13) and looking at BSE images (Fig. 2.14), these grains display little to no zoning. Additionally, CL reactivity was low for these zircons (Fig. 2.15) and only rarely revealed patchy zonation (Fig. 2.14C). EDS analyses of the inclusions identify primarily U-rich thorite, monazite, xenotime, biotite, and albite (Fig. 2.14A). Crystallization of later stage REE-bearing fluoride mineral can be detected on grain boundaries. Subordinate euhedral Nb-bearing minerals (primarily columbite) seem to have crystallized around the same time as zircon.

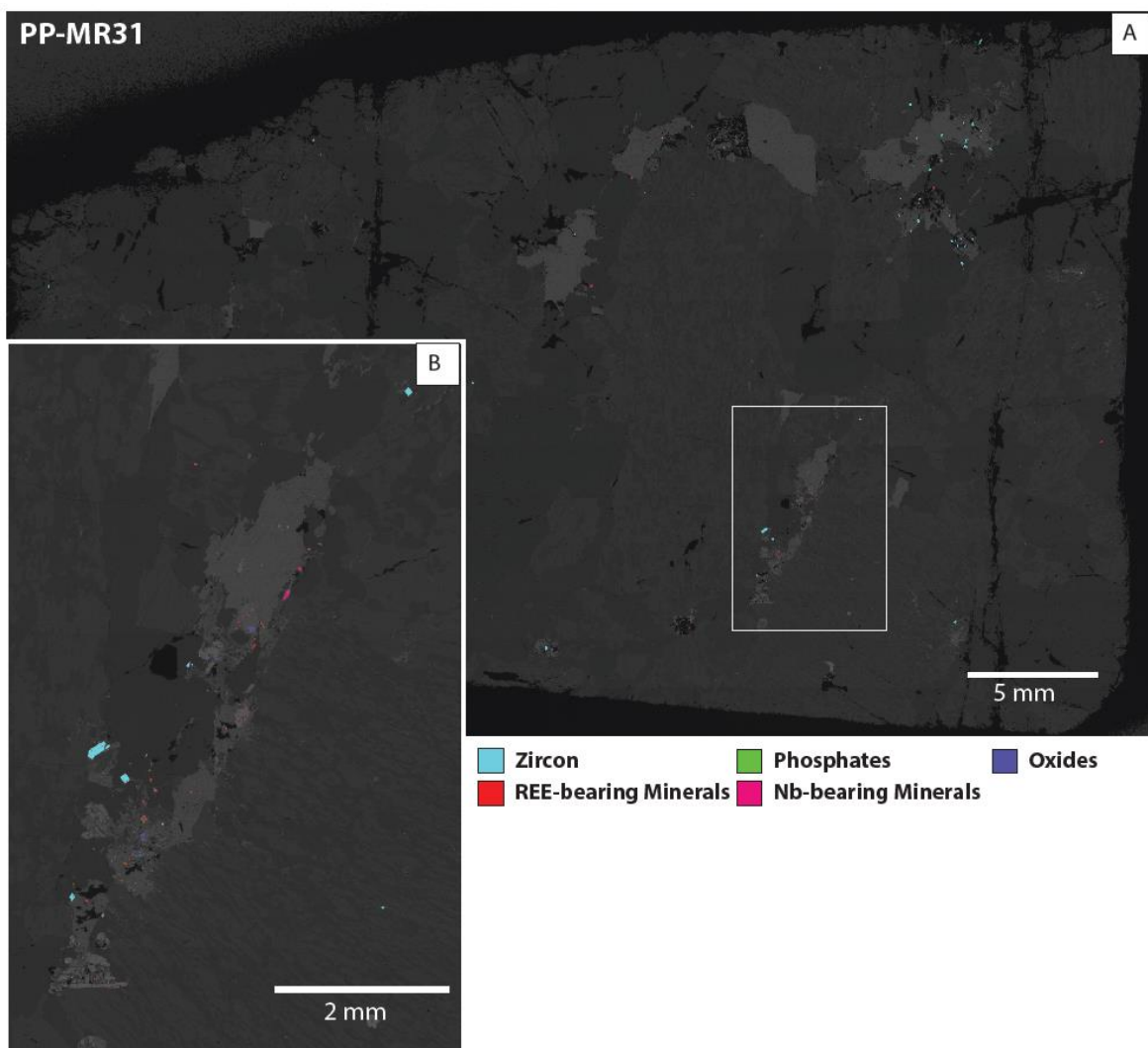


Figure 2.12: Bright phase scan of fayalite bearing quartz syenite, thin section PP-MR31. The group phosphates (green) represents xenotime and monazite, while all other REE-bearing minerals are red (parasite, bastnasite, and allanite). (A) Overview scan of thin section PP-MR31, (B) close-up image displaying euhedral zircon, phosphate, and Nb-bearing minerals hosted with a biotite phenocryst.

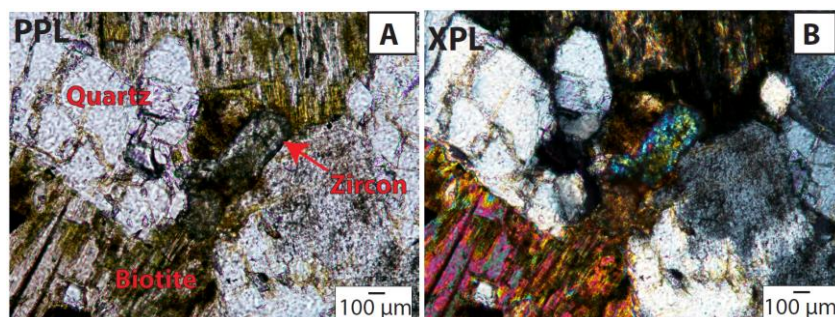


Figure 2.13: Granitic dike zircon viewed in plane polarized light (A) and cross polarized light (B).

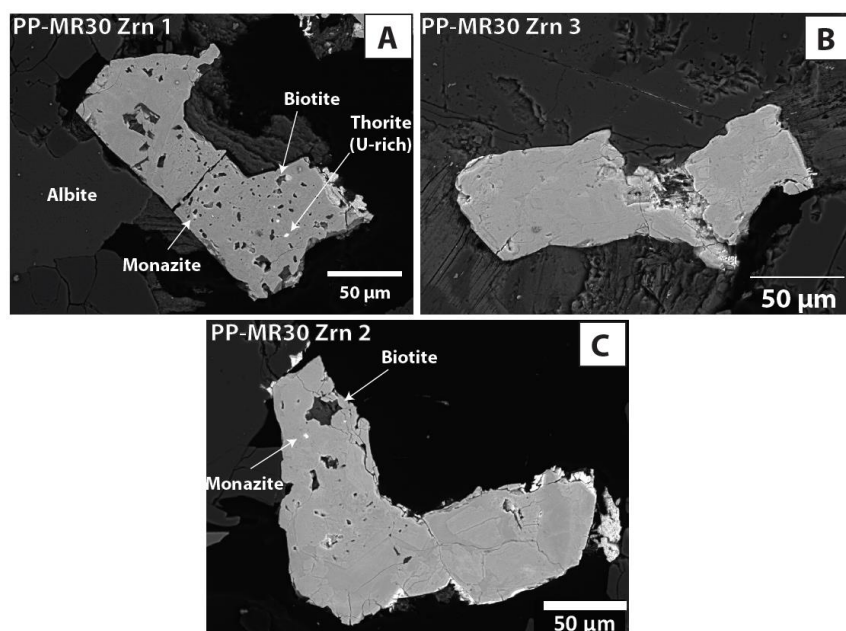


Figure 2.14: BSE images of zircons in the Granitic Dikes. (A) Inclusion-rich subhedral zircon, (B) subhedral zircon with no inclusions, (C) subhedral zircon with minor inclusions and patchy zoning.

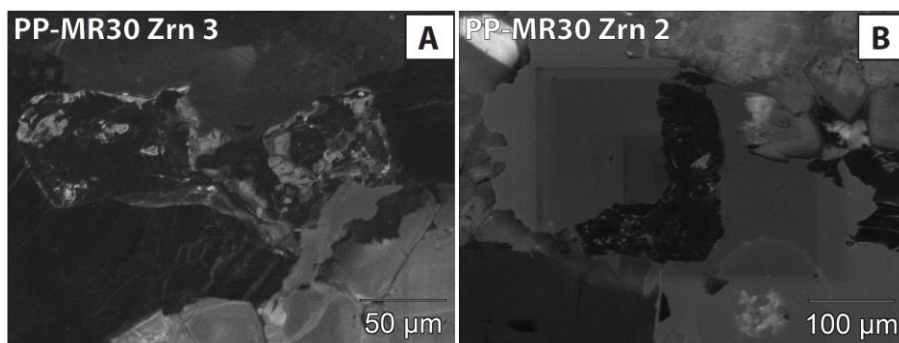


Figure 2.15: CL images of zircon 2 and 3 seen in Fig. 2.14 in the Granitic Dikes. (A) Patchy reactivity of zircon 3, (B) no reactivity, which is characteristic of most zircons in thin section PP-MR30.

Mount Rosa Granite

Most zircons in the MRG are heterogeneously distributed, typically crystallizing in clusters. Two distinct zircon types, herein referred to as sieved zircon and patchy zircon occur. It is important to note that the two different zircon types do not co-occur within one sample, but are exclusive of one another. Sieved zircons are large relative to others within the MRC, ranging between 200 and >500 μm , and scattered abundantly throughout the thin sections (Fig. 2.16). The outer rims display lower birefringence than the cores, but this can be difficult to discern due to the overall brown nature of the zircons (Fig. 2.17).

In BSE imaging, they display as euhedral, but occasionally can be classified as skeletal (Fig. 2.18). These zircons are very rich in large inclusions (up to 100 μm), which are generally anhedral, mineralogically simple, and create a sieve texture. The inclusions are primarily composed of biotite, K-feldspar, albite, quartz and Na-amphibole. In CL, the inclusions oftentimes display a bright reactive halo around them (Fig. 2.19). In some areas towards the outer layer of the zircons, some very faint zoning can be detected (more illuminated in CL) but is quickly disrupted by the presence of inclusions.

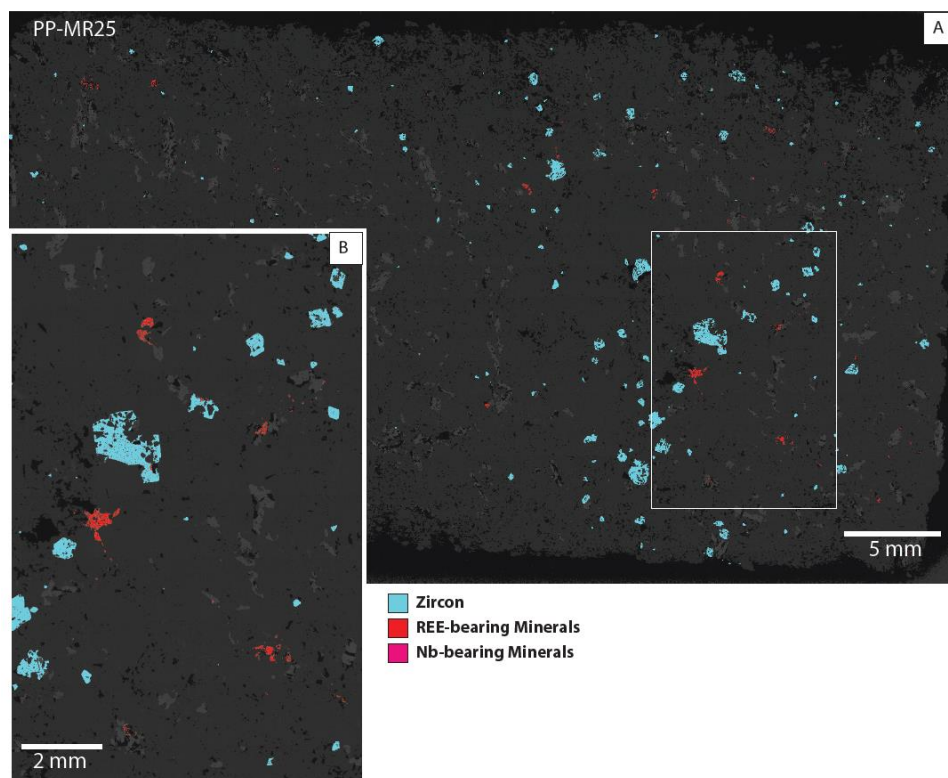


Figure 2.16: Bright phase scan of the thin section PP-MR25 highlighting sieve zircons. REE-bearing minerals are red (parasite and bastnasite) with pink Nb-bearing minerals (columbite). (A) Overview scan of thin section PP-MR25, (B) close-up image displaying inclusion rich-zircon with anhedral REE-bearing minerals.

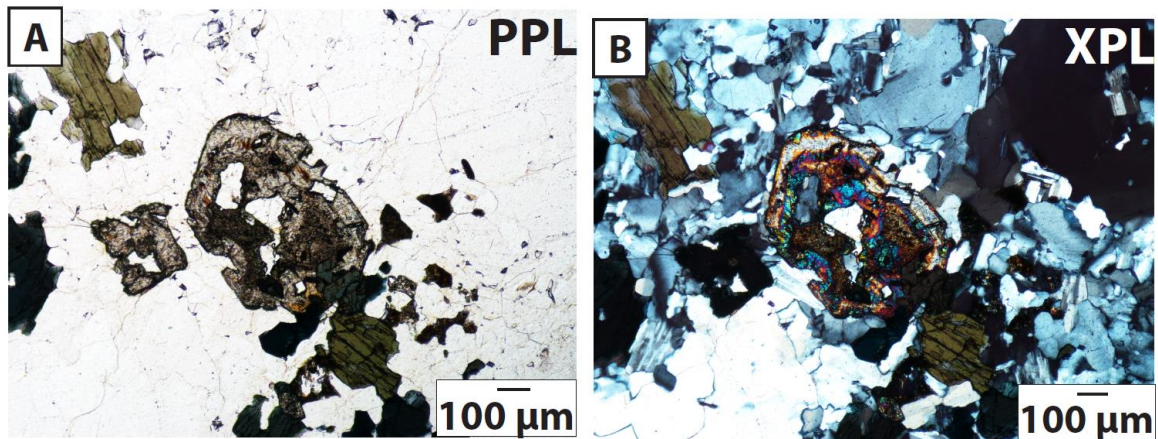


Figure 2.17: Mount Rosa Granite sieved zircon viewed in plane polarized light (A) and cross polarized light (B).

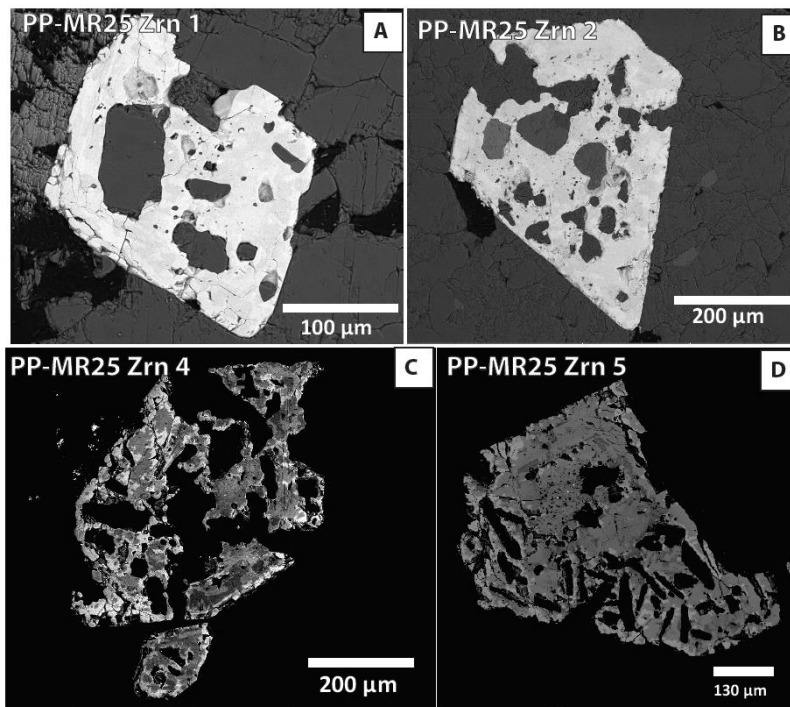


Figure 2.18: BSE images of sieved zircon within the Mount Rosa Granite. (A) Euhedral zircon crystal with anhedral mineral inclusions, (B) euhedral zircon with anhedral mineral inclusions, (C) abundant inclusions crosscutting a patchy zoned zircon, (D) subhedral zircon with elongated anhedral inclusions with slight patchy zonation.

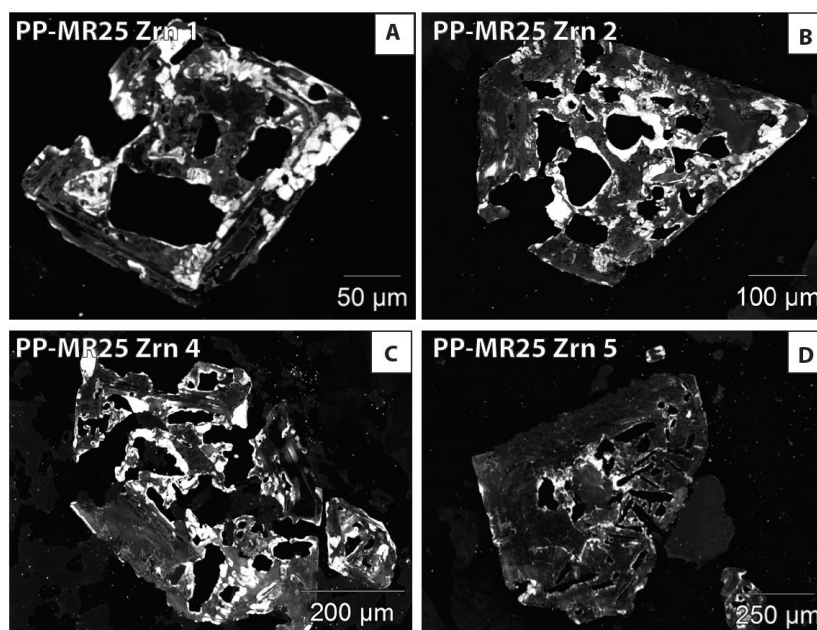


Figure 2.19: CL images of the same sieved zircon viewed in Fig. 2.18 within the Mount Rosa Granite. (A) Reactive rim and slight reactivity around inclusions, (B) reactive halos around mineral inclusions within a mostly unreactive zircon, (C) reactive halos around inclusions and patchy zircon zonation, (D) unreactive zircon aside from the core.

Patchy zircons are smaller than the sieve zircons, but overall large relative to the zircons observed in other rock units of the MRC, between 100-150 µm. Patchy zircons display as euhedral to subhedral without a particular mineral association (Fig. 2.20). Optically, these zircons are similar in that they display a light to dark brown profile in PPL with varying shades based on zones (Fig. 2.21). Inclusions are small, euhedral to subhedral, and occur throughout the zircons. The majority of the inclusions are composed of quartz, biotite, U-rich thorite, Th-bearing Fe-oxide, monazite, and yttrifluorite. Zoning in the patchy zircons can be observed optically but is much more evident in BSE (Fig. 2.22) and CL images (Fig. 2.23). Some zircons exhibit concentric zoning (Fig. 2.23E) however, the majority of the zircons display erratic patchy zoning with patchy cores (Fig. 2.22A, B and C). Metamict areas display as dark gray to black on BSE and CL images. Oftentimes, fractures radiate outward throughout the grain into the lighter gray areas. EDS spot analyses revealed that those metamict zones have notably high Fe content.

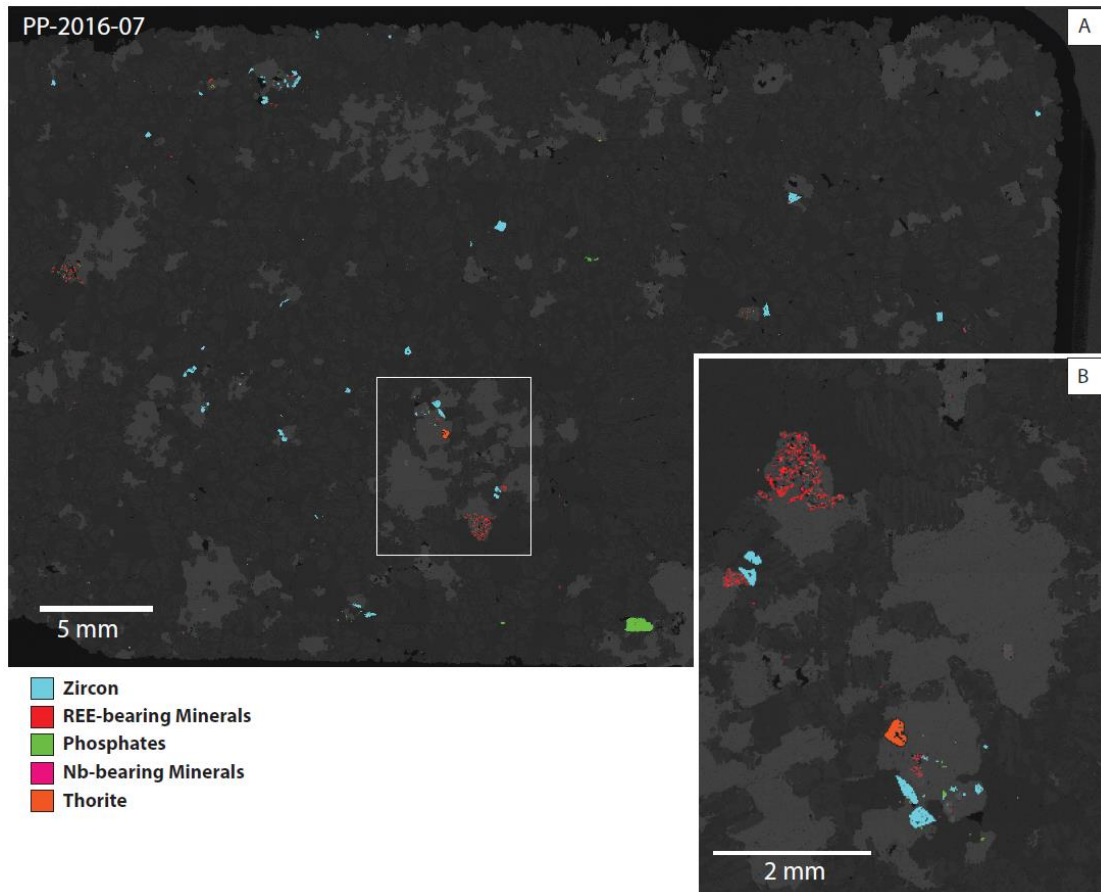


Figure 2.20: Bright phase scan of the thin section PP-2016-07 highlighting patchy zircons. Phosphate minerals (xenotime and monazite) are outlined in green, REE-bearing minerals are red (parasite and bastnasite), and pink represents Nb-bearing minerals (columbite). (A) Overview scan of thin section PP-2016-07, (B) close-up image of euhedral zircon concentrated in biotite with thorite and anhedral REE-bearing minerals replacing biotite.

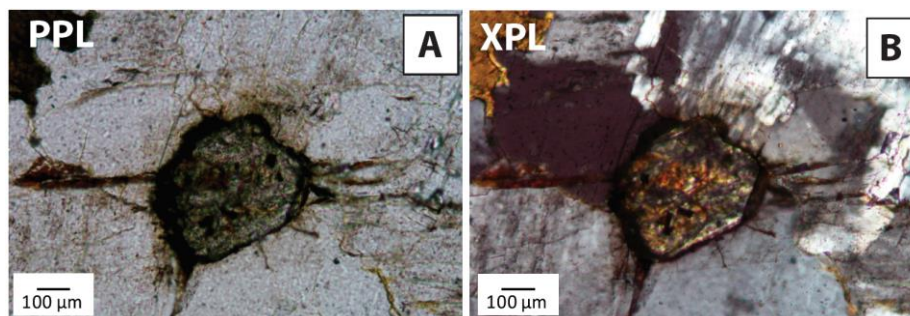


Figure 2.21: Mount Rosa Granite patchy zircon viewed in plane polarized light (A) and cross polarized light (B).

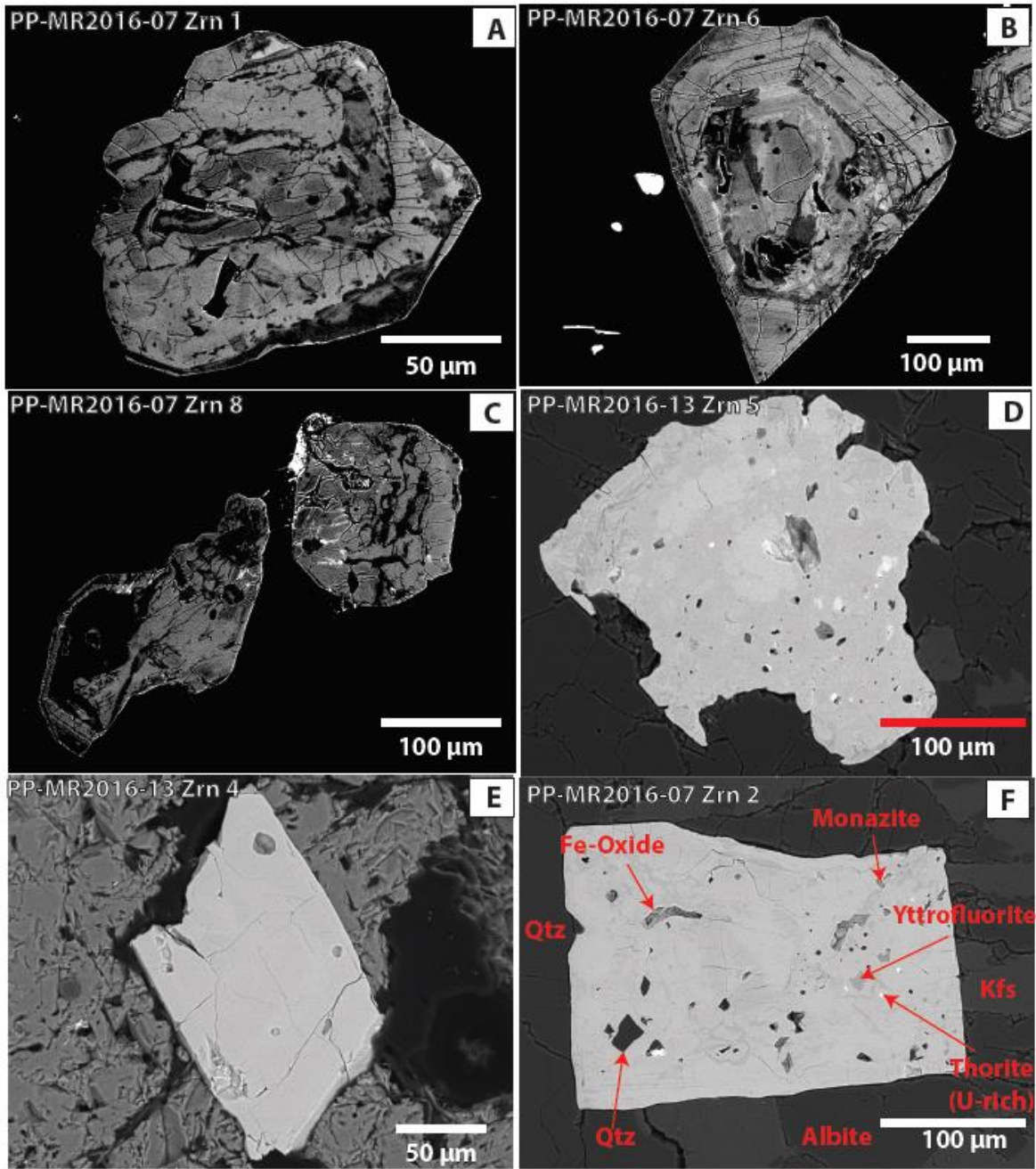


Figure 2.22: BSE images of Mount Rosa granite patchy zircon. (A) Patchy zoned zircon with fractures radiating from darker metamict zones, (B) patchy zoned zircon with concentrated fractures in the rim and a patchy core, (C) two small patchy zoned zircons, (D) inclusion rich zircon with patchy zonation, (E) mostly inclusion-free zircon hosted in biotite, (F) abundant inclusions within euhedral zircon grain

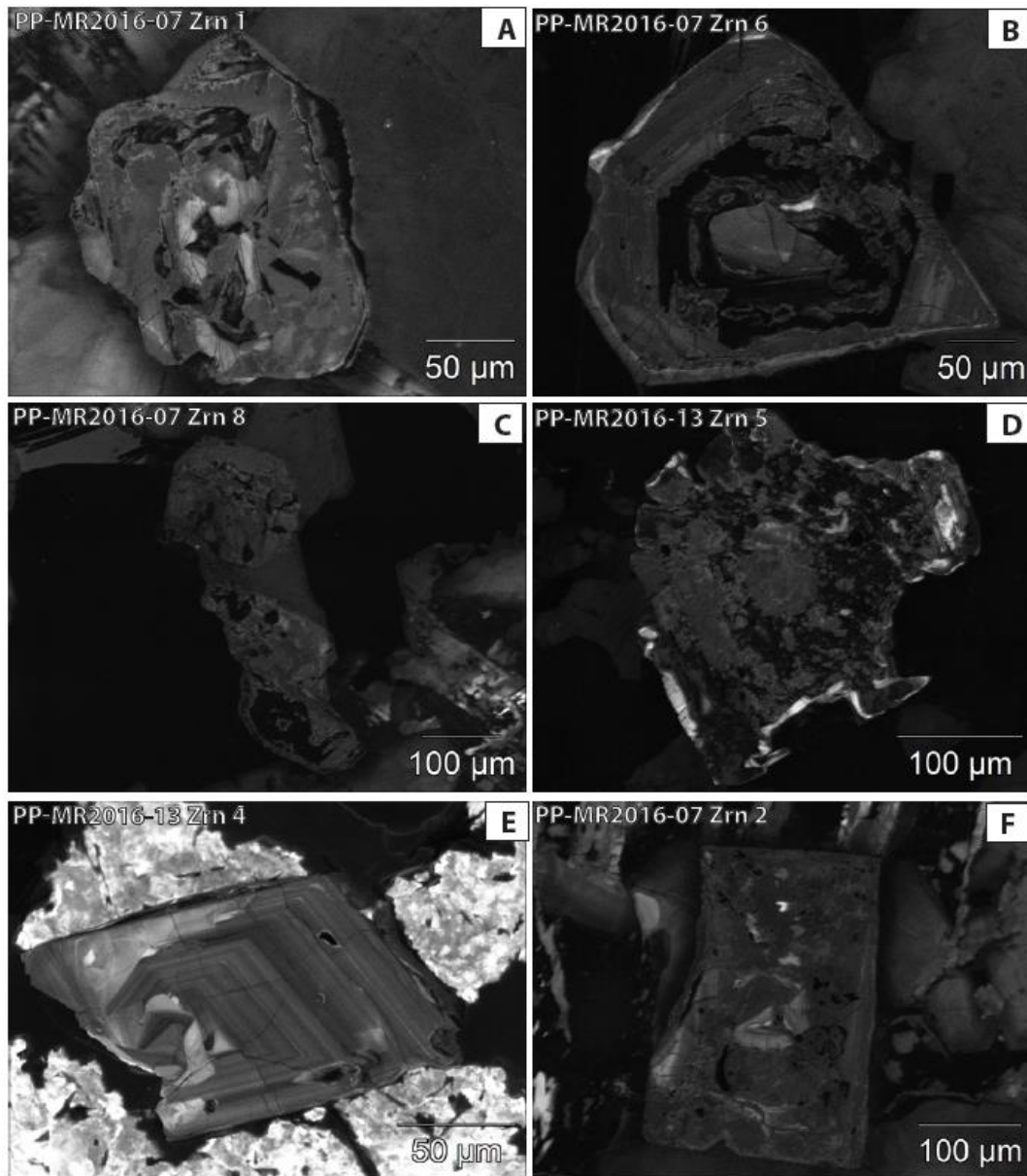


Figure 2.23: CL images of the same zircons in Fig. 2.22 of Mount Rosa Granite patchy zircon. (A) Patchy zircon reactivity with no reactivity in the metamict zones, (B) core surrounded by unreactive metamict zone and concentric zoned rim, (C) mostly unreactive smaller zircon crystals, (D) patchy reactive zircon without inclusion influence, (E) concentric zoned, reactive zircon, (F) patchy reactive core with mostly unreactive rim.

Mafic Dikes

Zircons from the mafic dike samples generally range between 20 and 75µm, making them some of the smallest zircons in the MRC. Unlike other rock units, these zircons do not display any type of preferred mineral association and are dispersed homogeneously throughout the thin section (Fig. 2.24).

Due to their small nature, optically these zircons could not be described in detail. These zircons range between euhedral to subhedral and are near the middle of the crystallization sequence. BSE imaging and automated mineralogy bright phase images revealed an extremely high concentration of inclusions, typically scattered throughout the entire zircon (Fig. 2.25). Oftentimes, these zircons display a sieve texture. SEM-CL images display high reactivity for these zircons (Fig. 2.26).

Most of the zircons display a darker core, with a lighter outer rim using both BSE and CL techniques with the exception of zircon 1 in sample MR58, which displays multiple growth zones (Figs. 2.25A and 2.26A). This zircon also contains abundant inclusions throughout the crystal rather than inclusions restricted and concentrated in the core. Inclusions dominantly consist of parasite, allanite, and bastnasite and columbite.

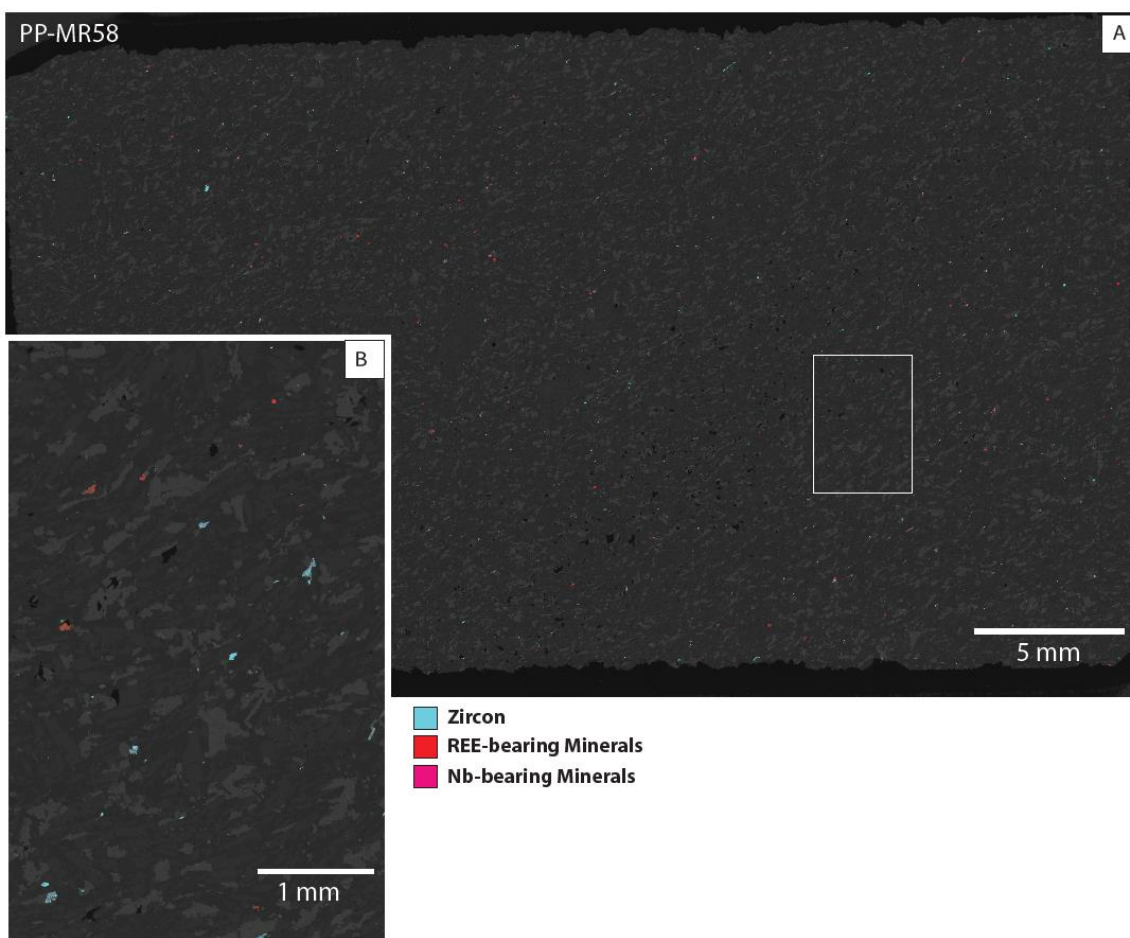


Figure 2.24: Bright phase scan of a mafic dike, represented by thin section PP-MR58. REE-bearing minerals are red (parasite, allanite, and bastnasite) with pink Nb-bearing minerals (columbite). (A) Overview scan of thin section PP-MR58, (B) close-up image displaying even distribution of zircon and REE-bearing minerals

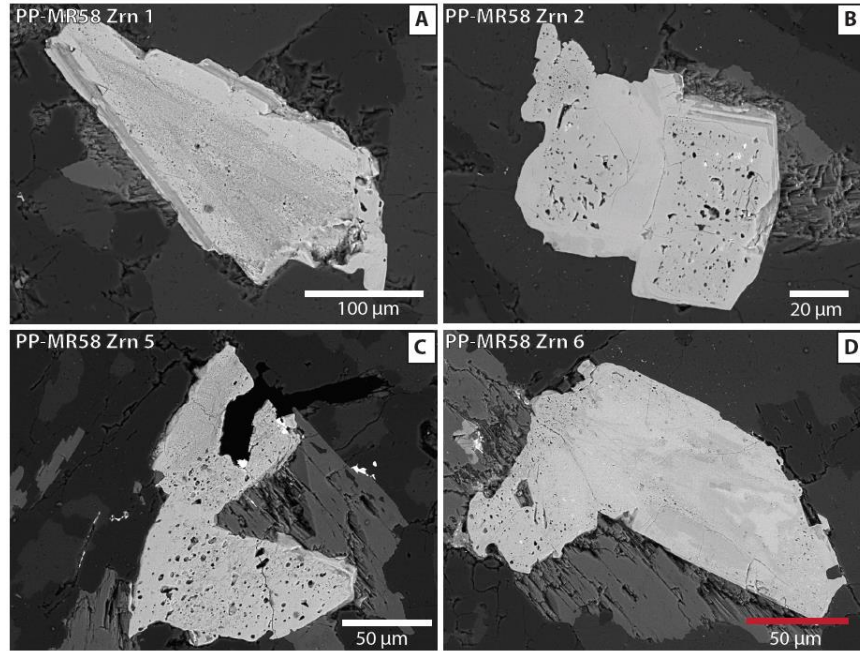


Figure 2.25: BSE images of zircons found within the mafic dike. (A) Zoned zircon with inclusions distributed throughout the crystal, (B) zircon with inclusions concentrated at the core and dark parts of the rim, (C) unzoned zircon with a high inclusion concentration, (D) patchy zoned zircon with inclusions concentrated at the rim.

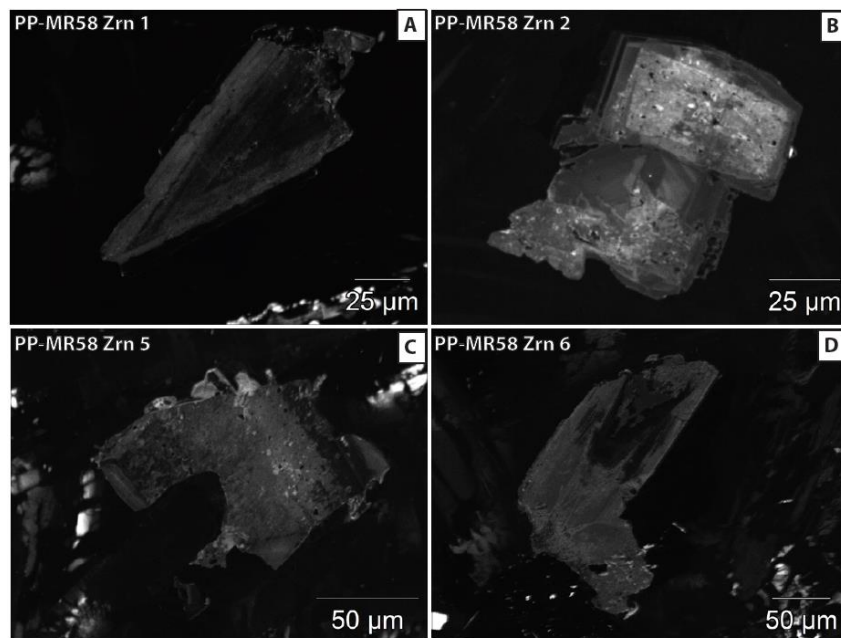


Figure 2.26: CL images of the same zircons viewed in Fig. 2.25 found within the mafic dike. (A) Unreactive core with a more reactive rim, (B) highly reactive core with a moderately reactive rim, (C) patchy zoned zircon with minor reactivity, (D) unreactive core with a moderately reactive rim.

Type-(I) Pegmatite

Thin sections AS-18 (pegmatite rim) and AS-19 (pegmatite core) are representative of the type-(I) pegmatites in the MRC. These zircons are by far the largest of all rock units within the MRC, ranging between 250 to >500µm. The zircons make up about 40% of thin section AS-19 (Fig 2.27). Secondary alteration is not characteristic of these zircons. Optically, these zircons display as clear to brown in PPL and as bright second order colors in XPL (Fig. 2.28). Depending on the zone, second order colors are difficult to observe due to a “spongy” appearance. All zircons are euhedral and were one of the first minerals to crystallize.

Zoning is very evident, and is observed optically, through BSE (Fig. 2.29), and through CL imaging (Fig. 2.30). Zircons from type-(I) pegmatites display a clear core, a dark zoned interior (metamict), and a clear, but fractured rim. The dark interior metamict zone is generally inclusion-rich (Th/U/Nb-rich Fe-oxides, quartz, fluorite, potassium feldspar, columbite, barite and REE-bearing minerals rich in Y such as xenotime). Additionally, EDS spot analyses identified Fe enrichment throughout the metamict zone in all zircons. The core and outer rim are overall inclusion free.

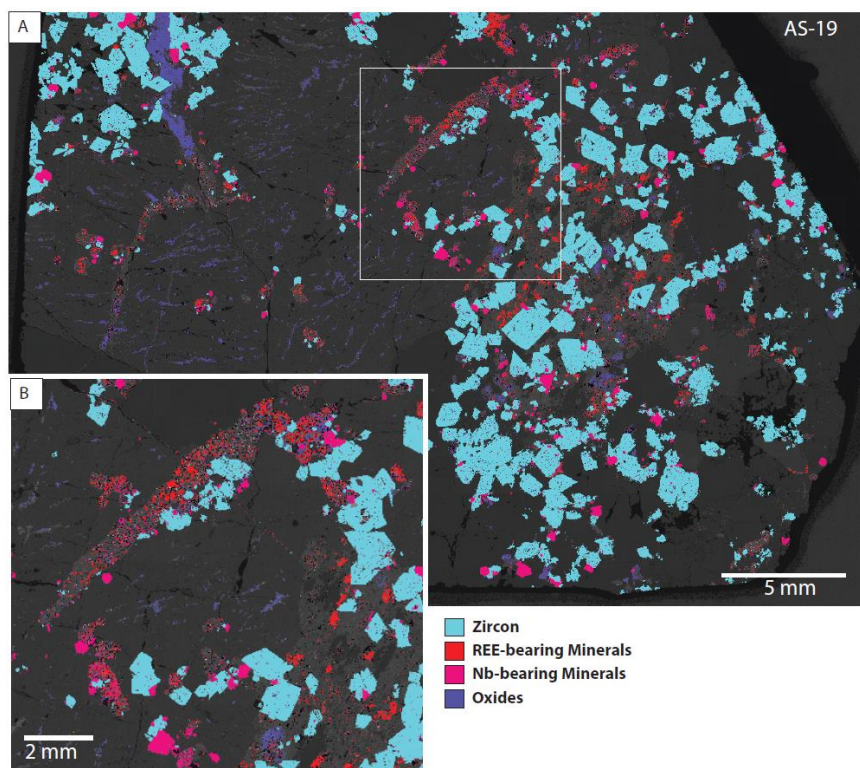


Figure 2.27: Bright phase scan of a type-(I) pegmatite, represented by thin section AS-19. REE-bearing minerals are red (parasite, allanite, and bastnasite) with pink Nb-bearing minerals (columbite). (A) Overview scan of thin section AS-19, (B) close-up image REE concentration in late stage vein network

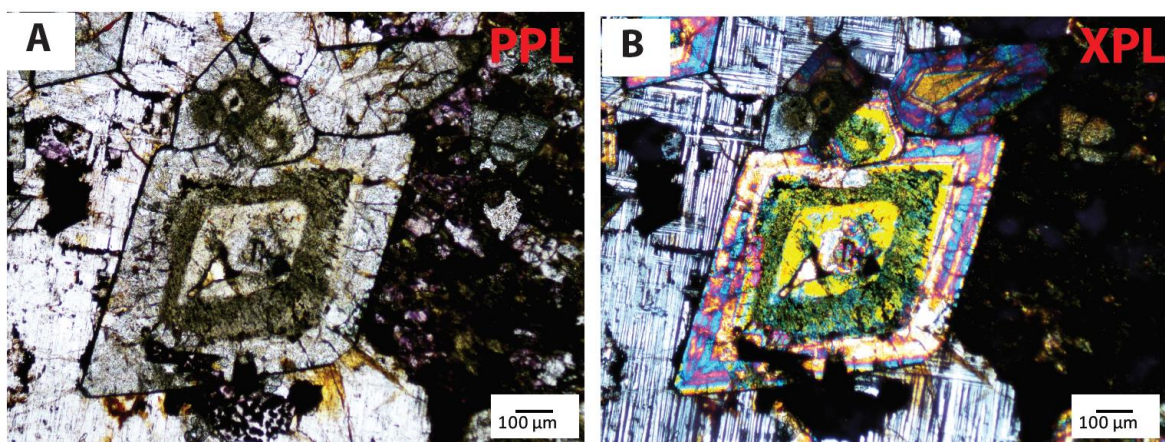


Figure 2.28: Type-(I) pegmatite zircon viewed in plane polarized light (A) and cross polarized light (B).

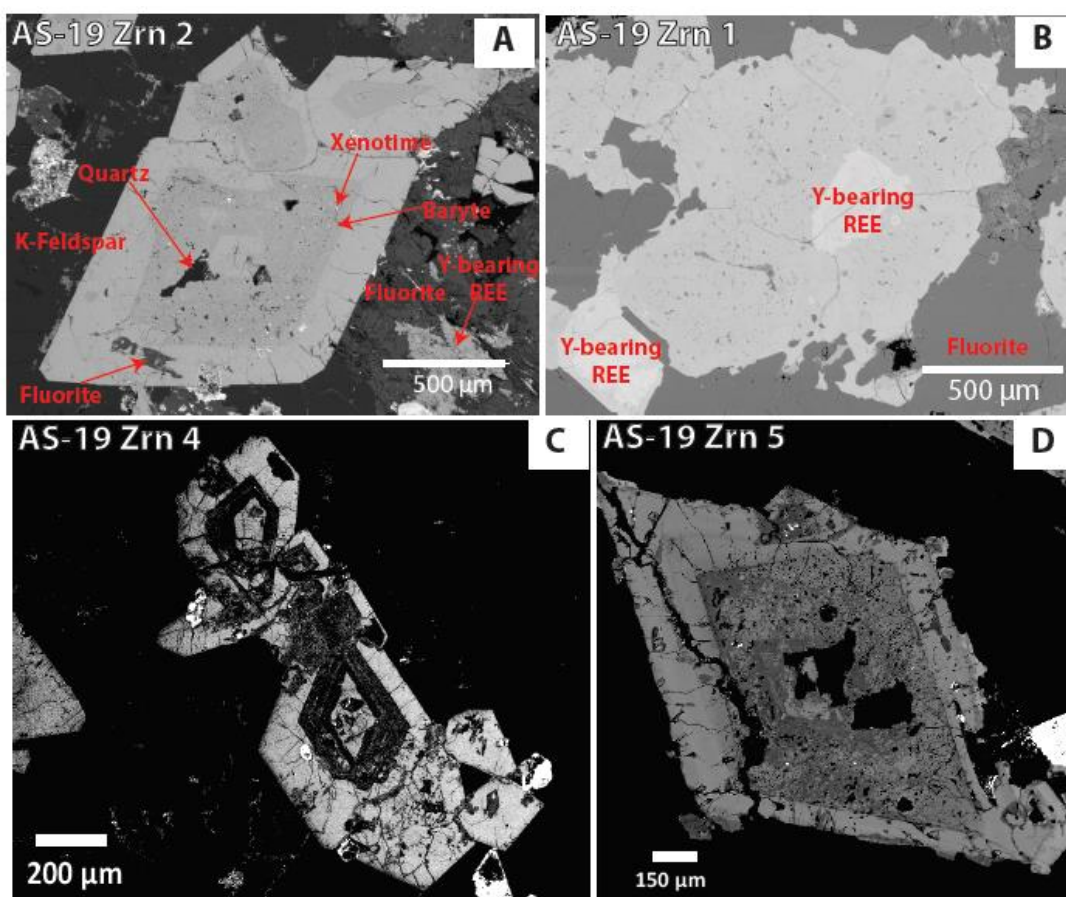


Figure 2.29: BSE images of type-(I) pegmatite zircon. (A) Inclusion rich metamict interior producing radial fractures into the rim, (B) inclusion rich zircon surrounding a Y-bearing REE mineral, (C) concentric zoned zircon with fractured rims, (D) zircon lacking a core with a metamict interior and fractured rims.

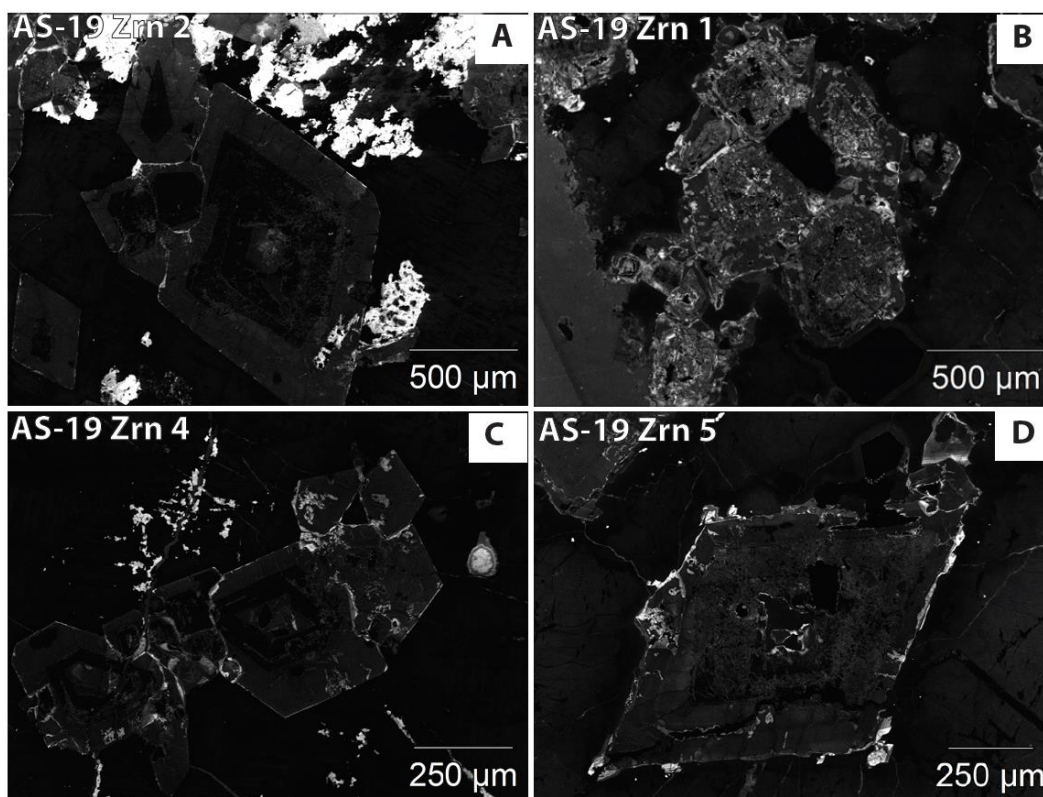


Figure 2.30: CL images of the same type-(I) pegmatite zircons viewed in Fig. 2.29. (A) Lack of CL reactivity, especially in the metamict zone, (B) fairly reactive zircon in the areas rich in inclusions, (C) lack of CL reactivity throughout zircon, (D) very small reactive rim in an otherwise unreactive zircon.

Type-(II) Pegmatites

Thin sections AS-MR38-01 through AS-MR38-10 were collected as transect samples in 25 cm increments across a type-(II) pegmatite hosted within MRG. All 10 thin sections were analyzed in detail in order to detect changes in zircon morphology across the body of the pegmatite. Samples AS-MR38-01, AS-MR38-02, and AS-MR38-10 are thin sections representing the rim of the pegmatite (wallrock). Samples AS-MR38-03, AS-MR38-04, AS-MR38-08, and AS-MR38-09 represent the interior of the pegmatite. Samples AS-MR38-05, AS-MR38-06, and AS-MR38-07 represent the core of the pegmatite.

Type-(II) pegmatite zircons can be divided into a coarser grained hydrothermally overprinted magmatic zircon, which is confined to the rim and very rarely observed in the interior of the pegmatite but never the core, and a finer grained, vein forming group of zircons that dominate the interior and core of the pegmatite. The coarser grained (magmatic) zircons display little to no zoning when viewed using BSE (Fig. 2.31) and CL imaging (Fig. 2.32). Rarely, small areas of zoning will present as discontinuous and

patchy. Additionally, inclusions are not present. Oftentimes, these zircons are surrounded by inclusion-free quartz. The far more abundant small hydrothermal zircons are very small and cluster together to form complex veinlets hosted in quartz and fluorite. Optically, the zircons can not be distinguished individually, but in clusters they display a green/brown weathered color and spongy texture (Fig. 2.33). Hydrothermal zircons can display no zoning to perfect concentric zoning when imaged using BSE (Fig. 2.34), however most zircons of this type are unreactive to CL imaging (Fig. 2.35). These zircons do not host any inclusions.

Nb-bearing minerals occur near the rim of the pegmatite and as smaller grains near the interior and core of the pegmatite. These tend to concentrate in vein networks with the zircons and oftentimes are associated with Fe-oxides throughout the thin section. Columbite crystallized early in the crystallization sequence at the pegmatite rim and crystallized later in the sequence closer to the core of the pegmatite, typically co-crystallizing with the zircons in this pegmatite.

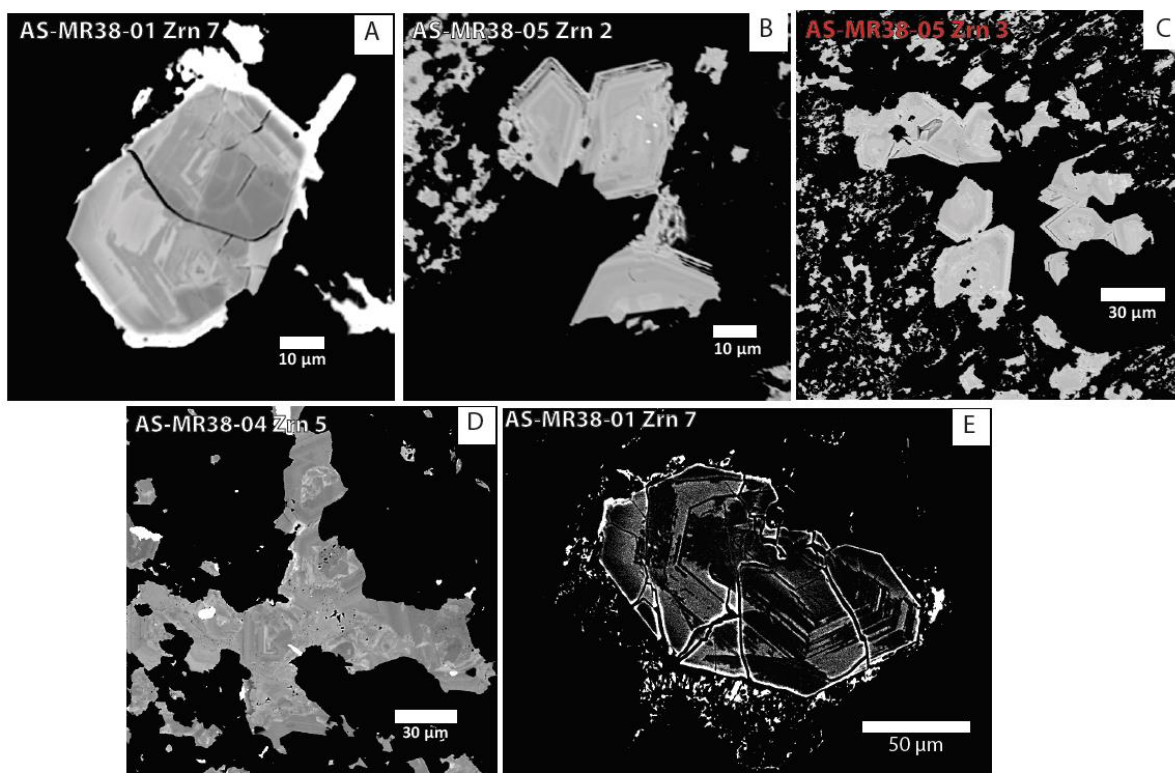


Figure 2.31: BSE images of larger magmatic wallrock zircons found in type-(II) pegmatites. (A) Patchy zoned zircon with a hydrothermal rim, (B) concentric zoned zircon with resorbed borders, (C) concentric zoned zircons within inclusion-free quartz, (D) cluster of patchy zoned zircons, (E) patchy zoned, fractured zircon.

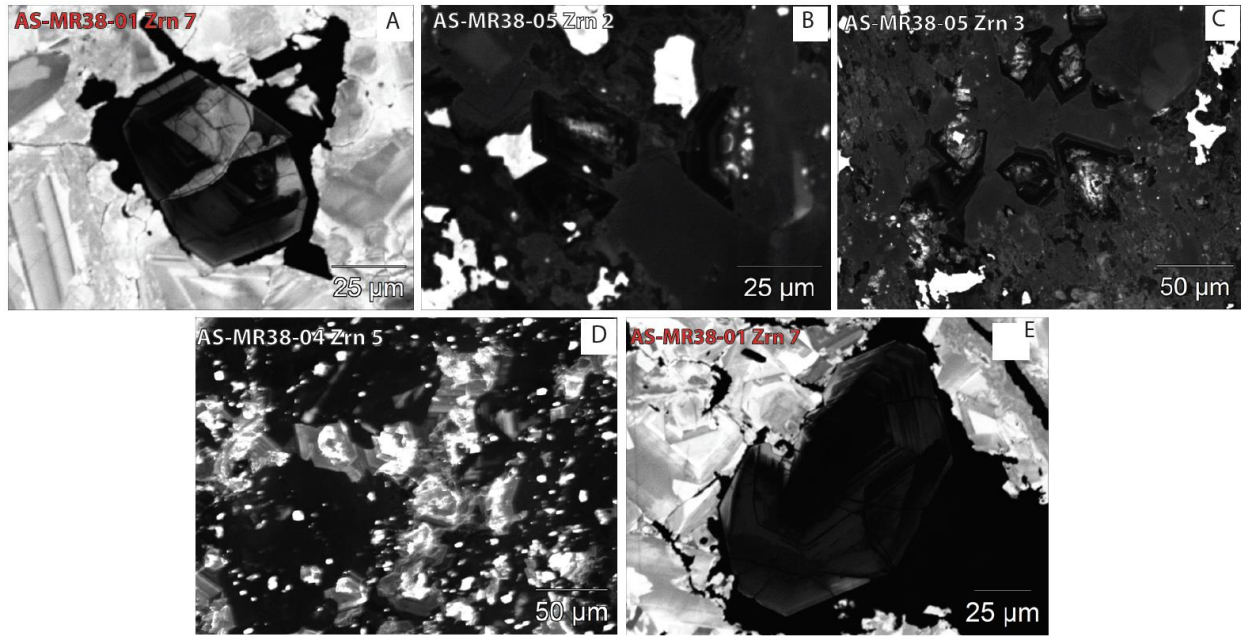


Figure 2.32: CL images of the same wallrock zircons found in the type-(II) pegmatite as Fig. 2.31. (A) Patchy reactive zircon in highly reactive fluorite, (B) mostly unreactive zircons, (C) reactive zircon cores with unreactive rims, (D) patchy reactivity in zircon cluster, (E) unreactive zircon.

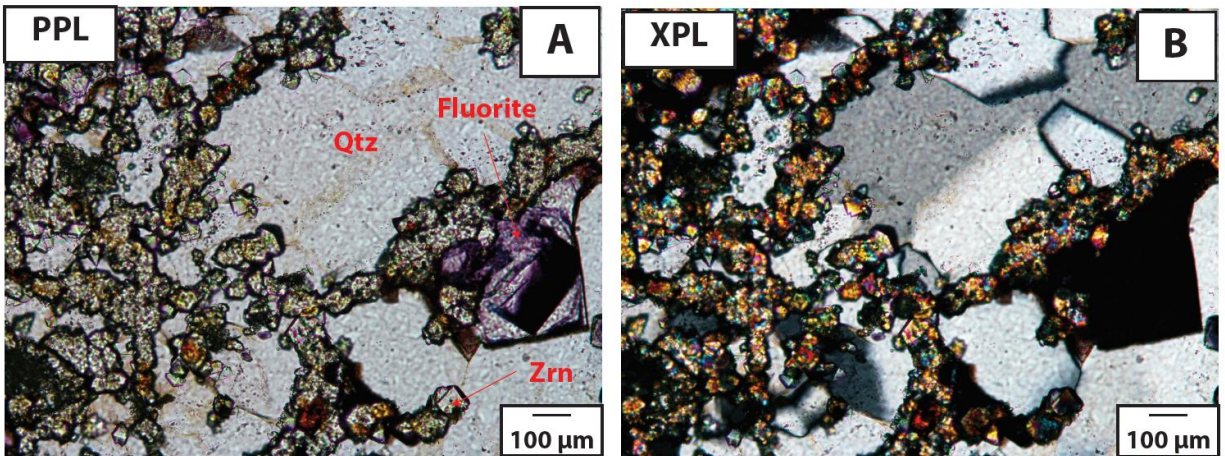


Figure 2.33: Type-(II) pegmatite fine grained zircons viewed in plane polarized light (A) and cross polarized light (B).

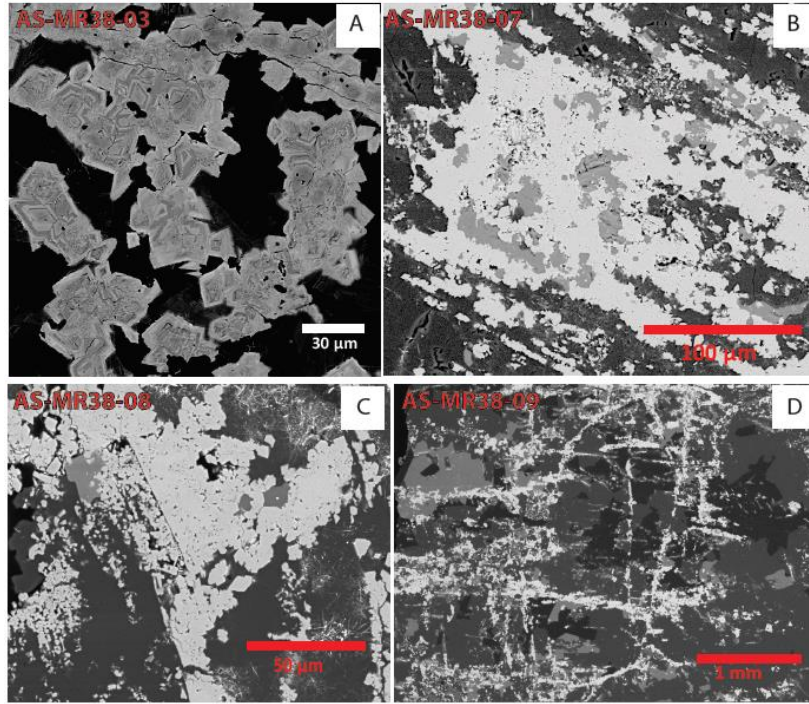


Figure 2.34: BSE images of hydrothermal zircons found in type-(II) pegmatites. (A) Concentric zoned small zircons, (B) thick zircon veinlet clusters hosted in quartz (dark gray) and fluorite (light gray), (C) hydrothermal zircons outlining relict minerals, (D) very thin hydrothermal zircon veinlets.

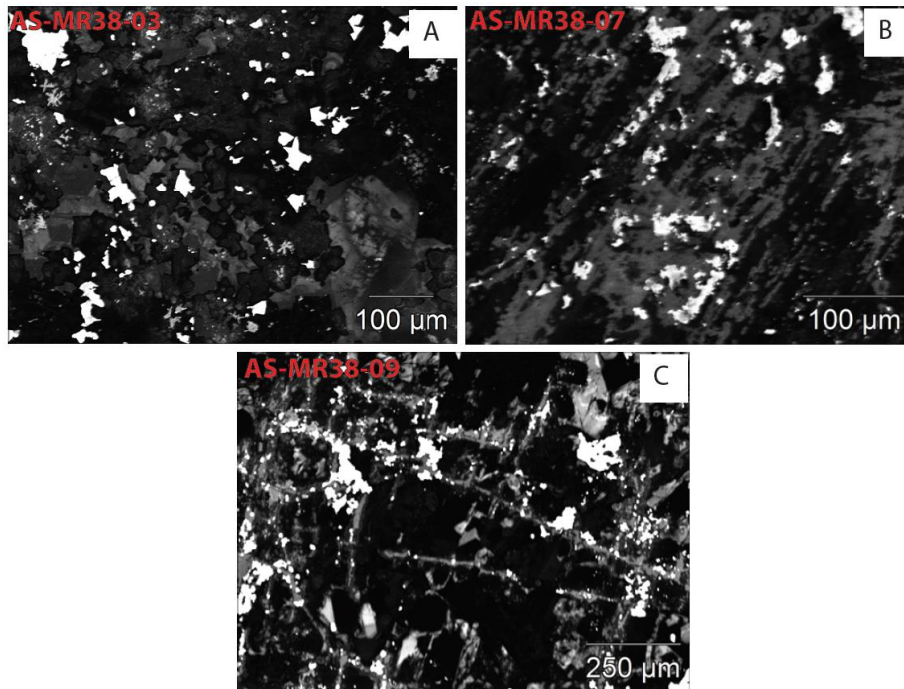


Figure 2.35: CL images of the same hydrothermal zircons seen in Fig. 2.34 found in type-(II) pegmatites. (A) Unreactive zircon clusters, (B) partially reactive zircon veinlets, (C) partially reactive zircon veinlets.

2.5.2 Mineral Chemistry

EMPA Major and Minor Element Chemistry of Zircon

Zircon occurs throughout all rock types of the MRC. A representative subset of 16 thin sections were chosen for analysis (Table 2.2). Roughly 4-6 zircon grains with 5-6 analysis points were chosen per thin section in order to reflect all textural varieties. Table 2.3 displays representative EMPA analyses for each rock type and zircon variety. Data distribution for analyzed elements is displayed in Fig. 2.36. Stoichiometrically, zircon (ZrSiO_4) is composed of 43.14 wt% Zr and 14.76 wt% Si (Hoskin and Schaltegger, 2003).

Pikes Peak Granite zircons range between 13.86 and 15.35 wt% for Si values and between 41.97 and 48.83 wt% for Zr. REE values range between 2,200 ppm to 27,000 ppm (Fig. 2.36H). Additional elements incorporated into the zircons include Ca (up to 6,100 ppm; Fig. 2.36C), Fe (up to 1.4 wt%; Fig. 2.36D), and Hf (up to 3.1 wt%; Fig. 2.36J). Elevated concentrations of Al (up to 1,300 ppm; Fig. 2.36A), Mg (up to 400 ppm; Fig. 2.36B), and Mn (up to 800 ppm; Fig. 2.36E) in isolated zones.

Fayalite -bearing quartz syenite zircons range between 13.64 and 15.46 wt% for Si values and between 41.96 and 49.02 wt% Zr. REE values range between 1,800 and 13,400 ppm (Fig. 2.36H). Additional elements incorporated into the zircons include Ca (up to 7,000 ppm; Fig. 2.36C), Fe (up to 15,200 ppm Fig. 2.36D), and Hf (up to 6 wt% Fig. 2.36J). In isolated zones, Fe, Ca, U, and Hf have a large spread in concentration (Figs 2.36C, D, F, and J).

Granitic dike zircons range between 14.93 and 14.96 wt% for Si values and between 46.97 and 47.14 wt% Zr. REE values range between 5,400 and 6,300 ppm (Fig. 2.36H). Additional elements incorporated into the zircons include Ca (up to 1,100 ppm; Fig. 2.36C), Fe (up to 2,800 ppm; Fig. 2.36D), and Hf (up to 1.4 wt%; Fig. 2.36J).

Mount Rosa Granite zircons range between 13.38 wt% for Si values and between 15.38 wt% Zr. REE values range between 1,600 up to 14,900 ppm (Fig. 2.36H). Additional elements incorporated into the zircons include Ca (up to 100 ppm in sieve zircons and 500 ppm in patchy zircons; Fig. 2.36C), Fe (up to 500 ppm in sieve zircons and 13,700 ppm for patchy zircons; Fig 37D), and Hf (up to 1.4 wt% for sieve zircons and 2.3 wt% for patchy zircons; Fig. 2.36J). Elevated concentrations of Al (up to 900 ppm for sieve zircons and 5,600 ppm for patchy zircons; Fig. 2.36A), Mg (below detection limit for sieve zircons but up to 900 ppm for patchy zircons; Fig. 2.36B), and Mn (below detection limit for sieve zircons but up to 7,200

ppm for patchy zircons; Fig. 2.36E) are specifically notable in the patchy MRG zircons. These elevated concentrations are isolated to the metamict zones, while the unaltered sieve MRG zircons and the crystalline zones of the patchy zircons usually are below the detecting limit. Both types of zircons display a moderate enrichment in P, REE, Hf, and Al compared to older units, but are lower in concentrations relative to younger units. Sieve zircons usually display lower concentrations in all elements analyzed (but enriched relative to older units) compared to patchy MRG zircons (Figs. 2.36A-K).

Mafic dike zircons range between 12.77 and 15.31 wt% for Si values and between 37.89 and 48.74 wt% Zr. REE values range between 4,500 and up to 67,000 ppm (Fig. 2.36H). Additional elements incorporated into the zircons include Ca (up to 8,500 ppm; Fig. 2.36C), Fe (up to 2.10 wt%; Fig. 2.36D), and Hf (up to 1.50 wt%; Fig. 2.36J). Overall, the concentrations of REE and HFSE elements increase dramatically beginning with the mafic dike zircons and continue to increase in concentration in the younger units.

Type-(I) pegmatite zircons range between 12.96 and 15.39 wt% for Si values and between 39.62 and 49.12 wt% Zr. REE values range between 2,100 and 42,000 ppm (Fig. 2.36H). Additional elements incorporated into the zircons include Ca (up to 6,600 ppm; Fig. 2.36C), Fe (up to 1.3 wt%; Fig. 2.36D), and Hf (up to 9,800 ppm; Fig. 2.36J). Elevated concentrations of Al (up to 1,300 ppm; Fig. 2.36A), Mg (up to 400 ppm; Fig. 2.36B), and Mn (up to 3,800 ppm; Fig. 2.36E) are isolated to the metamict zones relative to the healthy zones, which display little to no enrichment. Sn is elevated to 2,400 ppm in the type-(I) pegmatite (Fig. 2.36I).

Type-(II) pegmatite zircons range between 12.15 and 15.42 wt% for Si values and between 34.80 and 48.14 wt% Zr. REE values range between 1,000 ppm up to 85,200 ppm (Fig. 2.36H). Additional elements incorporated into the zircons include Ca (up to 9,400 ppm; Fig. 2.36C), Fe (up to 3.1 wt%; Fig. 2.36D), and Hf (up to 4.6 wt%; Fig. 2.36J). Type-(II) pegmatites display an extreme enrichment in Sn compared to all other units (up to 1.9 wt%; Fig. 2.36I). These zircons typically have low EMPA totals (between 88 and 100%) with Si values as low as 12.15 wt% and Zr values as low as 15.42 wt%.

Elements such as Mg, Al, U, Ca, Fe, and Mn tend to have a large spread in concentration among all zircons, without strong trends between rock units (Fig. 2.36A-F). However, elevated concentrations correlate to the spots with elevated REE concentrations and can mainly be found in metamict zones. Table 2.4 displays common concentrations of these elements solely within the metamict zones of the zircon. This pattern is largely evident in Fe, Y, Hf, and P element maps collected from a zircon in the PPG, MRG, and type-(I) pegmatite (Fig. 2.37). Additionally, the metamict zones are correlative to lower totals

collected by the EMPA (sometimes as low as 88%). This pattern is observed in all rock units containing metamict zones (PPG, MRG, and type-(I) pegmatites)

A negative correlation between 4+ valence state elements (Hf, Sn, U, and Th) and Zr is observed throughout the rock units with the exception of the mafic dike, consistent with simple substitution mechanisms (Fig. 2.38A). Although not as tight of a correlation, a positive correlation is observed between Fe and Al concentrations, commonly in the latter rock units (Fig. 2.38B).

2.5.3 Raman Spectroscopy

Raman spectroscopy was conducted within individual zones of select zircons after EMPA analysis. This technique was used to determine if specific zones contained water unable to be detected using EMPA. Additionally, Raman spectroscopy provided spectra to illustrate the degree of crystallinity each zircon exhibits, and if zones had become fully metamict. Three distinct spectra were produced based on the zircon type and zone (Fig. 2.39). Points were picked among zircons analyzed using EMPA and points were chosen close to the EMPA analysis points for comparison. Focus was placed on different zones in zircon crystals to understand the degree of crystallinity and/or metamictization.

The first spectrum (Fig. 2.39A) is representative of crystalline magmatic zircons throughout the rock units with little to no alteration. These zircons display relatively narrow ν_1 peaks at the 1000 cm^{-1} location, typically truncating between the 900 and 1050 cm^{-1} mark. Most zircons in this category also display a smaller, narrow ν_3 peak between the 950 and 975 cm^{-1} range, a pattern typically observed in crystalline zircons.

Within the more crystalline zircon zones, less crystalline zones can be present and were analyzed across all rock units with zircons containing these zones (Pikes Peak granite, Mount Rosa granite (patchy zircons) and type-(I) pegmatites). These zones display much broader ν_1 peaks at the 1000 cm^{-1} location (Fig. 2.39B). Generally, these spectra never display a second, narrow peak (ν_3), which is a characteristic of the more crystalline zones.

Hydrothermal zircons exclusive to the type-(II) pegmatites display a similar zircon spectrum to the healthy zones, but with the narrowest and most discrete peaks (Fig. 2.39C). The ν_1 peak's midpoint shifts to around 1010 in these zircons, generally beginning around 990 cm^{-1} and ending around 1025 cm^{-1} . The second ν_3 peak is the most discrete of all zircon types, also displaying as very narrow and sharp. The hydrothermal zircon spectrum displays as the most discrete, and therefore most crystalline of all zircons analyzed.

Table 2.3: Representative EMPA compositions of zircons from individual rock units within the MRC.

Sample	Pikes Peak Granite						Fayalite-bearing Quartz Syenite					
	PP-MR01 Zrn 1	PP-MR01 Zrn 4	PP-MR01 Zrn 5	Mean	Min	Max	PP-MR31 Zrn 2	PP-MR31 Zrn 6	PP-MR31 Zrn 8	Mean	Min	Max
Wt%O												
SiO ₂	32.18	32.22	32.59	31.80	29.66	32.84	32.67	32.91	32.91	32.40	29.17	33.07
ZrO ₂	63.55	64.09	65.48	62.94	56.69	65.95	64.53	65.78	64.42	64.07	56.67	66.21
Al ₂ O ₃	bdl	bdl	0.01	0.02	bdl	0.25	bdl	bdl	bdl	0.00	bdl	0.05
MgO	bdl	bdl	0.01	0.01	bdl	0.07	bdl	bdl	bdl	0.00	bdl	0.02
ThO ₂	0.08	0.04	0.04	0.12	0.04	1.01	0.09	0.05	bdl	0.04	bdl	0.14
UO ₂	0.11	0.03	0.04	0.15	0.03	0.76	0.08	0.03	0.05	0.09	0.03	0.55
SnO ₂	bdl	bdl	0.02	bdl	bdl	0.02	bdl	bdl	bdl	bdl	bdl	0.02
CaO	bdl	0.01	0.06	0.15	bdl	0.85	0.03	bdl	0.04	0.05	bdl	1.05
HfO ₂	1.75	1.29	1.62	1.58	1.15	3.65	1.20	1.70	1.74	1.97	1.20	7.45
Yb ₂ O ₃	0.11	0.09	0.07	0.16	0.05	0.58	0.19	0.13	0.12	0.16	0.06	0.41
Er ₂ O ₃	0.04	0.06	0.05	0.09	0.03	0.30	0.08	0.05	0.05	0.06	0.03	0.14
Gd ₂ O ₃	bdl	bdl	bdl	0.00	bdl	0.08	bdl	bdl	bdl	0.01	bdl	0.09
Dy ₂ O ₃	0.03	0.04	0.03	0.08	0.02	0.32	0.07	bdl	0.03	0.05	bdl	0.38
FeO	bdl	bdl	0.15	0.33	0.01	1.81	0.08	0.14	0.05	0.21	0.03	1.95
Sm ₂ O ₃	bdl	bdl	bdl	bdl	bdl	bdl	bdl	bdl	bdl	bdl	bdl	0.00
MnO	bdl	bdl	bdl	0.13	bdl	1.02	bdl	0.01	bdl	0.06	bdl	1.22
Pr ₂ O ₃	bdl	bdl	0.06	0.00	bdl	0.06	bdl	bdl	bdl	bdl	bdl	0.04
Nd ₂ O ₃	bdl	bdl	bdl	bdl	0.00	0.00	bdl	bdl	bdl	bdl	bdl	bdl
Ce ₂ O ₃	bdl	bdl	bdl	bdl	bdl	0.03	bdl	0.02	bdl	0.00	0.02	0.02
Y ₂ O ₃	0.34	0.40	0.23	0.51	0.14	2.11	0.56	0.25	0.17	0.34	bdl	0.84
P ₂ O ₅	bdl	bdl	bdl	0.02	bdl	0.15	bdl	bdl	bdl	0.00	0.03	0.03
TOTAL	98.07	98.18	100.42	98.07	94.32	100.74	99.43	100.91	99.41	99.36	94.45	101.03
Wt %												
Si	15.00	15.06	15.23	14.86	13.86	15.35	15.27	15.38	15.38	15.15	13.64	15.46
Zr	47.42	47.45	48.47	46.59	41.97	48.83	47.77	48.70	47.69	47.43	41.96	49.02
Al	bdl	bdl	0.00	0.05	bdl	0.13	bdl	bdl	bdl	0.03	bdl	0.03
Mg	bdl	bdl	0.00	0.02	bdl	0.04	bdl	bdl	bdl	0.01	bdl	0.01
Th	bdl	0.03	0.04	0.13	0.03	0.88	0.08	0.05	bdl	0.06	bdl	0.13
U	0.10	0.03	0.03	0.15	0.03	0.67	0.07	0.03	0.04	0.10	0.03	0.49
Sn	bdl	bdl	0.01	0.01	bdl	0.02	bdl	bdl	bdl	0.01	bdl	0.01
Ca	bdl	0.01	0.04	0.19	bdl	0.61	0.02	bdl	0.03	0.08	bdl	0.75
Hf	1.45	1.10	1.37	1.34	0.97	3.10	1.02	1.45	1.48	1.67	1.02	6.32
Fe	bdl	bdl	0.12	0.38	0.01	1.41	0.06	0.11	0.04	0.16	0.02	1.52
Mn	bdl	bdl	bdl	0.32	0.01	0.79	bdl	0.01	bdl	0.17	0.01	0.94
P	bdl	bdl	bdl	0.05	bdl	0.06	bdl	bdl	bdl	0.01	bdl	0.01
ΣREE + Y	0.37	0.48	0.36	0.82	0.20	2.86	0.74	0.38	0.31	0.62	0.17	1.59
TOTAL	98.33	98.18	100.42	98.07	94.32	100.74	99.43	100.91	99.41	99.36	94.45	101.03
a.p.f.u.												
Si	1.01	1.01	1.00	--	--	--	1.01	1.00	1.01	--	--	--
Zr	0.97	0.98	0.98	--	--	--	0.97	0.98	0.97	--	--	--
Al	0.00	0.00	0.00	--	--	--	0.00	0.00	0.00	--	--	--
Mg	0.00	0.00	0.00	--	--	--	0.00	0.00	0.00	--	--	--
Th	0.00	0.00	0.00	--	--	--	0.00	0.00	0.00	--	--	--
U	0.00	0.00	0.00	--	--	--	0.00	0.00	0.00	--	--	--
Sn	0.00	0.00	0.00	--	--	--	0.00	0.00	0.00	--	--	--
Ca	0.00	0.00	0.00	--	--	--	0.00	0.00	0.00	--	--	--
Hf	0.02	0.01	0.01	--	--	--	0.01	0.01	0.02	--	--	--
Fe	0.00	0.00	0.00	--	--	--	0.00	0.00	0.00	--	--	--
Mn	0.00	0.00	0.00	--	--	--	0.00	0.00	0.00	--	--	--
P	0.00	0.00	0.00	--	--	--	0.00	0.00	0.00	--	--	--
ΣREE + Y	0.01	0.01	0.01	--	--	--	0.01	0.01	0.00	--	--	--
TOTAL	2.00	2.00	2.00	--	--	--	2.00	2.00	2.00	--	--	--

bdl: Below detection limit

Table 2.3 continued:

Sample	Granitic Dike					Mount Rosa Granite Patchy Zircon					
	PP-MR30 Zrn 1	PP-MR30 Zrn 1	Mean	Min	Max	PP-MR2016-13 Zrn 6	PP-MR25 Zrn 3	PP-MR25 Zrn 5	Mean	Min	Max
Wt%O											
SiO ₂	32.02	31.95	31.98	31.95	32.02	32.25	31.93	32.16	32.12	31.85	32.57
ZrO ₂	63.68	63.45	63.57	63.45	63.68	64.18	63.42	64.17	64.04	62.92	67.04
Al ₂ O ₃	bdl	bdl	bdl	bdl	bdl	0.18	bdl	bdl	0.03	bdl	0.18
MgO	bdl	bdl	bdl	bdl	bdl	bdl	bdl	bdl	bdl	bdl	bdl
ThO ₂	0.05	0.07	0.06	0.05	0.07	bdl	0.05	0.04	0.01	0.04	0.05
UO ₂	bdl	bdl	bdl	bdl	bdl	0.24	0.12	0.07	0.10	0.07	0.24
SnO ₂	bdl	bdl	bdl	bdl	bdl	bdl	bdl	bdl	bdl	bdl	bdl
CaO	0.10	0.16	0.13	0.10	0.16	0.01	bdl	0.01	0.00	bdl	0.01
HfO ₂	1.57	1.65	1.61	1.57	1.65	1.18	1.38	1.37	1.37	1.18	1.65
Yb ₂ O ₃	0.16	0.17	0.16	0.16	0.17	0.30	0.47	0.30	0.32	0.12	0.47
Er ₂ O ₃	0.06	0.08	0.07	0.06	0.08	0.07	0.21	0.12	0.13	0.07	0.21
Gd ₂ O ₃	bdl	bdl	bdl	bdl	bdl	bdl	0.05	bdl	0.01	bdl	0.05
Dy ₂ O ₃	0.07	0.09	0.08	0.07	0.09	bdl	0.12	0.09	0.08	bdl	0.14
FeO	0.26	0.37	0.32	0.26	0.37	0.06	0.01	bdl	0.02	0.01	0.06
Sm ₂ O ₃	bdl	bdl	bdl	bdl	bdl	bdl	bdl	bdl	bdl	bdl	bdl
MnO	0.10	0.18	0.14	0.10	0.18	bdl	bdl	bdl	bdl	bdl	bdl
Pr ₂ O ₃	bdl	bdl	bdl	bdl	bdl	bdl	bdl	bdl	bdl	bdl	bdl
Nd ₂ O ₃	bdl	bdl	bdl	bdl	bdl	bdl	bdl	bdl	bdl	bdl	bdl
Ce ₂ O ₃	bdl	bdl	bdl	bdl	bdl	bdl	bdl	bdl	bdl	bdl	bdl
Y ₂ O ₃	0.37	0.44	0.41	0.37	0.44	0.21	0.75	0.56	0.49	0.06	0.75
P ₂ O ₅	bdl	bdl	bdl	bdl	bdl	0.12	0.23	0.08	0.13	0.08	0.23
TOTAL	98.53	98.67	98.60	98.53	98.67	98.69	98.63	98.88	98.73	97.78	101.28
Wt %											
Si	14.96	14.93	14.95	14.93	14.96	15.07	14.93	15.03	15.01	14.89	15.22
Zr	47.14	46.97	47.06	46.97	47.14	47.52	46.95	47.51	47.41	46.58	49.63
Al	bdl	bdl	bdl	bdl	bdl	0.09	0.09	0.09	0.09	0.09	0.09
Mg	bdl	bdl	bdl	bdl	bdl	bdl	bdl	bdl	bdl	bdl	bdl
Th	0.05	0.06	0.05	0.05	0.06	bdl	0.04	bdl	0.04	0.04	0.04
U	bdl	bdl	bdl	bdl	bdl	0.21	0.11	0.06	0.11	0.06	0.21
Sn	bdl	bdl	bdl	bdl	bdl	bdl	bdl	bdl	bdl	bdl	bdl
Ca	0.07	0.11	0.09	0.07	0.11	0.01	bdl	0.01	0.01	0.01	0.01
Hf	1.33	1.40	1.36	1.33	1.40	1.00	1.17	1.16	1.16	1.00	1.40
Fe	0.21	0.28	0.24	0.21	0.28	0.05	0.01	bdl	0.03	0.01	0.05
Mn	0.08	0.14	0.11	0.08	0.14	bdl	bdl	bdl	bdl	bdl	bdl
P	bdl	bdl	bdl	bdl	bdl	0.05	0.10	0.04	0.07	0.04	0.10
ΣREE + Y	0.54	0.63	0.59	0.54	0.63	0.49	1.35	0.89	0.93	0.32	1.36
TOTAL	98.53	98.67	98.60	98.53	98.67	98.69	98.63	98.88	98.73	97.78	101.28
a.p.f.u.											
Si	1.00	1.00	--	--	--	1.00	1.00	1.00	--	--	--
Zr	0.97	0.97	--	--	--	0.97	0.97	0.97	--	--	--
Al	0.00	0.00	--	--	--	0.01	0.00	0.00	--	--	--
Mg	0.00	0.00	--	--	--	0.00	0.00	0.00	--	--	--
Th	0.00	0.00	--	--	--	0.00	0.00	0.00	--	--	--
U	0.00	0.00	--	--	--	0.00	0.00	0.00	--	--	--
Sn	0.00	0.00	--	--	--	0.00	0.00	0.00	--	--	--
Ca	0.00	0.01	--	--	--	0.00	0.00	0.00	--	--	--
Hf	0.01	0.01	--	--	--	0.01	0.01	0.01	--	--	--
Fe	0.01	0.01	--	--	--	0.00	0.00	0.00	--	--	--
Mn	0.00	0.00	--	--	--	0.00	0.00	0.00	--	--	--
P	0.00	0.00	--	--	--	0.00	0.00	0.00	--	--	--
ΣREE + Y	0.01	0.01	--	--	--	0.01	0.02	0.01	--	--	--
TOTAL	2.01	2.01	--	--	--	2.00	2.00	2.00	--	--	--

bdl: Below detection limit

Table 2.3 continued:

Sample	Mount Rosa Granite Patchy Zircon						Mafic Dike					
	PP-MR2016-07 Zrn 1	PP-MR2016-07 Zrn 7	PP-MR2016-13 Zrn 4	Mean	Min	Max	PP-MR58 Zrn 2	PP-MR58 Zrn 3	PP-MR58 Zrn 5	Mean	Min	Max
Wt%O												
SiO ₂	32.47	32.35	32.73	31.96	28.63	32.91	32.55	31.75	32.13	30.79	27.31	32.76
ZrO ₂	65.61	64.05	64.80	63.56	56.31	66.89	64.46	60.49	64.59	59.10	49.83	65.84
Al ₂ O ₃	0.01	0.03	0.01	0.09	0.01	1.06	bdl	bdl	bdl	0.17	bdl	0.95
MgO	bdl	bdl	bdl	0.00	bdl	0.04	bdl	bdl	bdl	bdl	bdl	0.03
ThO ₂	0.06	0.11	bdl	0.06	0.04	0.29	bdl	bdl	bdl	bdl	bdl	bdl
UO ₂	bdl	0.10	bdl	0.18	bdl	0.82	bdl	bdl	bdl	bdl	bdl	bdl
SnO ₂	bdl	bdl	bdl	0.00	bdl	0.03	bdl	bdl	bdl	bdl	bdl	bdl
CaO	bdl	bdl	0.04	0.05	bdl	0.71	bdl	0.53	bdl	0.30	bdl	1.19
HfO ₂	1.41	1.47	1.55	1.61	1.08	2.75	1.73	1.00	1.81	1.27	0.85	1.81
Yb ₂ O ₃	0.03	0.15	0.22	0.17	0.03	0.49	0.18	0.28	0.20	0.28	0.13	0.54
Er ₂ O ₃	0.04	0.12	0.06	0.07	0.03	0.14	0.13	0.26	0.12	0.28	0.04	0.59
Gd ₂ O ₃	bdl	bdl	bdl	0.00	bdl	0.05	0.10	0.20	bdl	0.22	bdl	0.44
Dy ₂ O ₃	bdl	0.04	0.06	0.06	bdl	0.28	0.16	0.34	0.08	0.36	0.04	0.78
FeO	0.09	bdl	0.01	0.30	bdl	1.76	0.05	0.31	0.23	0.65	0.03	2.78
Sm ₂ O ₃	bdl	bdl	bdl	bdl	bdl	0.00	bdl	bdl	bdl	0.05	bdl	0.19
MnO	bdl	bdl	bdl	0.13	bdl	0.93	0.01	0.03	bdl	0.07	bdl	0.64
Pr ₂ O ₃	0.04	bdl	bdl	0.00	bdl	0.04	bdl	bdl	bdl	0.01	bdl	0.07
Nd ₂ O ₃	bdl	bdl	bdl	0.00	bdl	0.06	bdl	0.04	bdl	0.11	bdl	0.58
Ce ₂ O ₃	bdl	bdl	bdl	0.00	bdl	0.07	bdl	0.07	bdl	0.13	bdl	0.91
Y ₂ O ₃	0.13	0.64	0.40	0.37	0.07	0.97	1.09	3.02	0.72	2.89	0.33	5.48
P ₂ O ₅	bdl	bdl	bdl	0.01	bdl	0.32	bdl	bdl	bdl	bdl	bdl	bdl
TOTAL	99.84	98.95	99.88	98.62	94.05	101.82	98.62	95.27	98.11	93.37	88.64	98.77
Wt %												
Si	15.18	15.12	15.30	14.94	13.38	15.38	15.21	14.84	15.02	14.45	12.77	15.31
Zr	48.57	47.41	47.97	47.05	41.69	49.52	47.72	44.78	47.81	44.12	37.89	48.74
Al	0.01	0.02	0.01	0.06	bdl	0.56	bdl	bdl	bdl	0.12	bdl	0.50
Mg	bdl	bdl	bdl	0.02	0.01	0.03	bdl	bdl	bdl	0.01	0.01	0.02
Th	0.05	0.10	bdl	0.08	0.04	0.25	bdl	bdl	bdl	bdl	bdl	bdl
U	bdl	0.09	bdl	0.19	0.03	0.73	bdl	bdl	bdl	bdl	bdl	bdl
Sn	bdl	bdl	bdl	0.02	0.01	0.02	bdl	bdl	bdl	bdl	bdl	bdl
Ca	bdl	bdl	0.03	0.11	0.01	0.51	bdl	0.38	bdl	0.34	bdl	0.85
Hf	1.20	1.24	1.31	1.37	0.92	2.33	1.47	0.84	1.54	1.08	0.72	1.54
Fe	0.07	bdl	0.01	0.27	0.01	1.37	0.04	0.24	0.18	0.48	0.03	2.16
Mn	0.01	bdl	bdl	0.32	0.01	0.72	0.01	0.02	bdl	0.08	0.01	0.49
P	bdl	bdl	bdl	0.10	0.06	0.14	bdl	bdl	bdl	bdl	bdl	bdl
ΣREE + Y	0.20	0.77	0.61	0.78	0.31	1.75	1.37	3.40	0.91	3.62	0.45	7.79
TOTAL	99.84	98.95	99.88	98.62	94.05	101.82	98.62	95.27	98.11	93.37	88.64	98.77
a.p.f.u.												
Si	1.00	1.00	1.00	--	--	--	1.00	1.00	0.99	--	--	--
Zr	0.98	0.97	0.97	--	--	--	0.97	0.93	0.97	--	--	--
Al	0.00	0.00	0.01	--	--	--	0.00	0.00	0.00	--	--	--
Mg	0.00	0.00	0.00	--	--	--	0.00	0.00	0.00	--	--	--
Th	0.00	0.00	0.00	--	--	--	0.00	0.00	0.00	--	--	--
U	0.00	0.00	0.00	--	--	--	0.00	0.00	0.00	--	--	--
Sn	0.00	0.00	0.00	--	--	--	0.00	0.00	0.00	--	--	--
Ca	0.00	0.00	0.00	--	--	--	0.00	0.02	0.00	--	--	--
Hf	0.01	0.01	0.01	--	--	--	0.02	0.01	0.02	--	--	--
Fe	0.00	0.00	0.00	--	--	--	0.00	0.01	0.01	--	--	--
Mn	0.00	0.00	0.00	--	--	--	0.00	0.00	0.00	--	--	--
P	0.00	0.00	0.00	--	--	--	0.00	0.00	0.00	--	--	--
ΣREE + Y	0.00	0.01	0.01	--	--	--	0.02	0.06	0.02	--	--	--
TOTAL	2.00	2.00	2.00	--	--	--	2.01	2.03	2.01	--	--	--

bdl: Below detection limit

Table 2.3 continued:

Sample	Type I Pegmatite						Type II Pegmatite					
	AS-19 Zrn 2	AS-19 Zrn 3	AS-19 Zrn 5	Mean	Min	Max	AS-MR38-01 Zrn 2	AS-MR38-08 Zrn 4	AS-MR38-05 Zrn 4	Mean	Min	Max
Wt%O												
SiO ₂	32.23	32.18	32.28	31.11	27.73	32.93	32.40	30.96	30.38	30.44	25.98	32.99
ZrO ₂	64.46	63.64	64.20	61.93	53.52	66.36	63.99	58.22	58.28	57.70	47.01	65.03
Al ₂ O ₃	bdl	bdl	bdl	0.05	bdl	0.25	0.04	0.65	0.08	0.45	bdl	1.32
MgO	bdl	bdl	bdl	0.01	bdl	0.07	bdl	bdl	bdl	0.00	bdl	0.04
ThO ₂	0.10	0.13	0.13	0.16	0.00	0.53	bdl	0.09	0.06	0.61	bdl	6.68
UO ₂	0.10	0.08	0.08	0.15	bdl	0.31	0.04	bdl	bdl	0.00	bdl	0.13
SnO ₂	bdl	bdl	0.02	0.06	bdl	0.30	bdl	0.28	1.87	0.48	bdl	2.36
CaO	bdl	bdl	bdl	0.25	bdl	0.92	bdl	0.34	0.09	0.27	bdl	1.31
HfO ₂	1.06	1.04	0.92	0.95	0.80	1.15	2.31	3.83	4.59	3.11	0.86	5.48
Yb ₂ O ₃	0.48	0.60	0.41	0.49	0.07	0.99	0.27	0.85	0.26	0.70	0.05	1.92
Er ₂ O ₃	0.27	0.32	0.26	0.30	0.03	0.64	0.11	0.21	0.09	0.18	0.00	0.87
Gd ₂ O ₃	0.09	0.06	0.07	0.08	bdl	0.22	bdl	0.09	bdl	0.04	bdl	0.29
Dy ₂ O ₃	0.11	0.12	0.13	0.23	bdl	0.65	0.05	0.24	0.12	0.19	bdl	0.71
FeO	bdl	bdl	0.02	0.49	bdl	1.66	0.07	0.29	0.16	0.66	bdl	4.00
Sm ₂ O ₃	bdl	bdl	bdl	0.00	bdl	0.07	bdl	bdl	bdl	0.00	bdl	0.04
MnO	bdl	bdl	bdl	0.14	bdl	0.49	bdl	0.13	0.23	0.25	bdl	1.04
Pr ₂ O ₃	bdl	bdl	bdl	bdl	bdl	bdl	bdl	bdl	bdl	0.00	bdl	0.00
Nd ₂ O ₃	bdl	bdl	bdl	0.00	bdl	0.03	bdl	bdl	bdl	0.00	bdl	0.06
Ce ₂ O ₃	bdl	bdl	bdl	0.00	bdl	0.03	bdl	0.03	bdl	0.02	bdl	0.18
Y ₂ O ₃	0.73	0.86	0.87	1.12	0.10	2.82	0.27	1.24	0.48	0.99	bdl	4.73
P ₂ O ₅	0.22	0.12	0.13	0.18	bdl	0.44	bdl	0.17	0.05	0.12	bdl	1.15
TOTAL	99.74	99.08	99.48	97.68	91.63	100.66	99.57	97.59	96.55	96.12	88.36	100.49
Wt %												
Si	15.06	15.04	15.09	14.54	12.96	15.39	15.14	14.47	14.20	14.23	12.15	15.42
Zr	47.72	47.11	47.53	45.85	39.62	49.12	47.37	43.10	43.14	42.72	34.80	48.14
Al	bdl	bdl	bdl	0.07	bdl	0.13	0.02	0.34	0.04	0.32	bdl	0.70
Mg	bdl	bdl	bdl	0.02	bdl	0.04	bdl	bdl	bdl	0.01	bdl	0.02
Th	0.09	0.11	0.11	0.17	0.03	0.47	bdl	0.08	0.05	0.76	bdl	5.87
U	0.08	0.07	0.07	0.15	0.03	0.27	0.03	bdl	bdl	0.05	bdl	0.11
Sn	bdl	bdl	0.02	0.10	bdl	0.24	bdl	0.22	1.47	0.50	bdl	1.86
Ca	bdl	bdl	bdl	0.43	bdl	0.66	bdl	0.24	0.06	0.23	bdl	0.94
Hf	0.90	0.88	0.78	0.80	0.68	0.98	1.96	3.25	3.89	2.64	0.73	4.65
Fe	bdl	bdl	0.02	0.52	bdl	1.29	0.05	0.22	0.12	0.54	bdl	3.11
Mn	bdl	bdl	bdl	0.27	bdl	0.38	bdl	0.10	0.18	0.26	bdl	0.80
P	0.09	0.05	0.06	0.11	0.03	0.19	bdl	0.07	0.02	0.10	bdl	0.50
ΣREE + Y	1.40	1.64	1.45	1.97	0.22	4.52	0.58	2.22	0.78	1.97	0.06	7.28
TOTAL	99.74	99.08	99.48	97.68	91.63	100.66	99.57	97.59	96.55	96.12	88.36	100.49
a.p.f.u.												
Si	1.00	1.00	1.00	--	--	--	1.00	0.99	0.99	--	--	--
Zr	0.97	0.97	0.97	--	--	--	0.97	0.92	0.92	--	--	--
Al	0.00	0.00	0.00	--	--	--	0.00	0.02	0.00	--	--	--
Mg	0.00	0.00	0.00	--	--	--	0.00	0.00	0.00	--	--	--
Th	0.00	0.00	0.00	--	--	--	0.00	0.00	0.00	--	--	--
U	0.00	0.00	0.00	--	--	--	0.00	0.00	0.00	--	--	--
Sn	0.00	0.00	0.00	--	--	--	0.00	0.00	0.02	--	--	--
Ca	0.00	0.00	0.00	--	--	--	0.00	0.01	0.00	--	--	--
Hf	0.01	0.01	0.01	--	--	--	0.02	0.03	0.04	--	--	--
Fe	0.00	0.00	0.00	--	--	--	0.00	0.01	0.00	--	--	--
Mn	0.00	0.00	0.00	--	--	--	0.00	0.00	0.01	--	--	--
P	0.00	0.00	0.00	--	--	--	0.00	0.00	0.00	--	--	--
ΣREE + Y	0.02	0.02	0.02	--	--	--	0.01	0.04	0.01	--	--	--
TOTAL	2.00	2.01	2.01	--	--	--	2.00	2.03	2.01	--	--	--

bdl: Below detection limit

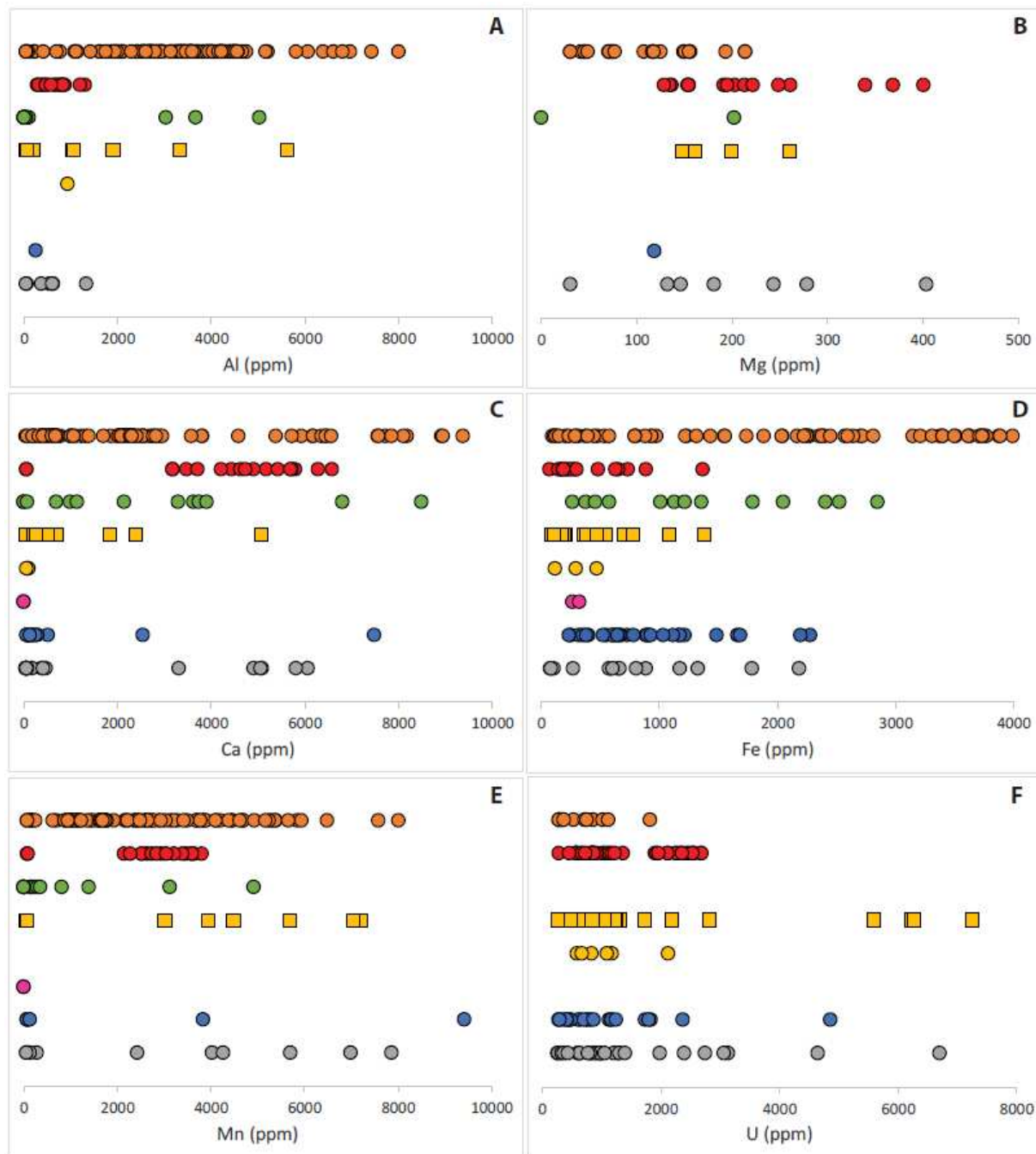


Figure 2.36: Compositional distributions of elemental data in zircons hosted within individual rock units throughout the MRC. (A) Al, (B) Mg, (C) Ca, (D) Fe, (E) Mn, (F) U

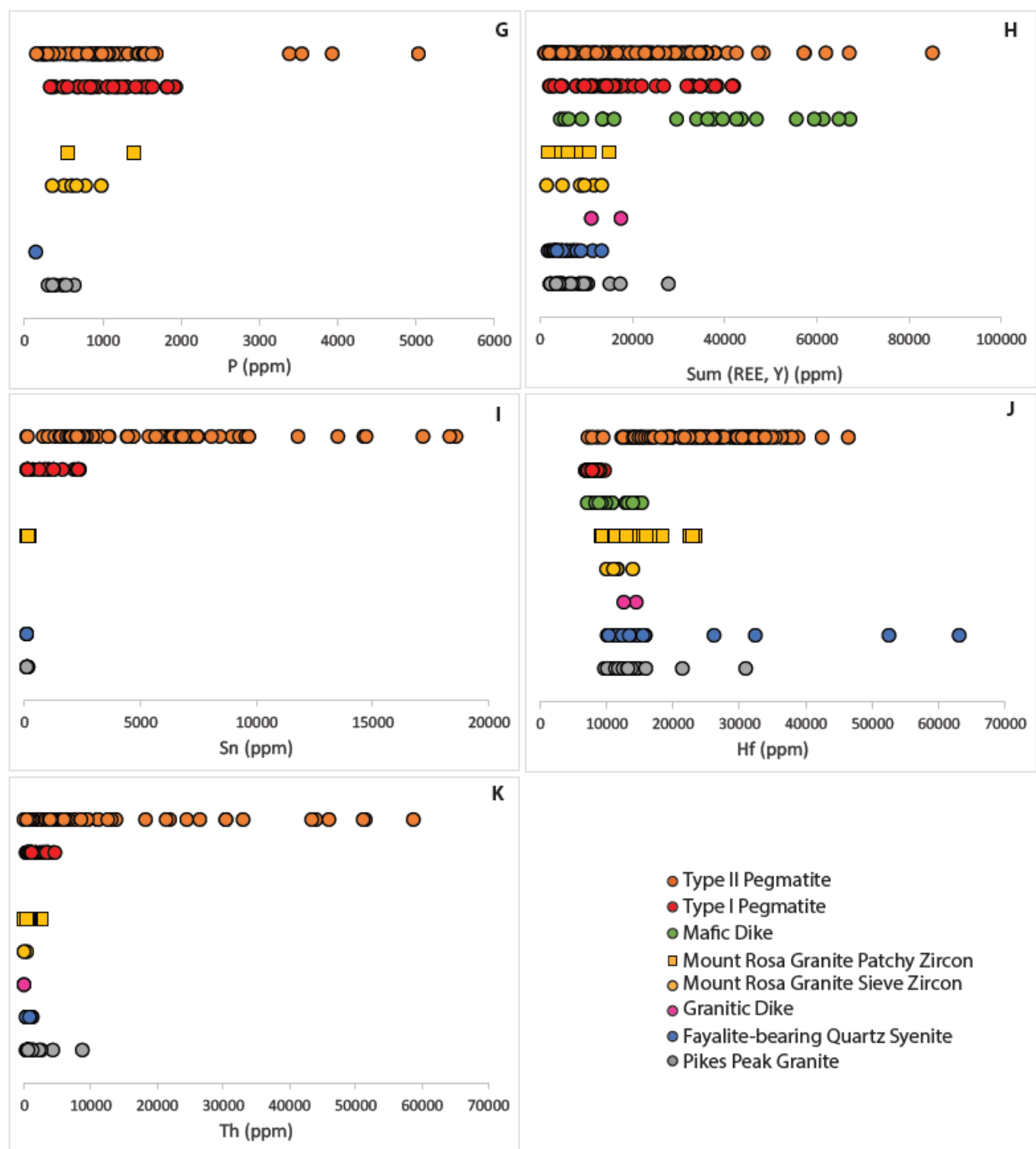


Figure 2.36 continued

Table 2.4: Representative EMPA concentrations of metamict zones within zircon grains independent to the PPG, MRG, and type (I) pegmatites

Sample	Pikes Peak Granite PP-MR01 Zrn 5	Mount Rosa Granite Zircon II PP-MR2016-07 Zrn 1	Type I Pegmatite AS-19 Zrn 3
Wt%O			
SiO ₂	29.87	30.85	28.80
ZrO ₂	59.16	61.68	56.65
Al ₂ O ₃	bdl	0.36	0.05
MgO	0.07	0.02	0.06
ThO ₂	0.25	0.12	0.20
UO ₂	0.36	0.64	0.28
SnO ₂	bdl	0.03	0.05
CaO	0.81	0.10	0.81
HfO ₂	1.43	1.46	0.84
Yb ₂ O ₃	0.22	0.13	0.69
Er ₂ O ₃	0.09	0.03	0.38
Gd ₂ O ₃	bdl	bdl	0.15
Dy ₂ O ₃	0.27	0.16	0.44
FeO	1.64	0.87	1.39
Sm ₂ O ₃	bdl	bdl	bdl
MnO	0.90	0.58	0.49
Pr ₂ O ₃	bdl	bdl	bdl
Nd ₂ O ₃	bdl	bdl	bdl
Ce ₂ O ₃	bdl	bdl	bdl
Y ₂ O ₃	0.63	0.28	1.37
P ₂ O ₅	bdl	bdl	0.42
TOTAL	95.58	97.19	93.07
Wt %			
Si	13.96	14.42	13.46
Zr	43.80	45.66	41.94
Al	bdl	0.19	0.03
Mg	0.04	0.01	0.03
Th	0.22	0.11	0.18
U	0.31	0.56	0.25
Sn	bdl	0.02	0.04
Ca	0.58	0.07	0.58
Hf	1.21	1.23	0.71
Fe	1.27	0.68	1.08
Mn	0.70	0.45	0.38
P	bdl	bdl	0.18
ΣREE + Y	1.00	0.51	2.53
TOTAL	95.58	97.19	93.07
a.p.f.u.			
Si	0.98	0.98	0.97
Zr	0.94	0.96	0.93
Al	0.00	0.01	0.00
Mg	0.00	0.00	0.00
Th	0.00	0.00	0.00
U	0.00	0.00	0.00
Sn	0.00	0.00	0.00
Ca	0.03	0.00	0.03
Hf	0.01	0.01	0.01
Fe	0.04	0.02	0.04
Mn	0.02	0.02	0.01
P	0.00	0.00	0.01
ΣREE + Y	0.02	0.01	0.04
TOTAL	2.05	2.03	2.05

bdl: Below detection limit

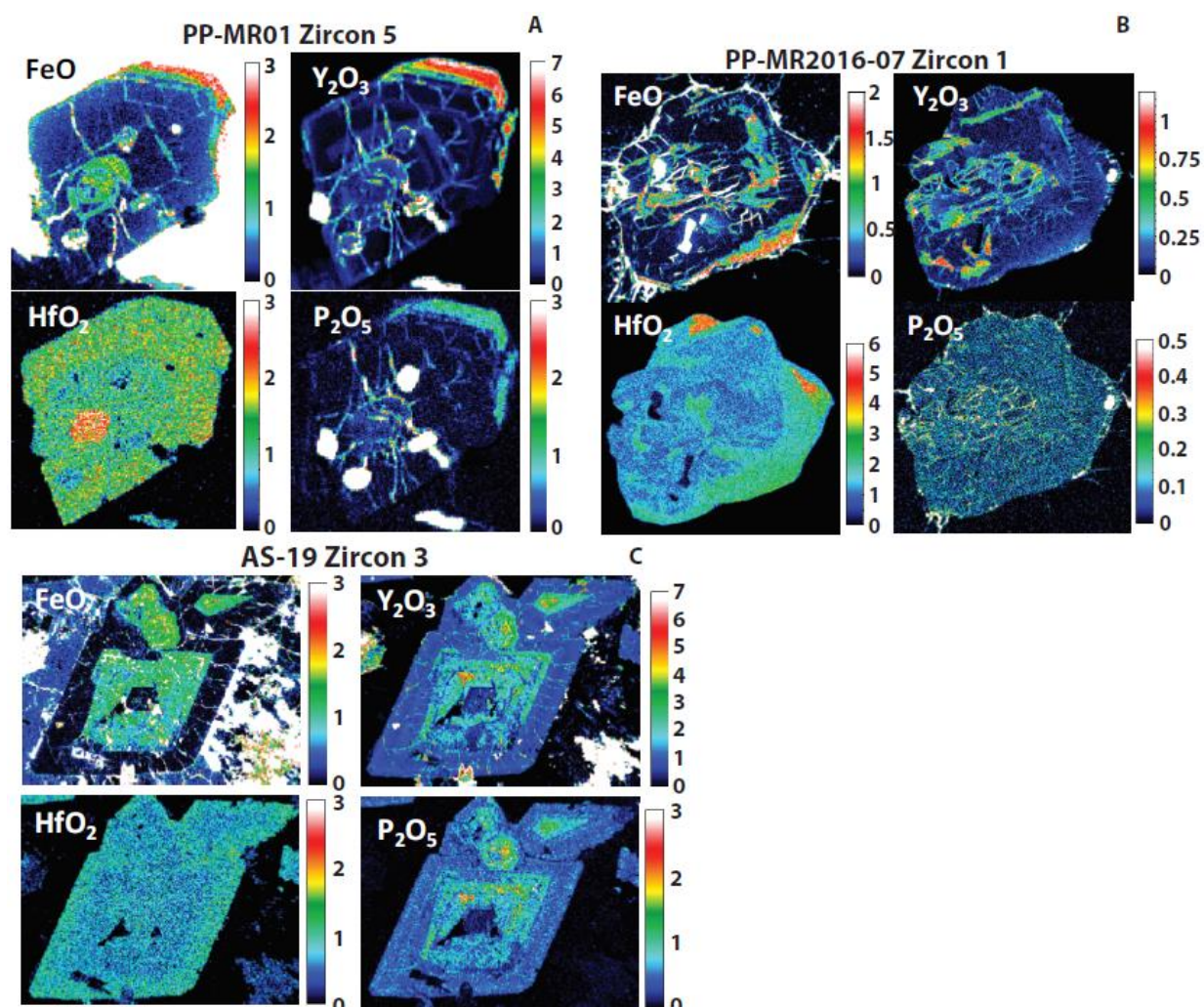


Figure 2.37: EMPA FeO, Y_2O_3 , HfO_2 , and P_2O_5 element maps for zircons found within (A) PPG, (B) MRG, and (C) Type-(I) pegmatites.

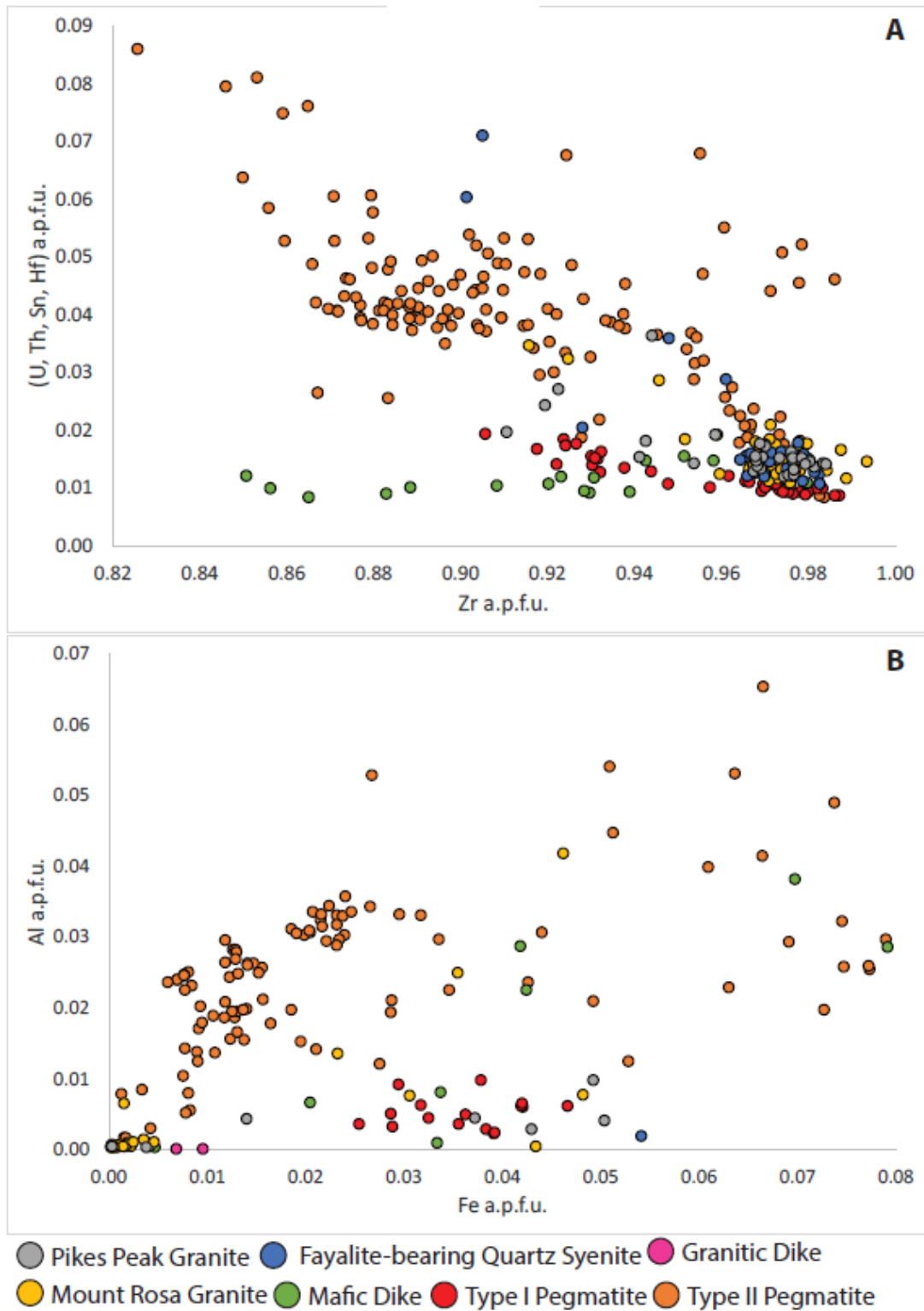


Figure 2.38: Elemental trend plots using EMPA data for zircons from all rock units. (A) Simple substitution plot depicted by Zr vs (U, Th, Sn, Hf), (B) General positive correlation plot depicted by Fe vs Al

Figure 2.39D compares more crystalline analyses to less crystalline analyses within the rock units containing zircons with varying degrees of crystallinity. Points that plot at lower frequencies and elevated linewidths are less crystalline than points with higher frequencies and lower linewidths. These zircons can be compared to the most crystalline zircons in the MRC, the hydrothermal zircons.

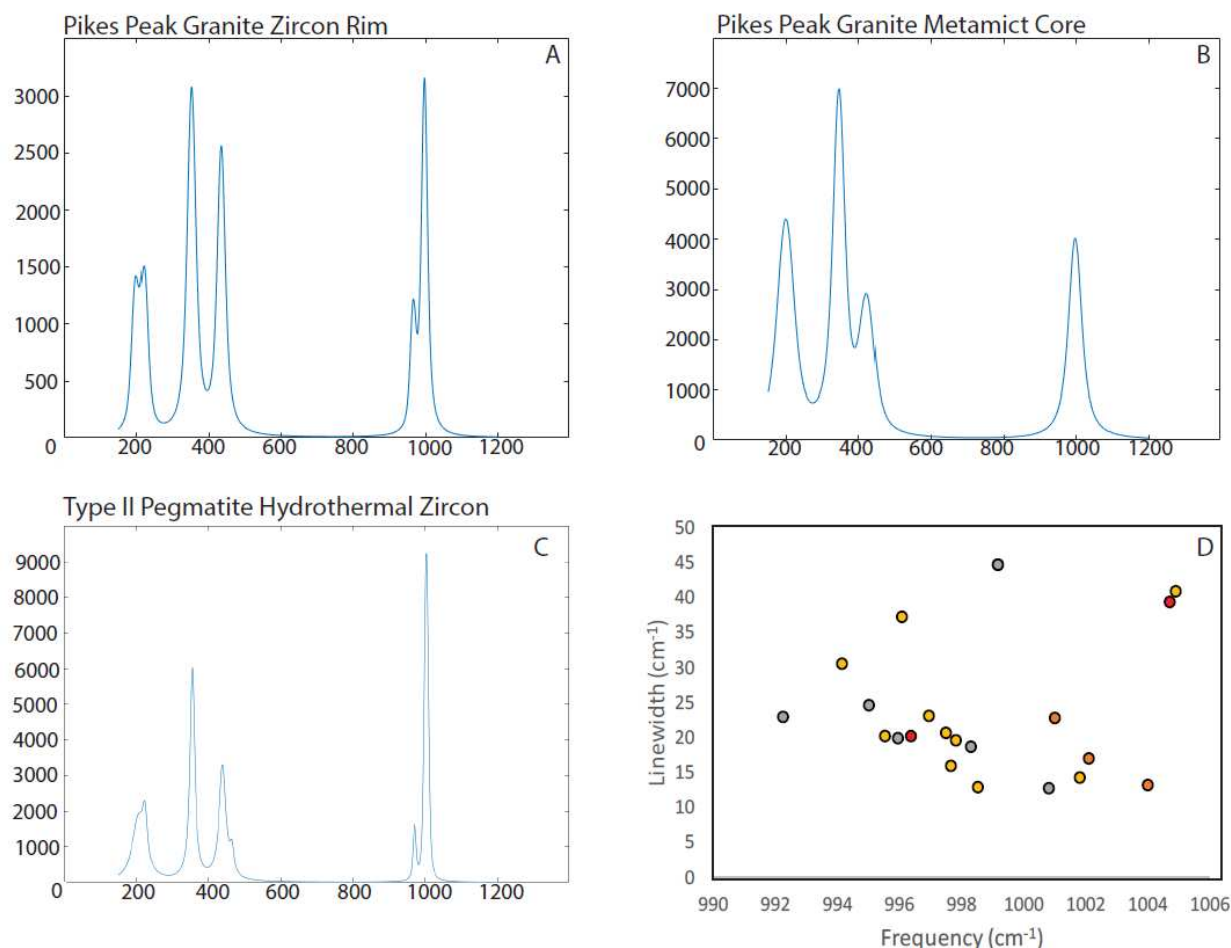


Figure 2.39: Raman spectroscopy data summarized from three distinct spectrums independent to types of zircons and their corresponding zones. (A) Representative spectrum of healthy, unaltered magmatic zircons, (B) representative spectrum of altered, metamict zircon zones, (C) representative spectrum of hydrothermal zircons, (D) frequency versus linewidth plot depicting degree of metamictization within zircons of specific rock units. Gray – Pikes Peak granite, Yellow – Mount Rosa Granite, Red – Type-(I) Pegmatites, Orange – Type-(II) Pegmatites.

2.6 Discussion

The following section discusses the zircons from individual rock units and similarities and differences in both texture and chemistry. These similarities allowed for the grouping of all analyzed

zircons into five groups. Each group will be discussed in detail and further interpreted to better understand the evolution of the MRC.

2.6.1 Zircon Chemistry of the MRC

Following field work, transmitted light petrography, BSE imaging, EDS analyses, automated mineralogy, SEM-CL imaging, EMPA trace element analyses, and raman spectroscopy, zircons were subdivided into magmatic zircons (1), magmatic zircons with hydrothermal overprint (2), and hydrothermal zircons (3). The magmatic zircons are found throughout all rock units in the MRC with the exception of the cores of some type-(II) pegmatites while the hydrothermally overprinted magmatic zircons and hydrothermal zircons are restricted to only some of the type-(II) pegmatites. The zircon groups are described as follows and are summarized in table 2.5:

(1A) Early magmatic zircon (Pikes Peak granite, fayalite-bearing quartz syenite, and type-(I) pegmatites): These zircons present as euhedral with noticeable concentric zoning around a small, undisturbed core. Generally, these are inclusion free with the exception of metamict areas, which host a variety of complex REE-bearing inclusions.

(1B) Magmatic sieve textured zircon (Mound Rosa granite): These zircons are euhedral without any noticeable zoning. Anhedral inclusions (mostly biotite, quartz, and Na-Fe amphibole) can usually be found in high concentrations throughout the zircon grains.

(1C) Magmatic patchy zircon (granitic dikes, Mount Rosa granite, and mafic dikes). These zircons present as euhedral to subhedral with patchy zoning around a patchy core. These zircons host small complex REE-bearing inclusions (i.e. allanite, parisite, and bastnasite) with varying modal abundances.

(2) Wallrock zircon: These zircons are concentrated near the contact between the type-(II) pegmatites and the wallrock with decreasing amounts towards the core of the pegmatite. These zircons are subhedral with patchy zoning and are inclusion free.

Hydrothermal zircons are only found in the core of type-(II) pegmatite and are classified as:

(3) Hydrothermal zircon: These zircons present in a complex network of interconnected veinlets within type-(II) pegmatites, increasing in modal abundance towards the core of the pegmatite. These zircons display as euhedral, but tend to concentrate together to create a complex set of veins throughout the host rock. These zircons can display concentric zoning and are always inclusion free

Table 2.5: Summary table of zircon groups.

Zircon Type	Rock Units	Size	Inclusions	Metamict Zones	Description
1A - Early Magmatic Zircon	Pikes Peak Granite	Between 50 and 100 μm	Monazite, ilmenite, quartz	Yes	Type 1A zircons are euhedral with concentric zoning around a small core. Small, euhedral inclusions are rare in these zircons, but appear abundantly in the metamict zones.
	Faylaite-bearing Quartz Syenite	Between 50 and 100 μm	Monazite, xenotime, apatite	No	
	Type-(I) Pegmatites	Between 250 to > 500 μm	Th-U-Nb - rich Fe-oxides, quartz, fluorite, K-feldspar, columbite, barite, xenotime	Yes	
1B - Magmatic Sieve Textured Zircon	Mount Rosa Granite	Between 200 to > 500 μm	Biotite, K-feldspar, albite, quartz, Na-amphibole	No	Type 1B zircons are isolated to Mount Rosa granite thin sections that do not contain type 1C zircons. These zircons are euhedral with an abundance of large euhedral to subhedral inclusions unrestricted to a particular zone within the zircon. Zonation is difficult to observe, but patchy when present.
1C - Magmatic Patchy Zircon	Granitic Dikes	Between 40 and 100 μm	U-rich thorite, monazite, xenotime, apatite, biotite	No	Type 1C appear as euhedral with a large concentration of euhedral inclusions unrestricted to a particular zone within the zircons. Zircon zoning is patchy and inclusion abundance increases in the metamict zones found in the Mount Rosa granite zircons.
	Mount Rosa Granite	Between 100 and 150 μm	Quartz, biotite, U-rich thorite, Th-bearing Fe-oxide, monazite, Y-rich fluorite	Yes	
	Mafic Dikes	Between 20 and 75 μm	Parasite, allanite, bastnasite, columbite	No	
2 - Wallrock Zircon	Type-(II) Pegmatites	Between 10 and 40 μm	None	No	Type 2 zircons are interpreted to be magmatic zircons with hydrothermal overprint textures. These zircons are isolated to the wallrock of the type-(II) pegmatites with decreasing abundance towards the core. Zoning can be patchy or concentric. These zircons are always surrounded by a halo of inclusion-free quartz.
3 - Hydrothermal Zircon	Type-(II) Pegmatites	Between 2 and 10 μm	None	No	Type 3 zircons are interpreted to be hydrothermal zircons found in the interior and core of the type-(II) pegmatites. These zircons display either concentric zoning or no zoning at all. These zircons cluster together in complex vein networks and are hosted in quartz and fluorite.

Figure 2.40 illustrates the chemical signature of zircon in different rock units based on their texture (zircon type). In general, wallrock and hydrothermal zircons display elevated concentrations in REEs (specifically, heavy REEs), Y, Ca, Fe, and Al while other elements such as Mn and P remain relatively consistent across zircon types (Fig. 2.40A-E). Higher concentrations of these elements observed in the type 1A and type 1C zircons is almost always restricted to the metamict zones. On the contrary, some elements such as P generally remains consistent regardless of zircon type or intensity of metamictization (Fig. 2.40F). Xenotime substitution ($\text{REE}^{3+} + \text{P}^{5+} = \text{Zr}^{4+} + \text{Si}^{4+}$) is the primary mechanism for REE substitution into the zircon's crystal lattice, which is consistent with zircons from other peralkaline complexes such as Thor Lake and Strange Lake, (Fig. 2.41A; Hoshino et al., 2012; Gysi et al., 2016). The more minor rock units (Fayalite-bearing Quartz Syenite, granitic dikes, and the mafic dikes) do not plot on the xenotime substitution plot due to a lack in P in their structure (Fig. 2.36G). The rock units with low quantities of P (PPG, MRG, type-(I) and type-(II) pegmatites) follows trends nicely with the zircons of Strange Lake, Canada and the Sierra Blanca Peaks, Texas (Rubin et al., 1993; Gysi et al., 2016). Zircons analyzed by Hoshino et al. (2012) have higher concentrations of P + (REE,Y) a.p.f.u. values, although the slope is the same as observed in zircons from the type-(II) pegmatites (Fig. 2.41A). Additionally, the variability in Zr concentration is attributed to the substitution of incompatible HFSE into the zircon structures through simple substitution mechanisms (Fig. 2.41B). The older rock units (PPG, Fayalite-bearing Quartz Syenite, and granitic dikes) generally concentrate near the zircons from Thor Lake, Canada (Sheard et al., 2012). The mafic dike zircons follow a 1:0 slope, which display a similar trend to the zircons of Thor Lake, Canada (Hoshino et al., 2012) and Strange Lake, Canada (Gysi et al., 2016). Type-(I) pegmatite zircons display a slightly elevated slope to those of the mafic dikes. The type-(II) pegmatite zircons follow the same slope as the Sierra Blanca Peak zircons (Rubin et al., 1993), however are comparatively less enriched in HFSE. A few of the PPG and Fayalite-bearing Quartz Syenite zircons deviate from their main cluster to follow trend with the type-(II) pegmatite zircons.

Type 1A zircons are found in PPG and Fayalite-bearing Quartz Syenite, as well as type-(I) pegmatites, one of the youngest rock units. These zircons range in size between 50 and 125 μm in the PPG and Fayalite-bearing Quartz Syenite while the zircons in the type-(I) pegmatites range between 250 to >500 μm . All zircons defined as type 1A display 1:2 to 1:4 aspect ratios with a characteristic dipyrimal morphology. Type 1A zircons display concentric zoning, oftentimes evident in transmitted light, BSE, and CL imaging (Figs. 2.7A, 2.7D, 2.11C, 2.11D, 2.11E, 2.29A and 2.29C). Rare patchy zoning is observed in metamict cores of the PPG. All zircons are euhedral and inclusions are rare. When inclusions are present,



Figure 2.40: Zircon distribution based on type 1A, 1B, 1C, 2, and 3 (see text for description). Triangles are EMPA points collected from metamict zones and squares represent the mafic dikes (type 1C).

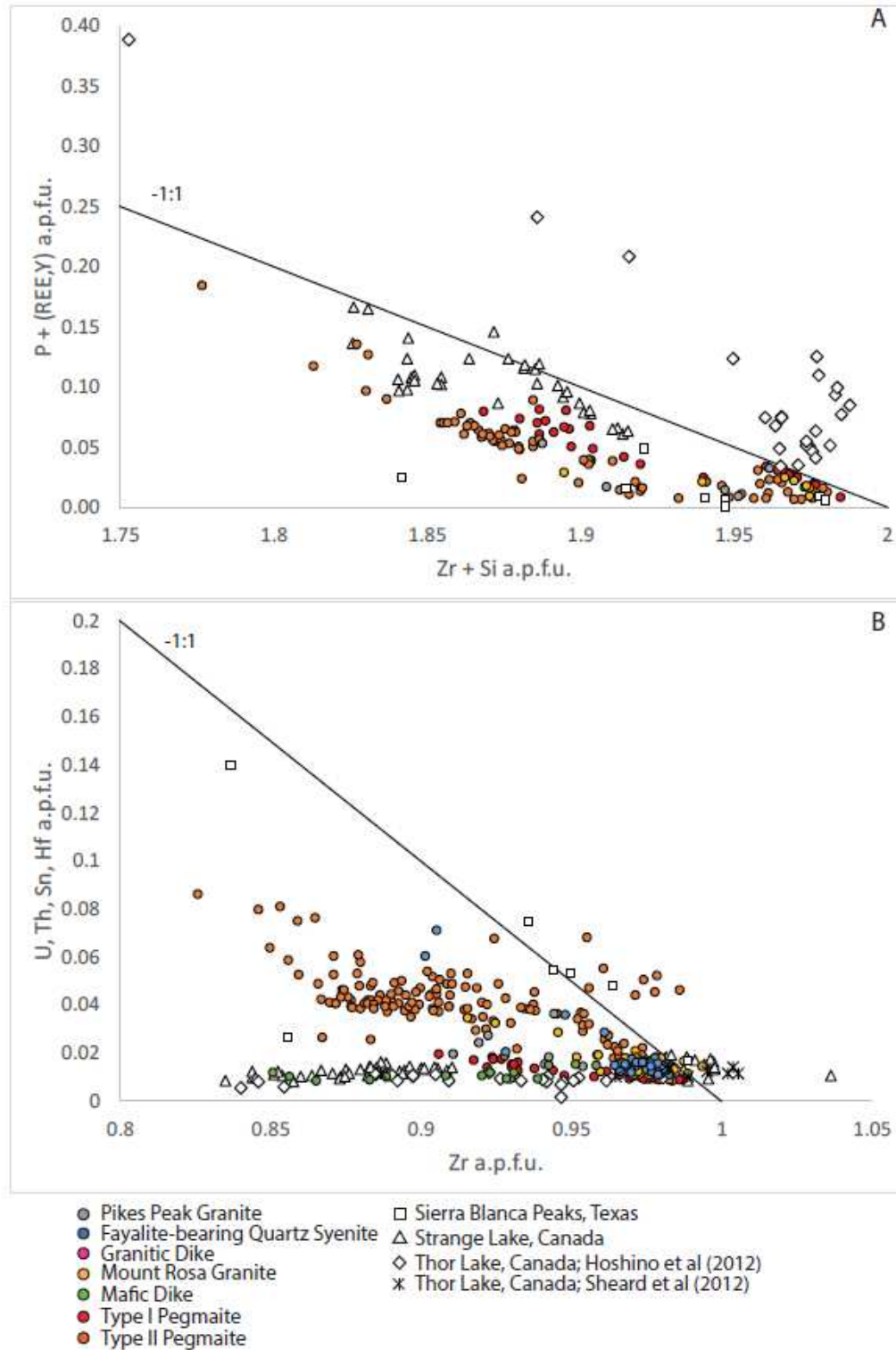


Figure 2.41: Zircon substitution plots with representative data from the Sierra Blanca Peaks, Texas (Rubin et al., 1993), Strange Lake Canada (Gysi et al., 2016), and Thor Lake, Canada (Sheard et al., 2012; Hoshino et al., 2012). (A) Xenotime coupled substitution and (B) simple substitution. 1:1 slopes denoted by the black line running across both plots.

they most commonly consist of monazite, xenotime, Fe-oxides, and thorite. Zircons within the PPG and Fayalite-bearing Quartz Syenite are commonly associated with biotite, while type-(I) pegmatite zircons do not show a preferred mineral association. Silica concentrations in type 1A zircons range between 13.96 and 15.46 wt% while Zr concentrations range between 39.62 and 49.12 wt%. EMPA spots with lower Si and Zr concentrations are analyses in metamict zones, which are also paired with overall lower totals (94.14-96.50 wt% analysis total). Based on morphology, type 1A zircons crystallized very early in the crystallization sequence. Elevated REE and HFSE concentrations relative to mantle sourced zircons are common in these zircons, especially in the zones of metamictization (Fig. 2.42A and C). Undisturbed zones of the PPG and Fayalite-Bearing Quartz Syenite type 1A zircons display around 5,000 ppm REE+Y, 1,000 ppm U, 15,000 ppm Hf and 1,500 ppm Th. Type-(I) pegmatite zircons are generally more elevated in incompatibles, with concentrations of about 18,000 ppm REE, 1,000 ppm U, 9,000 ppm Hf, and 1,000 ppm Th. Unique to the type 1A zircons is the presence of homogeneous cores followed by concentric zoning, which is also a texture reported in zircons of the peraluminous Monte Capanne pluton, Italy (Gagnevin et al., 2010).

Type 1B zircons are only found in some samples in the MRG. These are generally larger, between 200 and >500 μm in size. Type 1B zircons are concentrated with large subhedral to anhedral inclusions, which are mineralogically “simple” compared to other zircons. Inclusions are commonly quartz, biotite, K-feldspar, albite, and Na-amphibole (arfvedsonite). Inclusions are so abundant in these zircons (Fig. 2.18), zoning patterns are difficult to discern, but some small areas display patchy zonation. REE concentrations are elevated relative to the 1A PPG and Fayalite-bearing Quartz Syenite zircons (between 9,000 and 13,000 ppm), but less than the type-(I) pegmatite zircons. Other incompatibles such as Th and U are very low or below the detection limit. Hafnium is fairly high, around 11,000 ppm. While these zircons display a texture unlike any others observed in the MRC, their elemental concentrations are overall very similar to other type 1 zircons (Fig. 2.40). Following literature review, zircons displaying an inclusion texture this extreme was not found, but the subhedral to anhedral nature of the inclusions and frequency is interpreted to be due to rapid zircon crystallization (Corfu et al., 2003).

Type 1C zircons are found in the granitic dikes, some MRG samples (PP-MR2016-07 and PP-MR2016-13), and the mafic dikes. The granitic dike and MRG zircons typically range between 50 and 150 μm in size while the mafic dike zircons are a little smaller at 40 to 75 μm in size. Zircons of the MRG display as euhedral while granitic dike and mafic dike zircons are subhedral. All zircons of this category present 1:1 to 1:4 aspect ratios. Patchy zoning is characteristic of these zircons, with no concentric zoning

observed in BSE and CL imaging (Figs. 2.15A, 2.22A, 2.22B, 2.22C, and 2.26B). Gagnevin et al. (2010) report patchy zoning similar to this type of zircon within the peraluminous Monte Capanne Pluton, Italy, and interprets the texture to be due to magma partitioning and mixing. Type 1C zircons are defined by a high concentration of small euhedral to subhedral inclusions (Figs. 2.14A, 2.22D, 2.22F, 2.25B, and 2.25C). Inclusions are commonly thorite (U-rich), albite, Fe-oxide, monazite, and quartz. Additionally, yttrifluorite is common in type 1C MRG zircons. Inclusions are widely dispersed throughout the zircons, and are generally not restricted to a particular zone. Most type 1C category display an abundance of inclusions throughout the entire zircon crystal. Silicon concentrations for these zircons ranges between 13.28 and 15.38 wt% with Zr values of 37.89 to 39.52 wt%. Similar to the type 1A zircons, higher values are constrained to metamict zones. Chemical analyses from type 1C zircons from the granitic dike show the same chemical signature as the type 1C zircons from the MRG, while mafic dike zircons show higher trace element concentrations compared to the granitic dike and MRG. Elemental concentrations are variable, correlating to patchy zoning, characteristic of the 1C zircons (Fig. 2.43). Type 1C zircons display about 4,000 ppm REE, slightly lower REE concentrations than discussed for type 1A and 1B zircons. High field strength elements display similar concentrations in type 1A PPG and Fayalite-bearing Quartz Syenite zircons with U hovering around 1,000 ppm and Hf a little more elevated at 15,000 ppm. Thorium is lower (around 500 ppm) compared to type 1A zircons. On the contrary, the mafic dike type 1C zircons are chemically very similar to type 1A pegmatite zircons with REE concentrations at 16,000 ppm and elevated Hf at 14,500 ppm. Additionally, the mafic dike zircons contain U and Th concentrations below the detection limit. Magmatic zircons reported from the peralkaline Sierra Blanca Peaks, Texas locality are described as “corroded with abundant thorite inclusions” by Rubin et al. (1993), similar to the textures found in type 1C zircons, especially in the peralkaline MRG and mafic dike units. Rubin et al. (1989) suggests the thorite inclusions of the peralkaline Sierra Blanca Peaks, Texas are a product of exsolution from the zircon host, therefore depleting the actual zircon from elevated Th values.

Type 2 zircons are only found in some type-(II) pegmatites and are most abundant at the edge of the pegmatite. The zircons range between 10 to 30 μm in size and are always associated with quartz. The zircons display as subhedral with areas of jagged edges where it looks as if dissolution occurred (Figs. 2.31A, B, and C). Some of these zircons occur as isolated crystals while others grew together in large clusters (Fig. 2.31D). These zircons display concentric zoning and are always inclusion free. The quartz surrounding these zircons is also completely inclusion free. These zircons show Si concentrations ranging between 13.27 and 15.38 wt% and Zr concentrations ranging between 41.22 and 48.14 wt% with about 30% of the totals below 97.00%. Unlike previously discussed zircons, lower analysis totals are not

restricted to metamict zones. Most of these zircons display similar values in incompatible elements as the type 1A zircons of the older rock unit zircons (PPG and Fayalite-bearing Quartz Syenite) while a few outliers are similar to the chemical composition of the younger type-(I) pegmatite and mafic dike units (type 1A and 1C; Fig. 2.40 and 2.44). Most of the zircons display REE values around 3,000 ppm with U only detected in small amounts (300 ppm). Thorium values have a larger range in these zircons, ranging between below the detection limit to greater than 6,000 ppm. One outlier is zircon 6 of thin section AA-MR38-01 (Fig. 2.44). This zircon displays REE values greater than 20,000 with Th values of 3,000 and inconsistent U (bdl to just below 900 ppm). Hf values between 15,000 and 30,000 is common for all zircons of this category.

Type 3 zircons are restricted to some type-(II) pegmatites, and are very abundant when present. These zircons range between 1.0 and 10 μm in size and crystallize as complex veinlets in clusters and rarely independently (Fig. 2.34D). Occasionally, these veinlets will outline what is interpreted to be prior crystallized minerals, but have since dissolved and become replaced by later-stage quartz, fluorite, and zircon (Fig. 2.34C). Type 3 zircons are always associated with fluorite and quartz. Concentric zoning can be observed in these zircons (Fig. 2.34A), but is not always present. Furthermore, these zircons are always inclusion-free. Type 3 zircons display the lowest Si values, Zr values, and overall totals compared to all zircons of the MRC, but have the highest concentration of incompatible elements (Table 2.3). Si values range between 10.95 and 15.42 wt% while Zr values range between 34.80 and 44.41 wt% with analytical totals commonly between 94 and 96%. Low totals for hydrothermal zircon have been reported such as the peralkaline Nechalacho deposit in Thor Lake, Canada (Sheard et al., 2012; Hoshino et al., 2012) and are interpreted to be due to the incorporation of H_2O into the crystallographic structure. REE values for these zircons concentrate around 20,000 ppm with plenty of analyses reaching 30,000 ppm or higher (Fig 2.40 and 2.45). Additionally, Fe becomes incorporated into these zircons at around 6,000 ppm but all U

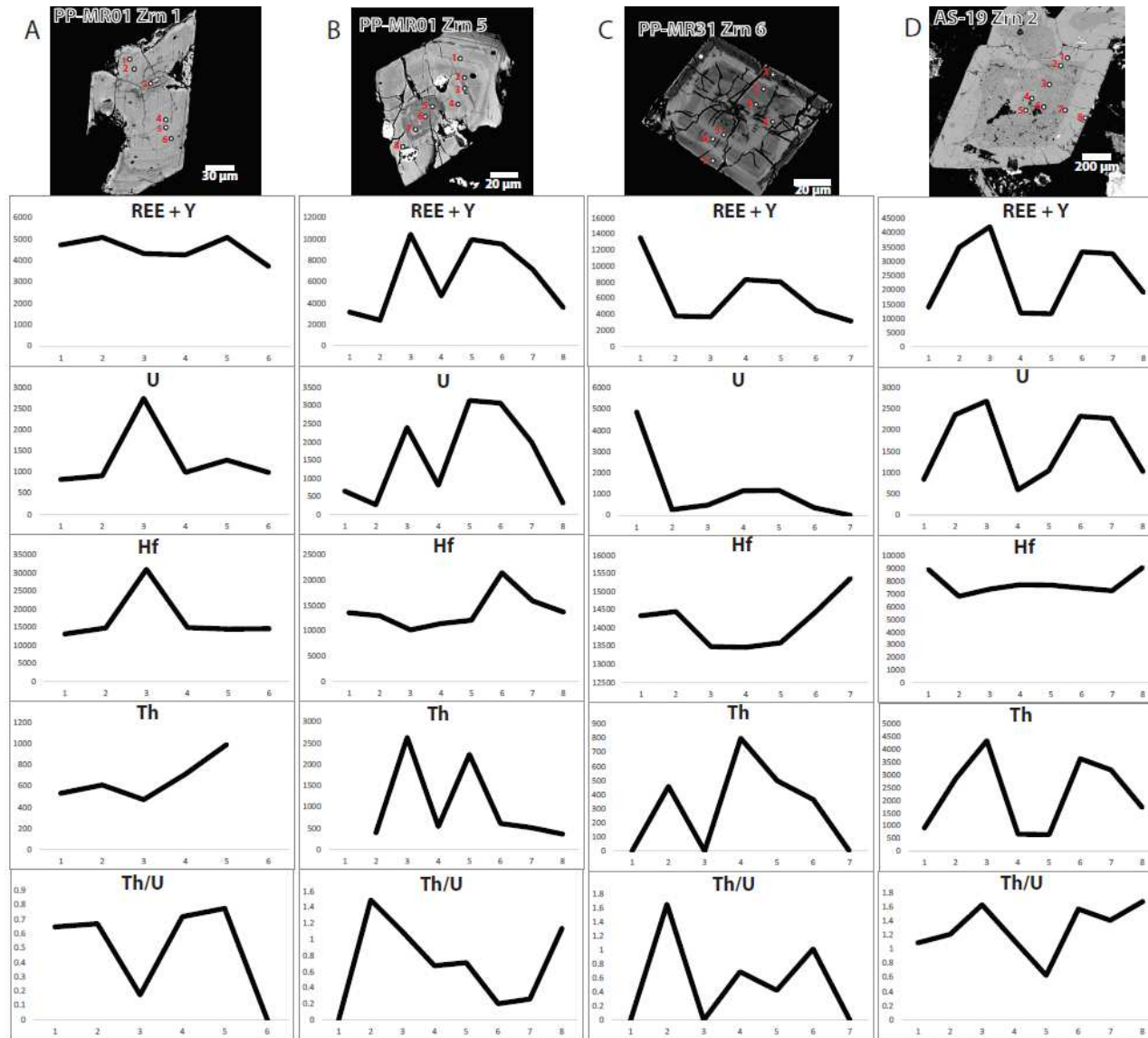


Figure 2.42: Zircon traverse plots illustrating variation in (REE+Y), U, Hf, Th, and Th/U values within type 1A zircon grains. (A) PPG, (B) PPG, (C) Fayalite-bearing Quartz Syenite, (D) type-(I) pegmatite.

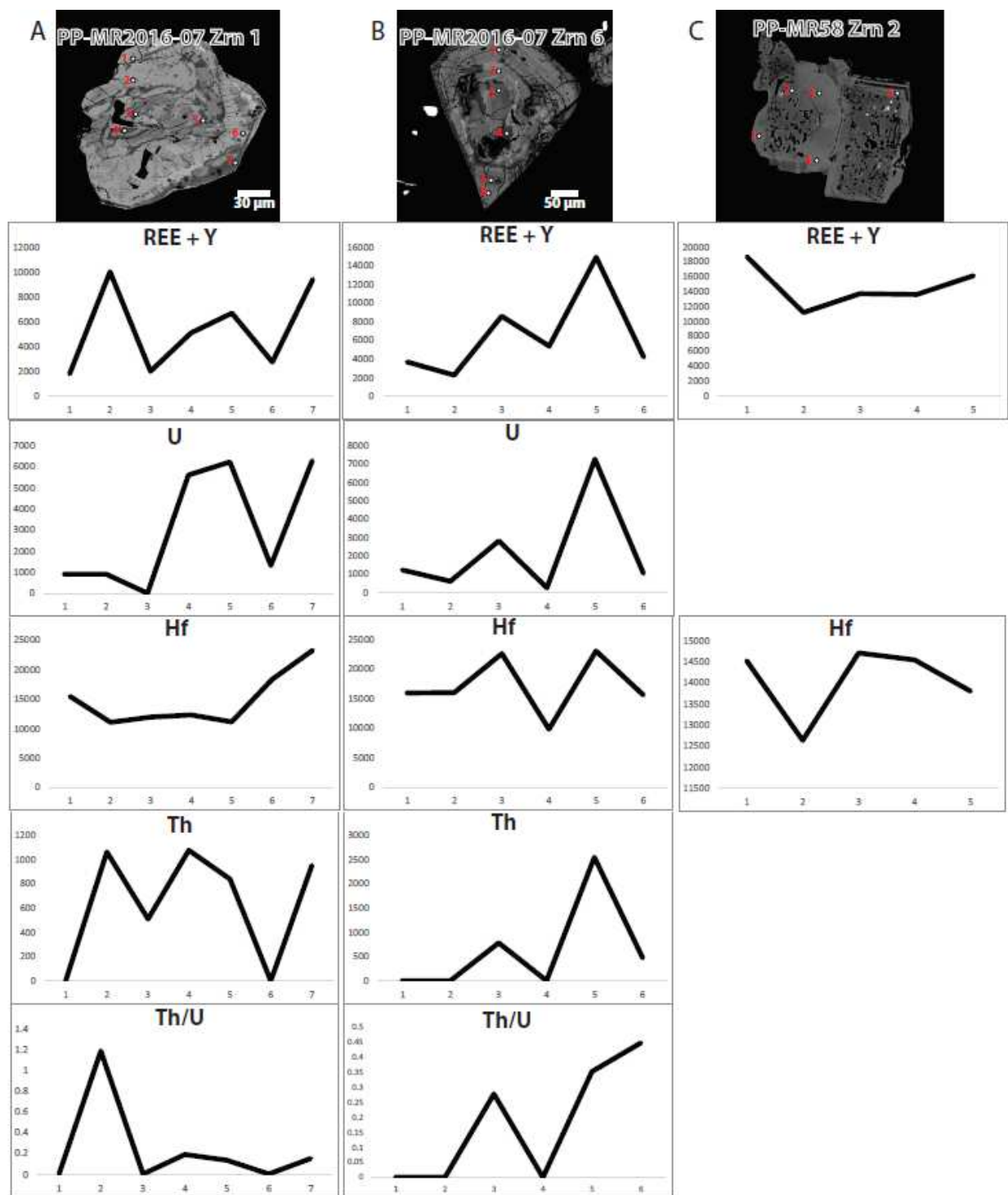


Figure 2.43: Zircon traverse plots illustrating variation in (REE+Y), U, Hf, Th, and Th/U values (where applicable) within type 1C zircon grains. (A) MRG patchy zircon, (B) MRG patchy zircon, (C) mafic dike.

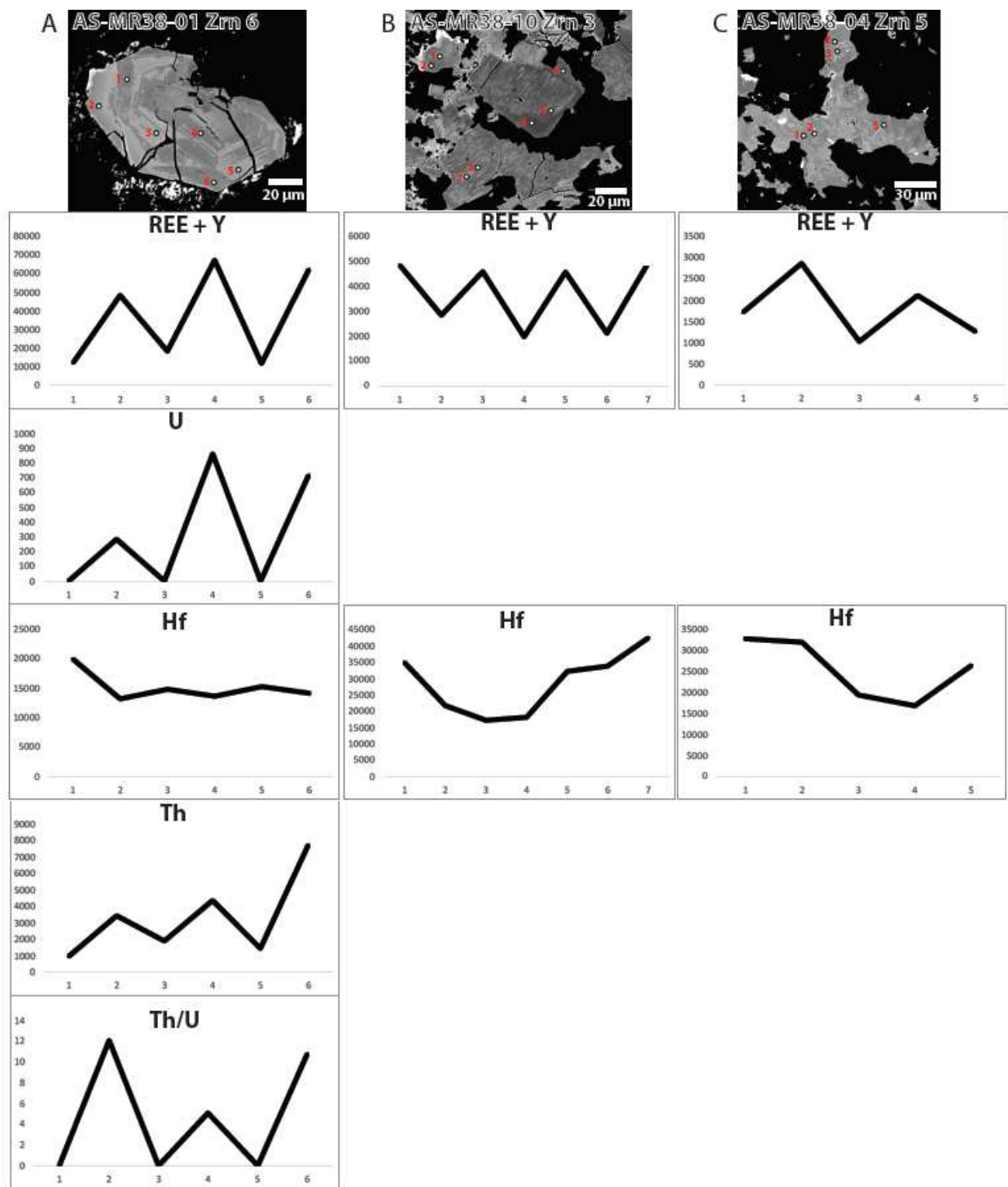


Figure 2.44: Zircon traverse plots illustrating variation in (REE+Y), U, Hf, Th, and Th/U values (where applicable) within type 2 zircon grains. (A) Type-(II) pegmatite zircon from the pegmatite rim, (B) Type-(II) pegmatite zircon between the rim and the core, (C) Type-(II) rim pegmatite zircon collected from the other side of the pegmatite.

concentrations were below the detection limit. Hf values for these zircons remained around 30,000 ppm with some exceeding 40,000 ppm while Th values ranged between 8,000 ppm to 12,000 ppm.

Hydrothermal zircons similar to type 3 zircons have been reported in other localities such as the peraluminous Christmas Mountains of the Sierra Blanca Peaks, Texas (Rubin et al., 1989; 1993). Zircons of the Sierra Blanca Peaks are hosted in peraluminous laccoliths and have similar petrographic and chemical compositions to the MRC type 3 zircons. Texturally, the Christmas Mountain zircons display irregular boundaries, are too small for petrographic analysis, and are hosted in fluorite. These zircons are almost inclusion-free with the exception of occasional Fe-oxides. Chemically, Christmas Mountain zircons display lower Hf concentrations at around 1.1-2.2 wt%, however Rubin et al. (1989) report hydrothermal zircon overgrowths and “stringers” with Hf concentrations between 5.1 and 7.6 wt%. The large range in Hf concentration is very similar to concentrations detected in type 3 zircons. Rubin et al. (1989) attribute the large range in Hf to multiple fluid pulses with varying Hf concentrations. Hydrothermal zircons hosted in peralkaline intrusions such as Strange Lake, Canada have also been documented (Gysi et al., 2016). In addition to chemical similarities to both the Christmas Mountains and the MRC, the hydrothermal zircons of Strange Lake also display low analytical totals (as low as 98.1%).

Metamict zircon zones are present in the type 1A and 1C zircons. They occur in some of the cores of the PPG, as a roughly 100 μm zone, in the interior of type-(I) pegmatite zircons, and in some areas of patchy zonation throughout the MRG patchy zircons. These metamict zones were discerned using a combination of physical and chemical techniques including transmitted light petrography, textural relationships observed in BSE imaging, EMPA trace element chemistry, and Raman spectroscopy. Metamict zircon forms from the radioactive decay of trace amounts of Th and U (substituting for Zr) incorporated into the zircon structure (Nasdala et al., 2001). Over time, atomic displacements through the dissipation of particle energy occurs due to the alpha decay of radio-nuclides and forms point defects (Tromans, 2006). This effect results in a darker brown spongy texture, which can usually be discerned in transmitted light petrography (Fig. 2.28A) and is especially evident in the type-(I) pegmatite zircons, but can also be recognized in some cores of the PPG zircons and areas of the patchy MRG zircons. In crossed polarized light, these zones transition from the bright second order colors characteristic of zircons to dull first order colors. This phenomenon is not uncommon as many reports of this observation have been published in both igneous and metamorphic zircons such as the Jack Hills, Australia, and the Pütürge metamorphite (Nasdala et al., 2001 and Kihc, 2016). Additional effects of prolonged radiation damage is the decrease in density and swelling of the metamict layers, resulting in fracturing of the zircon (Tromans,

2006), which is observed in BSE images of all zircons possessing metamict layers throughout the MRC (Figs. 2.7B, 2.7F, 2.22A, 2.22B, 2.29A, 2.29C, and 2.29D). In addition to the fracturing networks, metamict layers are characterized as having a high concentration of inclusions relative to other zones and display as a darker shade of gray in BSE.

Chemically, metamict zones display elevated concentrations of elements such as Fe (0.02-1.41 wt%), U (0.03-0.73 wt%), Th (0.03-0.88 wt%), and REE+Y (0.21-4.22 wt%), with Si ranging between 12.96-15.39 wt% and Zr ranging between 39.62-48.96 wt%. Additionally, Th/U values are typically <1 except for the type-(I) pegmatite zircons, which are about 3.0. Based on equations presented by Nasdala et al. (2001), type 1A zircons took just under 250 m.y. to reach the first percolation threshold (2.2×10^{18}), type 1C zircons took roughly 100 m.y., and type-(I) pegmatite zircons took about 180 m.y. These zones contribute to a bimodal distribution in chemistry, where the metamict areas are enriched in incompatible elements while the “healthy” zones display lower values, but still elevated concentrations compared to mantle-derived zircons (Fig. 2.46). While chemically point 3 of thin section PP-MR01 displays similar elevated values as the metamict core of the zircon, the zone was too small for textural verification. EMPA totals as low as 91.63% are observed for metamict zones, but low totals (<90% at times) are a commonly reported feature from metamict zircons from the Spanish Central System and the Sierra Blanca Peaks (Rubin et al., 1989; Pérez-Soba et al., 2007; Hoshino et al., 2012). Many studies have been conducted using Raman spectroscopy and the relationships between the acquired spectra and degree of metamictization observed in zircons (Nasdala et al., 1995; Nasdala et al., 2001). Their results stated as the degree of metamictization increases in zircons, the intensities of the peaks become lower and the width of the peaks increase, decreasing the peak’s sharpness (Nasdala et al., 1995). Additionally, metamict peaks tend to shift towards lower wavenumbers, which is observed in these zircons relative to crystalline zones (Fig. 2.39B). Raman spectra of metamict zones within the MRC typically display full width at half-maximum values up to 44.67 cm^{-1} whereas more crystalline zircon zones within the same grains displayed values up to 22.96 cm^{-1} . Additionally, Raman spectroscopy was utilized in order to detect potential water within the metamict zones, which would aid in the explanation of low EMPA totals. No water (or other hydroxyl groups) were detected in these zones, so it is suggested the low EMPA totals are due to vacancies within these zones.

2.6.2 Evolution of the MRC

The Mount Rosa Complex (MRC) consists of six rock units: the peraluminous Pikes Peak granite (PPG), Fayalite-bearing Quartz Syenite, granitic dikes, peralkaline Na-amphibole Mount Rosa granite

(MRG), mafic dikes, and NYF-type pegmatites (listed from oldest to youngest). The NYF-type pegmatites are further divided into type-(I) pegmatites, which are more abundant and mineralogically simple and type-(II) pegmatites, which occur in clusters and are mineralogically more complex.

Magmatic Evolution of the MRC

The peraluminous Pikes Peak Granite (Type 1A zircon) is the dominant rock unit of the Pikes Peak Batholith and was emplaced about 1.1 Ga (Smith et al., 1999). This event was activated during the mid-continental rift, which was the main mechanism for A-type magma production throughout North America. Whole rock data elevated in REE and HFSE concentrations as well as recent Lu-Hf isotope data on zircons (Guitreau et al., 2016) suggest crustal contamination during ascent and emplacement of the Pikes Peak Batholith (Smith et al., 1999; Persson, 2017). The peraluminous PPG, which makes up a large amount of the batholith occurs as subsolvus and hypersolvus granite (Smith et al., 1999). Zircons of the PPG (type 1A) display elevated concentrations of incompatible trace elements for an unevolved magmatic melt sourced from A-type magmatism; with the highest concentrations constrained to the metamict cores. Zircons in the PPG usually occur as inclusions in biotite with nicely developed faces, suggesting the magma reached zircon saturation and nucleation early (Hoskin and Schaltegger, 2003). Concentric zoning in these zircons occurs in narrow growth bands, oftentimes around a homogeneous core, similar to zircons in the peraluminous Monte Capanne pluton, Italy (Gagnevin et al., 2010). Zircon core to rim element data (Fig. 2.42A) suggest an enrichment in most elements towards the core, but with little variation among the narrow zones. Gagnevin et al. (2010) suggest narrow growth bands of concentric zoning to be due to large-scale changes within the magma body, such as additional influxes of magma. Variations in the Th/U ratios (0-1.6) could be suggestive of temperature changes influenced by magma influx or zircon migration (from cooler to warmer regions or vice versa) within the magma chamber (Kirkland et al., 2014), also resulting in narrow growth bands. The PPG zircons suggest possible crustal contamination due to the elevated REE+Y values (between 2,000 and 10,000 ppm), which are high when compared to zircons of mantle affinity (between 16 and 113 ppm from kimberlitic zircons in south Africa; Belousova et al., 1998), however elevated concentrations could be obtained by an originally enriched magma source. Trace element concentrations in zircons from the PPG are comparable to crustal zircons, which display average values of around 1 wt% REE+Y (Hoskin and Schaltegger, 2003) and is also supported by Lu-Hf data suggesting crustal contamination (Guitreau et al., 2016).

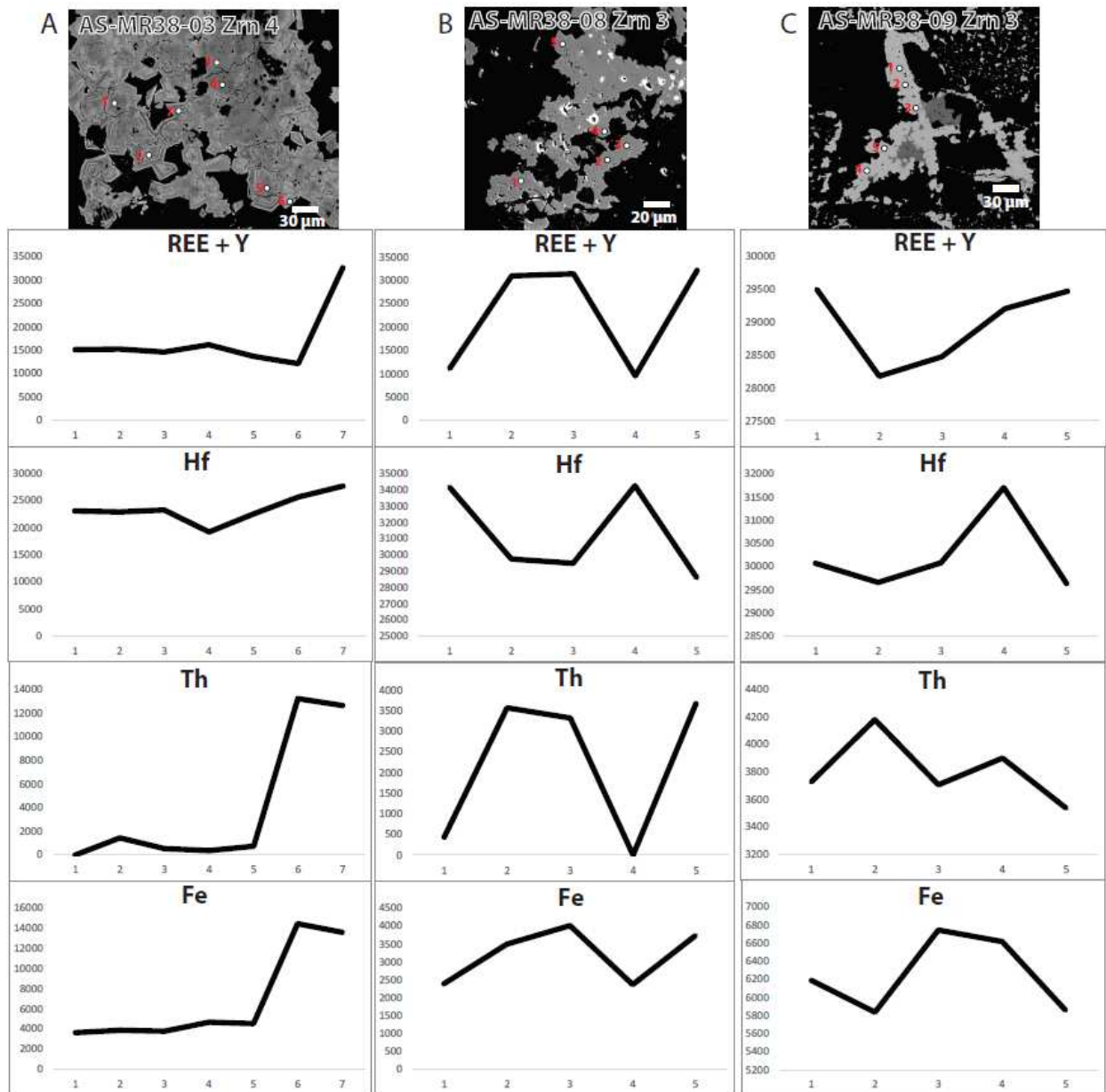


Figure 2.45: Zircon traverse plots illustrating variation in (REE+Y), U, Hf, Th, Iron within type 3 zircon grains. (A) Type-(II) pegmatite hydrothermal zircon from between the wallrock and core with concentric zoning, (B) Type-(II) pegmatite hydrothermal zircon from between the wallrock and core with no zoning, (C) Type-(II) pegmatite hydrothermal zircon from between the wallrock and and core with no zoning.

The Fayalite-bearing Quartz Syenite (Type 1A zircon) displays zircon textures comparable to those of the PPG, except these zircons lack metamict zones. Additionally, like the PPG, the zircons are commonly hosted in biotite, and occur heterogeneously throughout the thin sections (Fig. 2.12A).

Chemically, these zircons display some of the lowest concentrations of incompatible elements of all zircons analyzed in the MRC (average of 0.61 wt% REE+Y compared to an average of 0.82 wt% REE+Y in the PPG; Table 2). Concentric zones texturally appear similar to those in the PPG, but chemically the zones do not appear the same as the PPG zones. However, whole rock chemical analysis presents an enrichment in REE and HFSE relative to the older peraluminous PPG and younger peraluminous granitic dikes (Persson, 2017). This anomaly is similar to that observed in the fayalite-bearing syenite intrusion of Misery Lake, Canada, an A-type igneous pluton with high concentrations of REE and HFSE bearing minerals within quartz-fayalite dikes containing zircon and REE-bearing minerals (Petrella et al., 2014). In the Fayalite-bearing Quartz Syenite, REE enrichment comes from minerals co-crystallizing with zircon rather than zircon being a large carrier of REE. In fayalite syenites from other deposits (i.e. Thor Lake, Canada and Strange Lake, Canada) REE enrichment is generally confined to elevated concentrations within zircons. Petrella et al. (2014) suggests quartz-fayalite dikes in the Misery Lake complex are sourced from an FeO-SiO₂ bearing fluid that separated from a fractionated magma, which sequestered Zr, Nb, and REE. A process similar to this could explain the crystallization of zircon, columbite, and REE-bearing minerals (bastnasite, parisite, and allanite) as separate minerals rather than the uptake of HFSE/REE into the zircon structure due to the extreme enrichment of these elements. Whole rock geochemistry and similar biotite compositions paired with overlapping age dates suggests this unit is co-magmatic with the PPB (Persson, 2017).

Granitic dikes (Type 1C zircons) are volumetrically minor compared to other rock units in the MRC. This unit is interpreted to be younger than the Fayalite-bearing Quartz Syenite yet older than the MRG due to its cross-cutting relationships with the Fayalite-bearing Quartz Syenite and radial geometry around the MRG (Gross, 1962; Barker et al., 1975; Persson, 2017). These zircons classify as type 1C but present similar in chemistry as the earlier two units (type 1A zircons). This unit is peraluminous (Persson, 2017), and EMPA analysis points on zircons display similar REE and HFSE concentrations compared to the PPG. While conclusions are difficult to draw from zircon chemical data, texturally these zircons are different from older rock units. BSE images generally display a lack of zonation in granitic dike zircons and a lack of CL reactivity. The presence of REE-bearing inclusions (thorite and monazite) throughout the zircons are noteworthy since inclusions oftentimes provide valuable information when interpreting crystallization conditions (Corfu et al., 2003). The REE-bearing inclusions display as euhedral, suggesting co-crystallization with zircon. Abundant inclusions co-crystallizing with zircons early in the crystallization sequence suggest this magma was saturated with respect to incompatible elements leading to the immediate crystallization of zircon, thorite and monazite.

The peralkaline Mount Rosa Granite (type 1B and 1C zircons) was initially suggested to be sourced from a separate magmatic body unrelated to other rock units of the MRC (Gross, 1962; Smith, 1999). However recent research proposes the MRG to be co-magmatic with the PPG (Persson, 2017) based on both field relationships and chemical evidence. Two distinct zircons types (type 1B (sieve textured) and type 1C (patchy)) are present throughout the MRG, but generally do not occur together within one sample. Consistent with whole rock analyses presented by Persson (2017), both zircon types display an enrichment in REE/HFSE relative to the PPG, Fayalite-bearing Quartz Syenite and granitic dike zircons (Figs. 2.36 and 2.40; Table 2.3). Although euhedral, type 1B zircons (sieve textured) display many forms of disequilibrium textures such as patchy zoning and an abundance of anhedral inclusions (Fig. 2.18). The abundance of anhedral inclusions without a preferential crystallization zone throughout the zircon and the large size of these zircons (at times >500 μm) suggests that the system was Zr-oversaturated, allowing for rapid and large zircon crystallization (Corfu et al., 2003; Kelley, per. Comm.). Type 1C (patchy) zircons in the MRG, however, display a very patchy texture in BSE images. These zircons possess an abundance of euhedral to subhedral microinclusions (HFSE and REE-bearing minerals such as yttrifluorite, monazite, and thorite) crystallized as HFSE and REE bearing minerals, very similar to those observed in the granitic dikes. The darker zones of the patchy texture are zones of metamictization, and commonly (but not exclusively) host to the inclusions. Chemical analyses of these type 1C (patchy) zircons typically display a bimodal distribution, where the darker metamict zones are enriched in Fe, Al, Ca, REE, and HFSE relative to the lighter zones (Figs. 2.43A, 2.43B, 2.46B). Generally, type 1B (sieve textured) zircons are chemically less enriched relative to type 1C (patchy) zircons (Figs. 2.36 and 2.40). However REE concentrations of type 1B (sieve textured) and type 1C (patchy) zircons are similar in value (Table 2.3). This suggests the overall REE concentration in the melt that crystallized the patchy (type 1C) zircons and the corresponding REE-bearing mineral inclusions (i.e. monazite, thorite, yttrifluorite) was highly enriched in REE and HFSE. This enrichment allowed the magma to reach REE and HFSE saturation, allowing for the co-crystallization of both zircon and REE/HFSE bearing minerals.

Field evidence suggests that the MRG units intruded in multiple pulses and crops out in layered intrusive bodies. Moreover, the MRG is heterogeneous in both grain size and mineralogy (Fig. 2.47). Compositionally, areas of the MRG display a strong peralkaline signature (i.e. elevated concentrations of Na-Fe amphibole and astrophyllite phenocrysts) with irregular, undulating boundaries with less Na-Fe amphibole and no astrophyllite (Figs. 2.47A, C, and D). These boundary layers are almost always very irregular and in field outcrops remind of textures interpreted to represent magma mingling. It is

noteworthy that sieved (type 1B) and patchy (type 1C) MRG zircons typically do not coexist within one thin section, but rather occur in samples from different localities.

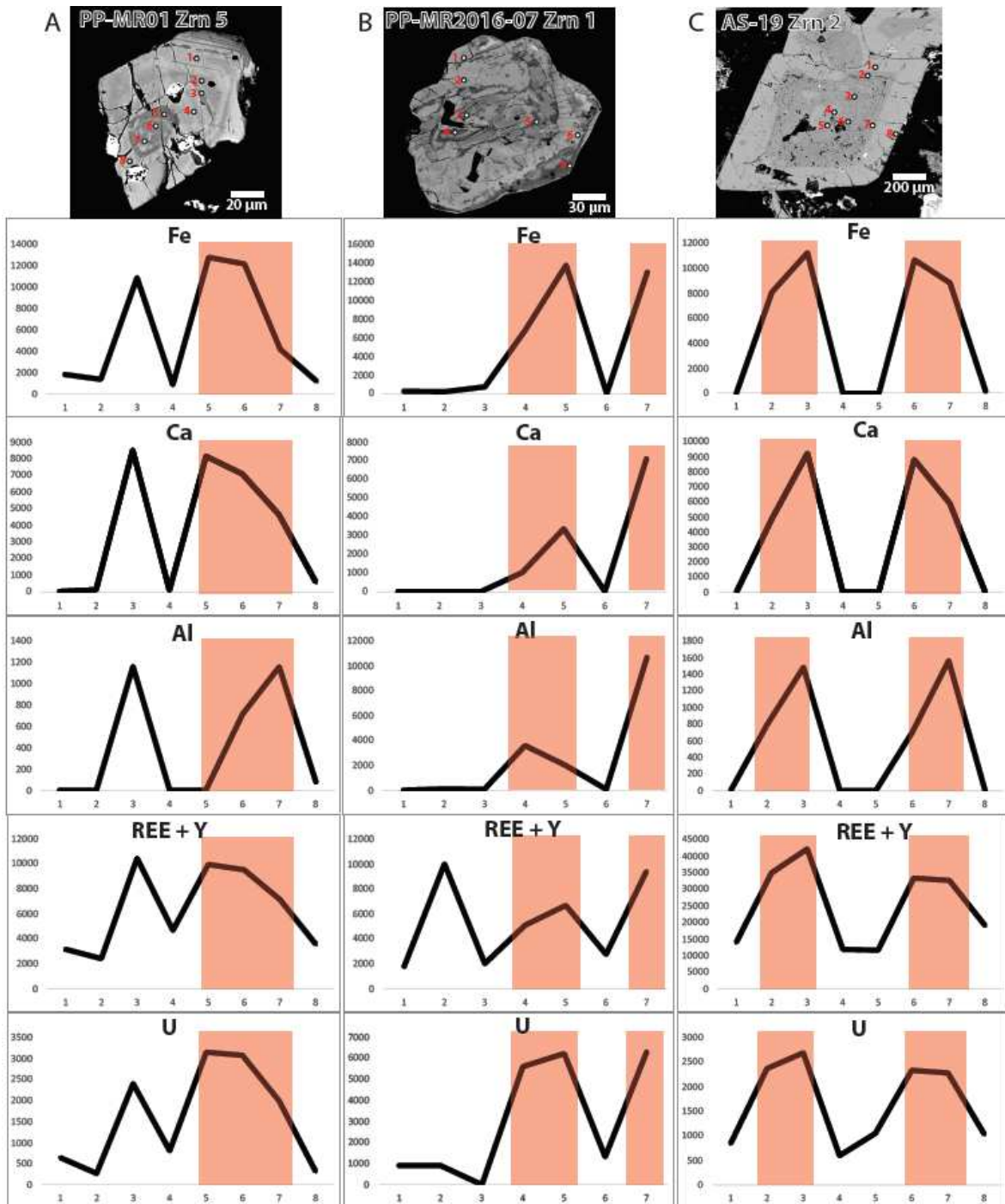


Figure 2.46: Zircon traverse plots illustrating variation in Iron, Ca, Al, (REE+Y), and U within (A) Pikes Peak granite (type 1A), (B) Mount Rosa granite patchy zircon (type 1C), and (C) type-(I) pegmatite zircon (type 1A). Areas of metamictization are highlighted in red and display elevated concentrations relative to the healthy zones.

Whole rock chemical data indicates the MRG is peralkaline (Barker et al., 1975; Smith et al., 1999; Persson, 2017). Until recently, researchers believed the MRG to be a separate peralkaline magmatic body unrelated to the peraluminous rock units of the MRC (Gross, 1962; Gross and Henirich, 1965; Smith et al., 1999). Persson (2017) challenged this statement, suggesting the MRG was in fact co-magmatic with the PPG based both on field and chemical data. Persson (2017) describes the contacts between the MRG and PPG as sometimes sharp but in other places as wavy and irregular, and even gradational. In addition to the irregular boundaries, variations in mineral modal abundance, grain size and appearance of mafic minerals (mainly arfvedsonite) within the MRG are noticeable. Finally, the MRG is described to occur in “sleet-like layers”, suggesting multiple pulses of magmatic emplacement over time. Whole rock geochemical data collected by Persson (2017) displays low Ca concentration (0.27 wt%) and undetectable P, both characteristics of a late-stage melt fraction rather than a separate granitic body (Thomas et al., 2006). In addition, zircon age dates of 1088.3 ± 6.8 (Premo, per. comm.) are similar to the PPG age as well as similar ϵNd values between rock units (Persson, 2017; Premo, pers. Comm.).

Current research regarding the formation of peralkaline melts include:

- (I) Markl et al. (2010) suggest the formation of peralkaline melts is largely controlled by a metasomatic event prior to magmatic generation, resulting in sodium and/or potassium enrichment of the mantle melt. The enrichment in these elements controls redox reactions, therefore controlling mineralogic assemblages based on silica-undersaturated or silica-oversaturated compositions in an attempt to reach equilibrium. In addition to redox reactions, they attribute oxygen fugacity to be a controlling factor, which is correlated to the Na/K and (Na+K)/Al ratio of the original melt.
- (II) Thomas et al. (2006) propose that the generation of a peralkaline melts originates from a peraluminous melt initially enriched in F- and H₂O. Through fractional crystallization processes, this melt is being further enriched in these volatiles and conjugate melt fractions form at saturation: one melt being peraluminous while the other being peralkaline in character. Each melt continues to evolve separately since physical and chemical properties between the two melts are drastically different. As a result, the more evolved, volatile-rich peralkaline melt might continue to evolve to second and third order fractions, continuing to increase in peralkalinity with each fraction.

Studying melt inclusions in S-type Li-mica granitic pegmatites in Germany, Thomas et al. (2006) suggest a peralkaline melt can form through fractional crystallization, followed by melt-melt immiscibility

processes from a peraluminous magma body rich in H₂O and F-. They suggest that through fractional crystallization processes, the original peraluminous melt ($\text{Al}_2\text{O}_3 > (\text{Na}_2\text{O} + \text{K}_2\text{O} + \text{CaO})$) becomes progressively more enriched in incompatible elements such as H₂O, F, Cl and B until complete saturation. At this point, the once homogeneous melt splits into two through immiscibility processes, one remaining peraluminous while the other being peralkaline ($\text{Al}_2\text{O}_3 < (\text{Na}_2\text{O} + \text{K}_2\text{O})$). The resulting peralkaline melt (here: MRG) is therefore highly enriched in H₂O and F allowing for additional extraction of REE and HFSE from the peraluminous melt due to their tendency to complex with these elements (Thomas et al., 2006; Van Lichtenvelde et al., 2010). This proposed process might explain the noticeable increase in HFSE and REE concentrations in both sieve (type 1B) and patchy (type 1C) MRG zircons relative to the peraluminous PPG zircons (Fig. 2.36). Once the immiscibility between peraluminous and peralkaline melts within the magma body occurs, a dissimilarity in both physical (density and viscosity) and chemical (compositions and volatile concentration) properties ensures their separation (Thomas et al., 2005; 2006).

The MRG displays irregular and wavy, sometimes gradational boundaries between optically different granitic rocks with slightly different mineralogy and vastly different mineral modal abundances; textures that suggest a magma mingling processes (Fig. 2.47). In these zones, grain sizes generally vary between fine and coarse grained. The more coarse grained granite oftentimes is hosted with a higher modal abundance of Na-Fe amphibole while the finer grained MRG displays a lower modal abundance of Na-Fe amphibole. In addition to the higher concentration of Na-Fe amphibole, in some cases these coarse grained pockets contain astrophyllite (Fig. 2.47D). The two different zircon types that were found in the MRG, (type 1B (sieve textured) and type 1C (patchy)) do not co-occur within the same sample, but are exclusive and from different sample localities. When compared to biotite chemical data collected by Persson (2017), it is noteworthy that the biotite chemistry in samples with sieve textured type 1B zircons is different (lower in Al, F and Mn content than the chemistry of biotite in samples that show patchy type 1C zircons (higher Al content, Mn, and F content; Fig. 2.48).

In addition to this immiscibility process that leads to the separation of a peraluminous melt and a peralkaline melt, second-order separations processes can occur (Thomas et al., 2006). This newly separated peralkaline melt is thought not to be in equilibrium leading to a second stage immiscibility process (Thomas et al., 2006). This means that the volatile-rich peralkaline melt might continue to evolve to second and third order fractions, continuing to increase in peralkalinity with each fraction, leading to the formation of a more evolved peralkaline melt with increasing concentrations of volatiles. Continued fractional crystallization would further concentrate H₂O, F, and other incompatible elements (Thomas et

al., 2005). Type 1B (sieved zircons) display a slightly lower concentration of REE and HFSE in their crystallographic structures (Fig. 2.36) relative to type 1C (patchy) zircons and do not contain any HFSE or REE-bearing mineral inclusions while type 1C (patchy) zircons host an abundance of these inclusions. These observations combined with biotite chemical data suggest the type 1B (sieved) zircons crystallized in the less evolved peralkaline melt and the type 1C (patchy) zircons crystallized in the more evolved peralkaline melt. Both zircons display as euhedral, and were one of the first minerals to crystallize. Sieve textured type 1B zircons occur in samples with the biotite endmember annite, which shows low F concentrations. Patchy zircons (type 1C) only occur in samples with the biotite endmember siderophyllite with high F content, and is commonly associated with astrophyllite, which is lacking in samples with sieve textured type 1B zircons. Marks et al. (2006) describe astrophyllite as a key mineral during increasing peralkalinity observed in various complexes (i.e. Ilimaussaq, Greenland, Puklen, Greenland, and Mont Saint Hilaire, Canada) and its presence suggests a highly evolved peralkaline melt trending towards an agpaitic character.

The patchy zoning texture reported in both sieve and patchy zircons of the MRG is similar to a texture reported for zircons of the peraluminous Monte Capanne pluton, Italy (Gagnevin et al., 2010). They attribute the texture to a disequilibrium, magma mixing process during zircon growth at high temperatures ($>700^{\circ}\text{C}$). The patchy zoned textures of both MRG zircons could be due to disequilibrium during second-order immiscibility and melt separation processes. While changes in density and volatile content between the two peralkaline bodies is present, it would likely not be nearly as extreme as the differences (both chemical and physical) observed in the peraluminous PPG versus the peralkaline MRG. As a result, melt separation during the second stage immiscibility processes is not as effective as during the initial separation of a peralkaline from a peraluminous melt. This causes abundant magma mingling and patchy outcrop features in the field.

The mafic dike (type 1C) zircons are the youngest of the type 1C zircons throughout the MRC. Similar to the granitic dikes and the MRG type 1C zircons, these zircons are rich in inclusions (Fig. 2.25). Chemically, these zircons display an elevated REE, Hf, Fe and Ca content compared to other type 1C zircons (granitic dike and MRG (patchy) zircons; Figs. 2.36 and 2.40). Zoning is generally rare in these zircons, but where present displays as concentric zoning with occasional reactive patches when viewed in CL. Inclusions of REE-bearing minerals such as monazite, xenotime and allanite suggests a typical fractional crystallization sequence, creating a more exsolved REE and HFSE enriched magma. Biotite data suggest that the mafic dike melt was also highly enriched in volatiles such as H_2O , F, and Cl (Persson, 2017). Even

though this seems to support that the melt responsible for crystallizing the MRG and the melt crystallizing the mafic dikes was very similar, textural evidence suggests an overprint event. Unlike other type 1C zircons, inclusions in type 1C zircons from the mafic dikes (Fig. 2.25) display as subhedral to anhedral. Mafic dike type 1C zircons show U and Th values below the detection limit, another feature similar to the later stage hydrous zircons of Thor Lake (Hoshino et al., 2012). Additional support for this late enrichment mechanism is the low EMPA totals (average of 93.92 wt%; Table 2.3), which Hoshino et al. (2012) describe as oftentimes close to or below 90 wt% due to the presence of hydrous species like H_2O undetectable by the EMPA.

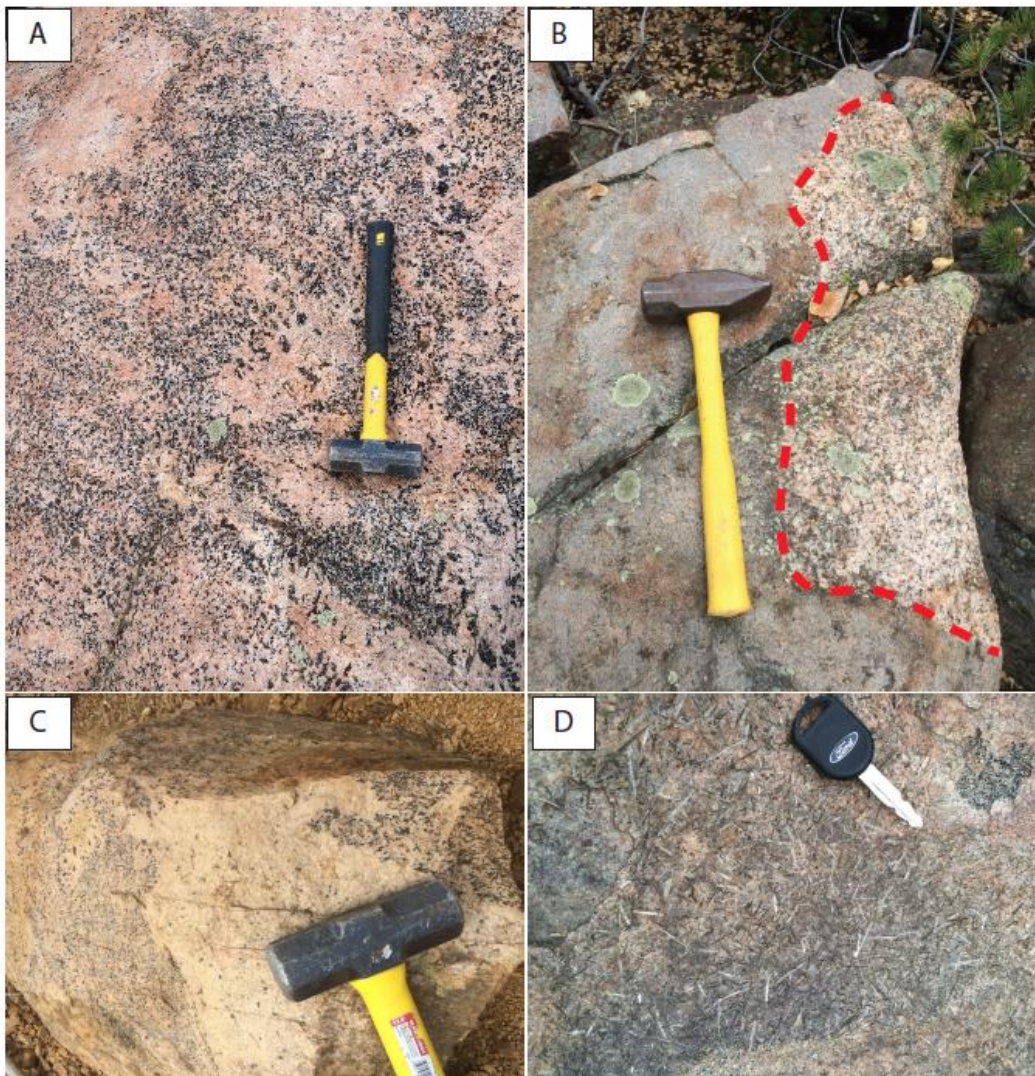


Figure 2.47: Field images of Mount Rosa Granite (MRG) heterogeneity. (A) Heterogeneous Na-amphibole distribution at the center of the granitic body (B) Coarse grained MRG situated within fine grained MRG (C) Heterogeneous mineral distribution textures, (D) Astrophyllite rich pocket in MRG within MRG without any astrophyllite. Images from Persson, 2017.

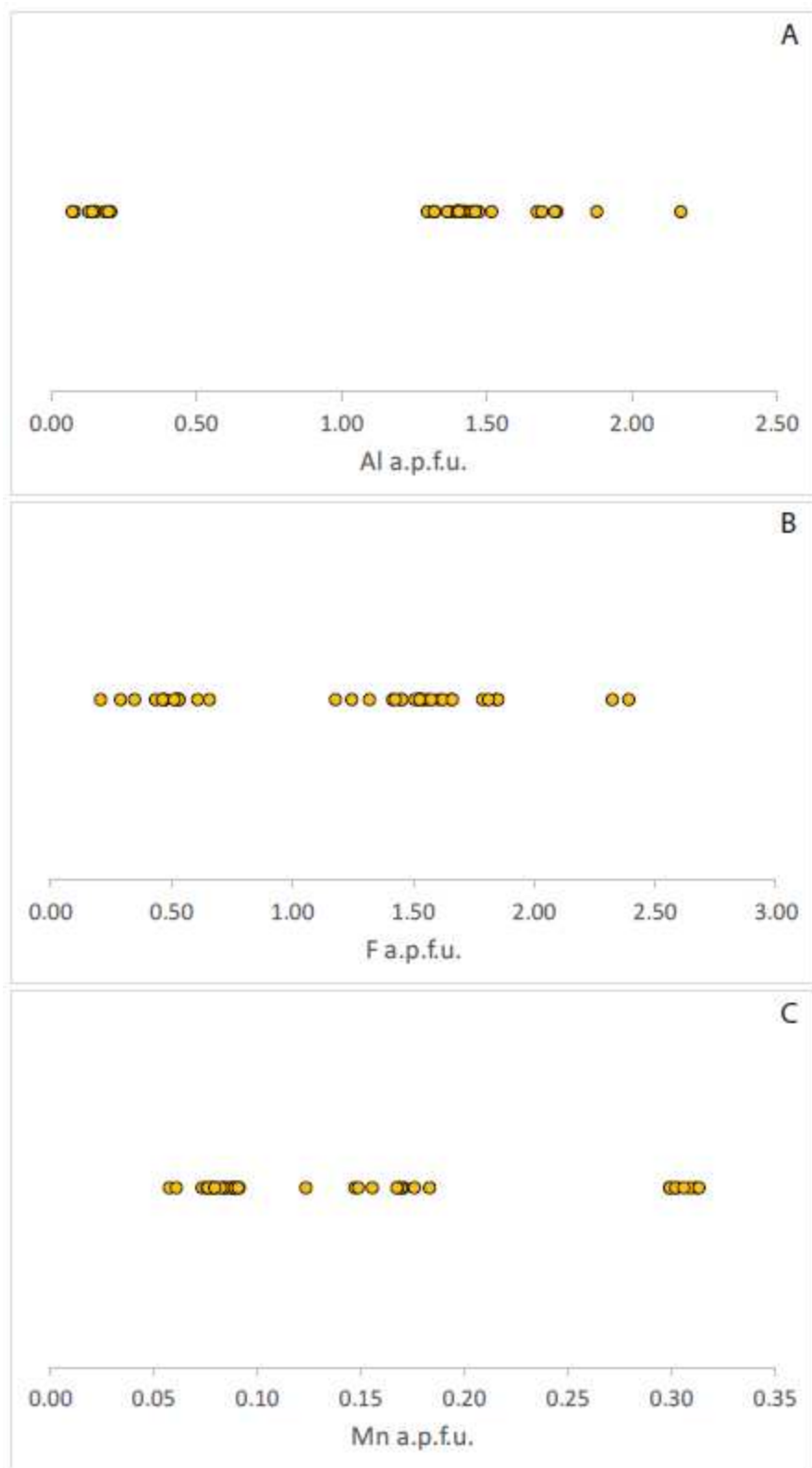


Figure 2.48: EMPA biotite data collected from Persson (2017). Two distinct groups can be observed in biotite analyzed from the MRG for elements (A) Al, (B) F, and (C) Mn (see text).

Type-(I) pegmatite (type 1A) zircons fall back into the category of type 1A zircons, which display as euhedral, concentric zoned zircons with minimal inclusions other than within the metamict layers. Mineralogically, these type-(I) pegmatites present as residual melt with large euhedral crystals growing inward from the contacts, and display strong compositional zoning (Gross and Heinrich, 1966; Persson, 2017). Zircon crystals along with other minerals are large, suggesting a slower cooling processes in a viscous fluid (London, 2008). Undisturbed concentric zoning indicates that the melt was in equilibrium, unlike during the formation of units hosting type 1B and type 1C zircons, which seem to be indicative of disequilibrium processes (Gagnevin et al., 2010). Chemically, most pegmatites of the MRC are classified as niobium-yttrium-fluorine(NYF)-type pegmatites, which is defined by an enrichment in Ti, Y, Sc, REE, Zr, U, Th, F and $Nb > Ta$ (Martin and De Vito, 2005; Černý and Ercit, 2005). The zircon chemistry strongly reflects this classification. Chemically, the zircons display a bimodal distribution for all elements, where extreme enrichment is observed in the metamict zones (Fig. 2.45C). Enrichment in REE (average of 1.97 wt%; table 2.3) and HFSE is also characteristic of the healthy zones of these zircons relative to all older units (PPG, Fayalite-bearing Quartz Syenite, granitic dikes, MRG, and mafic dikes; Fig. 2.36). Where metamictization occurs, REE and HFSE- bearing phases present as subhedral to anhedral inclusions, similar to the texture observed in the mafic dikes. Type 1A zircons are observed throughout all type-(I) pegmatites, displaying as a minor mineral near the pegmatite rim and transitioning to arguably a major mineral in the core, suggesting an abundance and enrichment of Zr in the system during crystallization.

Type-(II) pegmatites contain two individual zircon generations (Type 2 and type 3). Type-(II) pegmatites can be well zoned to poorly zoned and can contain an abundance of unusual F-bearing minerals (e.g. cryolite; Persson, 2017). Zircon chemical data from a transect of a type-(II) pegmatite was collected in order to better understand the evolution and formation of these complex pegmatites (Fig. 2.49A). Type 2 zircons are volumetrically minor and mainly concentrated near the rim of the pegmatite with a minor abundance in the interior portion of the pegmatite. The core of the pegmatite is lacking type 2 zircons. Type 2 zircons are interpreted to be primary magmatic zircons that were intensely overprinted by hydrothermal fluids due to their complex textural appearance and extreme REE and HFSE variability (Schaltegger, 2007). The complex patchy zoning textures observed in these zircons is interpreted to be overprint textures as secondary domains cut along the primary growth zones (Schaltegger, 2007). Hydrothermal type 3 zircons are very abundant in the sampled type-(II) pegmatite, and show much higher concentrations in incompatible elements compared to all other zircons within the complex. The REE values commonly make up between 2-3 wt%, Hf between 3-4 wt%, Th around 1 wt% and Fe just under 1 wt% (Table 2.3, Fig. 2.45). High concentrations in other elements such as Al are commonly described in

hydrothermal zircons (Rubin et al., 1993), which is also observed in hydrothermal type 3 zircons from the MRC. On the contrary, elevated U contents are commonly reported for hydrothermal zircons of the Sierra Blanca Peaks, Texas (Rubin et al., 1989; 1993) and Thor Lake, Canada (Sheard et al., 2012), which is not present in hydrothermal zircons from the MRC. However, hydrothermal zircons from Strange Lake, Canada are characterized by low U and Th contents (Gysi et al., 2016). Hydrothermal type 3 zircons from the MRC display perfect concentric zoning if crystallized as individual crystals or no zoning at all if crystallized in vein-like network-styles hosted in fluorite and quartz. The mineral association between hydrothermal type 3 zircons and fluorite and quartz has also been observed in other comparable igneous complexes such as Strange Lake, Canada (Gysi et al., 2016), Thor Lake, Canada (Hoshino et al., 2012; Sheard et al., 2012), and the Sierra Blanca Peaks, Texas (Rubin et al., 1993). The following characteristics can be observed from plotting trace element concentrations along a transect from the rim to the interior and core of the type-(II) pegmatite. The most incompatible elements (Hf, Al, Fe, Sn, and Mn) display increasing concentrations towards the core of the pegmatite (Fig. 2.49B). Persson (2017) investigated the biotite chemistry of a similar type-(II) pegmatite, and was able to show that fluorine concentration in biotite increases dramatically from the rim to the core of the pegmatite (Fig. 2.49C) and attributes this to constitutional zone refining.

Type-(I) pegmatites are mineralogically fairly simple, consisting of minerals generally seen in the MRG, but with higher REE and HFSE concentrations in the type 1A (type-(I) pegmatite) zircons relative to the type 1B and type 1C (MRG) zircons. Type-(II) pegmatites are mineralogically more complex, and are zoned. These pegmatites also display a similar mineralogy to the MRG, but in addition to a high abundance of fluorine, REE and HFSE-bearing minerals such as cryolite (Na_3AlF_6) and bastnasite ($\text{Ce}(\text{CO}_3)\text{F}$) occur. The presence of these minerals (with increasing concentrations towards the core) indicates a melt rich in volatiles, fluorine, REE, and HFSE. Both pegmatites are made up of minerals strikingly similar to the MRG, however whole rock data paired with biotite and zircon geochemistry suggests that the type-(II) pegmatites are genetically related to the more evolved MRG whereas the type-(I) pegmatites represent the remaining melt of the less evolved MRG. Thomas et al. (2006) report the most evolved melt, in this case the type-(II) pegmatites, oftentimes isolates and occur in clusters, typically congregating along the edges of a particular complex. In the MRC, the final amounts of melt that surface as type-(II) pegmatites occur as groups across the complex in the southeast corner of the PPB, rather than widely distributed like type-(I) pegmatites.

The transition from magmatic to hydrothermal can be nicely observed in type-(II) pegmatites. Magmatic type 2 zircons dominantly occur at the rim and transition zone of the pegmatite, whereas hydrothermal zircons are highly concentrated in the core (up to 60 modal %). Historically, zirconium was thought to be an immobile element (Finlow-Bates and Stumpfl, 1981) and only in more recent years have studies discovered that Zr and other HFSEs can be transported in alkali-rich (F and Cl) aqueous fluids (Rubin et al., 1989; Sheard et al., 2012; Gysi et al., 2016). The presence of F and other alkalis contributes to depolymerization, lower viscosity, and a decrease in solidus temperature, which aids in the transport and concentration of Zr, other HFSEs and REEs (Gysi et al., 2016). High modal abundance of fluoride and the presence of cryolite, bastnasite, and parisite paired with elevated F and Cl concentration in biotite grains from the core of a type-(II) pegmatite analyzed by Persson (2017) support this idea. Fluorine-rich fluids responsible for Zr transport and precipitation have been reported from the peraluminous Sierra Blanca Peaks, Texas, (Rubin et al., 1989; 1993) and the peralkaline Strange Lake complex, Canada, (Gysi et al., 2016). This final hydrothermal event seemed to have altered the primary magmatic mineralogy (very aggressive acidic fluid due to a high concentration of HF) and leached HFSEs and REEs from the primary metamict zones in the magmatic zircons. Abundant REE concentrations in all rock units in the MRC are a result of late-hydrothermal overprint depositing secondary REE minerals.

Hydrothermal event in the MRC

High REE concentration in whole rock data from all rock units of the MRC are largely contributed to a late stage hydrothermal event depositing secondary REE-bearing minerals. Type-(II) pegmatites are interpreted to show the transition from magmatic to hydrothermal in the MRC. According to Persson (2017), hydrothermal processes include albitization, aegirinization, followed by Ca-F metasomatism. Albitization can be both pervasive or minor among rock units in the MRC (Persson, 2017). This process typically alters perthitic feldspar grains to prismatic albite grains along grain edges. Aegirinization has been widely reported from various REE-HFSE deposits such as the peralkaline Strange Lake complex, Canada and the peralkaline Thor Lake complex, Canada (Salvi and Williams-Jones, 1996, Hoshino et al., 2012, Sheard et al., 2012; Gysi et al., 2016). This alteration fluid attacks primary magmatic biotite and amphibole and is capable of leaching and transporting REE and HFSE (Salvi and Williams-Jones, 1996). The dissolution of biotite buffers the highly acidic fluid and development of pore spaces provided an area for Ca-F metasomatic fluids to infiltrate and subsequently deposit REE-bearing minerals in pore spaces. In addition to the dissolution of biotite grains, this fluid likely attacked the more unstable metamict zones of the type 1A and 1C zircons of the PPG, MRG, and type-(I) pegmatites, providing an additional REE and HFSE source.

The metamict zones are notably more prone to dissolution due to crystal lattice defects and radioactive decay processes (Nasdala et al., 2001). A similar process is described by Rubin et al., (1993) in which the fluid was acidic enough to break down aegirine and arfvedsonite (hosting zircon), allowing for the release of Zr, but the zircons themselves were only moderately attacked at the weaker metamict zones.

Rare earth element bearing minerals are generally observed as secondary minerals deposited during Ca-F metasomatism. Secondary REE minerals include bastnasite (Y), allanite (Y), parasite (Ce), which usually present as replacement textures in biotite and amphibole or in crosscutting fluorite rich veins in type-(II) pegmatites. Ca-F metasomatism is a process largely attributed to transporting and concentrating HFSE and REE (Rubin et al., 1993; Salvi and Williams-Jones, 1996; Hoshino et al., 2012; Sheard et al., 2012; Gysi et al., 2016). Late stage fluorine-rich fluids form due to the incompatible character of fluorine in a granitic magma, forcing the fluorine to partition into the co-existing fluid (Sheard et al., 2012). Complexation relationships create HF, making this an aggressive and acidic fluid (Rubin et al., 1993; Salvi and Williams-Jones, 1996). During aegirinization (biotite and amphibole dissolution), the late stage hydrothermal fluids are being further enriched in F and Cl. Gysi and Williams-Jones (2013) suggest the transport of REE is strongly dependent on complexation with Cl whereas Zr transportation is dependent on complexation with F. Persson (2017) reported elevated F and Cl concentrations in biotite from the core of a type-(II) pegmatite, suggesting high F and Cl concentrations in the late stage magmatic to hydrothermal fluid transition (Fig. 2.49C).

The source of the hydrothermal fluid is unknown, but thought to be a combination of magmatic and meteoric waters. In the Sierra Blanca Peaks, researchers propose that the hydrothermal fluid was sourced from meteoric water based on fluid inclusion salinities (Rubin et al., 1993). The peralkaline Thor Lake complex displays elevated HFSE and REE in the nepheline-aegirine syenite, which suggests that with time, fractional crystallization of the melt produced elevated alkali contents in an aqueous fluid, therefore increasing solubility of REE and HFSE and forming alkali complexes for transportation (Sheard et al., 2012). In the peralkaline Strange Lake, Canada complex, Gysi et al. (2016) propose fluid exsolution from a fractionating magma combined with acidic alteration to be responsible for mobilization of REEs and HFSEs throughout the pegmatites and surrounding host rocks. In addition to fluid source, fluid temperature has been widely discussed in these deposits as a controlling factor for mobilization (Gysi et al., 2016). Studies have indicated fluids rich in HF successfully dissolve zircons in temperatures as low as 200°C and allow for its complexation with F for transportation (Sheard et al., 2012). Additionally, lower temperatures support

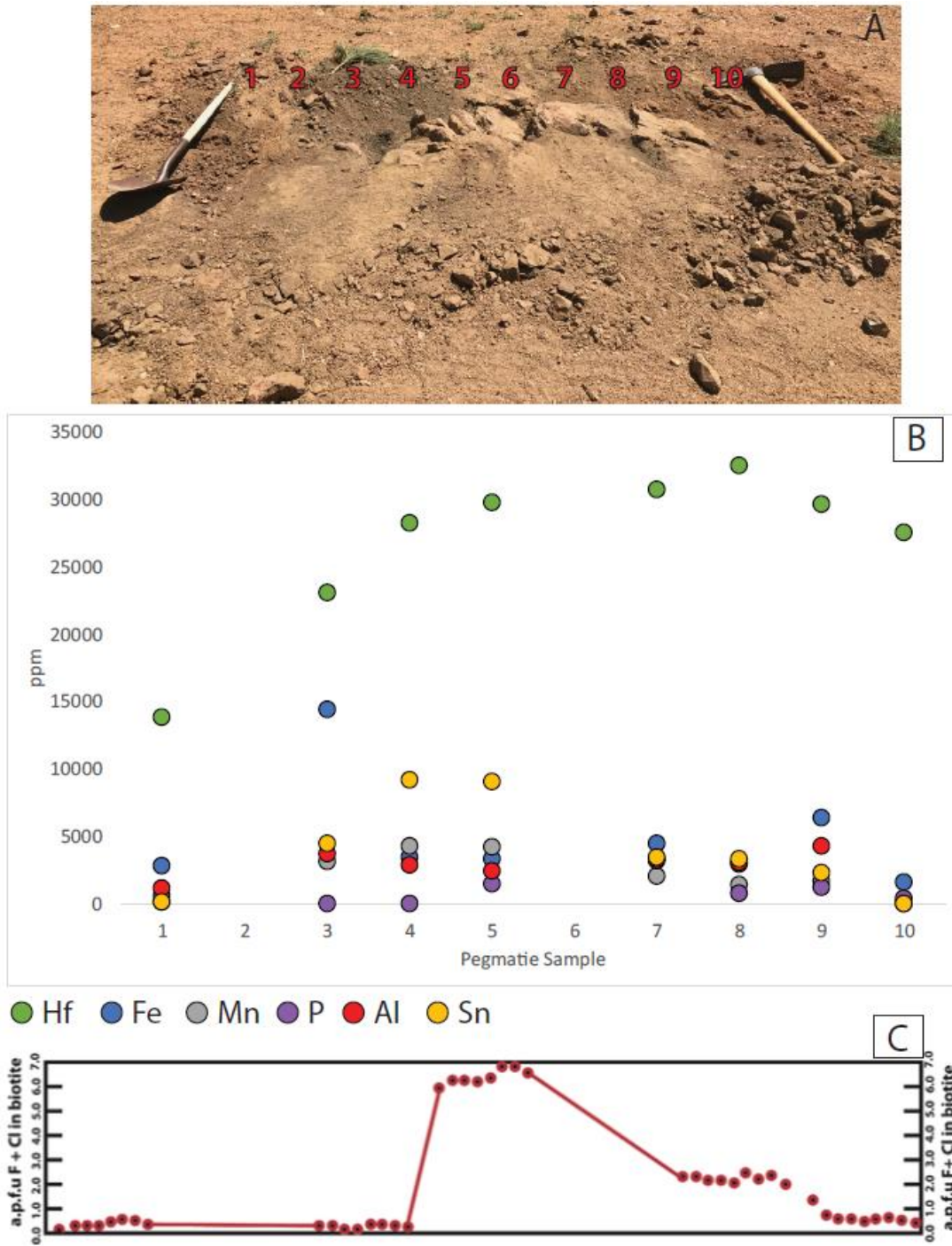


Figure 2.49: Type-(II) pegmatite transect. (A) Image of exposed type-(II) pegmatite with approximate sample locations, (B) mean element concentrations from zircons analyzed in each sample displaying a general enrichment towards the core (samples 2 and 6 were not analyzed), (C) fluorine content in biotite from a similar type-(II) pegmatite displaying enrichment of F and Cl in the core (Persson, 2017).

transport of the HFSE continued as the zircon solubility whereas REE-bearing minerals such as bastnasite are more soluble in higher temperatures (Gysi and Williams-Jones, 2015). The lack of REE-bearing minerals co-crystallizing with the hydrothermal zircons suggest the REEs were deposited first, while the metasomatic fluids were still warmer. Zircon dissolution and transportation increased as the fluid cooled since these display retrograde solubility at decreasing temperatures, concentrating these minerals in the type-(II) pegmatites. London (2008) explains the formation pegmatite textures begins with the crystallization of anhydrous minerals along the wall zone, which accumulates fluxed elements in the core through constitutional zone refining processes, which helps to explain the exponential increase in concentration of these elements in the core of the type-(II) pegmatite.

2.7 Conclusions

The MRC is suggested to evolve from an enriched peraluminous A-type granite to a peralkaline melt through fractional crystallization, eventually leading to melt-melt immiscibility and melt separation through density and viscosity differences. The volatiles, REEs and HFSEs are concentrated in the newly separated peralkaline melt, undergoing a second-order melt-melt immiscibility process. The existence of two peralkaline melts, one more evolved than the other is supported by textural and mineralogical relationships observed in the MRG, biotite chemical data, and zircon morphology and chemistry. Two types of pegmatites are the direct result of this second-order immiscibility process: type-(I) pegmatites form from residual, less evolved MRG melt while the type-(II) pegmatites form from the more evolved melt, highly enriched in volatiles, F, REEs, and HFSEs. Based on the collected data, the evolution of the MRC (Fig. 2.50) can be described as follows:

- The peraluminous A-type PPG was emplaced during the Berthoud Orogeny (1.4 Ga). Due to crustal contamination during ascent and emplacement, this melt was enriched in volatiles, alkalis, and HFSEs and REEs. Through fractional crystallization of the hypersolvus PPG, this peraluminous melt becomes saturated in incompatible elements and volatiles, and separates into two (one peraluminous $((\text{Na}_2\text{O}+\text{K}_2\text{O}+\text{CaO})/\text{Al}_2\text{O}_3 < 1.0)$ and one peralkaline $((\text{Na}_2\text{O}+\text{K}_2\text{O})/\text{Al}_2\text{O}_3 > 1.0)$ conjugate melts. Once separated, each melt continues to evolve independently, with little interaction (Fig. 2.50 Stage 1).
- The more evolved peralkaline melt, rich in volatiles and incompatible elements is not in equilibrium and unstable in nature, causing a second-order immiscibility process, producing into two peralkaline conjugate melts. Sieve texture zircons (type 1B) are interpreted to have crystallized in the less evolved melt (higher aluminum saturation index), co-existing with the

annite biotite endmember. The patchy (type 1C) zircons are interpreted to have crystallized from the more evolved melt (lower aluminum saturation index), co-existing with the F-rich, siderophyllite biotite endmember as well as astrophyllite (Fig. 2.50 Stage 2).

- Type-(I) pegmatites are interpreted to represent the remaining melt of the less evolved MRG magma (I) whereas type-(II) pegmatites are thought to represent the transition from magmatic (last batch of melt that was responsible for the formation of the more evolved MRG magma (II) to hydrothermal (Fig. 2.50 Stage 2).
- During aegirinization, acidic fluids rich in HF dissolve primary magmatic biotite and amphibole. Additionally, metamict areas of the magmatic zircons are attacked, releasing Zr as well as other REE-HFSE due to crystal lattice instability. During this process, the highly aggressive HF-bearing fluid (rich in F, Cl, REEs and HFSEs) is being buffered (Fig. 2.50 Stage 3), allowing for Ca-F metasomatism to occur.
- Ca-F metasomatism: As the fluid begins to cool and the fluid becomes less acidic due to biotite and amphibole dissolution processes, REE-F bearing minerals replace former biotite grains. Zirconium and other HFSE continue to stay in solution due to retrograde solubility characteristics, eventually depositing fluorite, destabilizing Zr-F complexes leading to the formation of complex hydrothermal zircon veinlets, fluorite and hydrothermal quartz (Fig 2.50. Stage 3).

Figure 2.50: Simplified diagram illustrating the proposed processes responsible for the formation of the MRC. Stage 1 displays a peraluminous melt with quartz, biotite and feldspar crystallizing (PPG). Incompatibles like alkalis, volatiles, HFSE, and REE remain in the melt, forming highly enriched melt pockets. This melt is not in equilibrium and unstable in nature, leading to the formation of two conjugate melts: a peraluminous and a peralkaline melt. Stage 2: the peralkaline melt (which is not in equilibrium) undergoes second-order melt separation forming two discrete peralkaline MRG melts, with one being more enriched in volatiles, alkalis, REEs, and HFSEs (more evolved) than the other. The more evolved melt corresponds to pockets of astrophyllite with patchy type 1C zircon and F-rich siderophyllite. The surrounding less evolved peralkaline MRG does not contain astrophyllite, is host to sieve textured type 1B zircons, and contains F-poor annite instead of siderophyllite. Field evidence suggests abundant magma mingling or incomplete separation of two co-existing peralkaline MRG melts. Type-(I) pegmatites are thought to represent the last remaining melt batch after crystallizing the less evolved MRG unit, whereas type-(II) pegmatites are thought to represent the last melt of the more evolved (more volatile rich) MRG unit and also shows the transition from magmatic to hydrothermal. Biotite and zircon chemical data suggest further enrichment of incompatible elements such as Hf, Sn, Mn, and F during late stage processes, leading to stage 3, a hydrothermal event. Stage 3 is characterized by aegirization and Ca-F metasomatism during which biotite and amphibole are being dissolved (releasing large amounts of Zr, REEs, and other HFSEs (from biotite and zircon inclusions) and replaced by secondary REE-bearing minerals such as bastnasite, parisite, and yttrifluorite.

CHAPTER 3: CONCLUSIONS AND OUTLOOK

Today, some processes that are responsible for REE and HFSE enrichment in granitic bodies and their remobilization remain rather inexplicable. While differences among deposits suggests multiple processes can contribute to REE and HFSE enrichment, years of research across many localities exhibit many resemblances. In the case of the MRC, evidence has led to the suggestion of melt-melt immiscibility through fractional crystallization and exsolution processes. These processes allow the complex to evolve from a peraluminous melt to a more volatile rich, peralkaline system.

3.1 Conclusions

The diverse array of peraluminous to peralkaline rock units throughout the MRC and enrichment in REEs and HFSEs relative to typical A-type magmatic suites remains perplexing even after detailing changes in zircon textures and chemistry for this study. Similar to conclusions drawn by Persson (2017), this study concludes the complex evolved from the parental PPG melt, initially enriched in REEs, HFSEs, alkalis and volatiles through crustal contamination prior to emplacement. This contamination provided incompatible elements to be incorporated into the zircon's structure early on in the magmatic evolution, creating an enriched A-type granite (PPG) starting at the oldest rock units.

Collected major, minor and trace element data from zircons from all rock units suggest a co-magmatic relationship among all rock units rather than separate bodies due to the gradual increase in REE and HFSE concentrations towards younger rock units. In order to develop a peralkaline melt from a peraluminous melt, melt-melt immiscibility processes through fractional crystallization is suggested. Melt inclusions studied by Thomas et al. (2006) implied a similar transition from peraluminous to peralkaline melt-melt immiscibility processes. The resulting peralkaline melt is thought to not be in equilibrium, causing it to undergo a second-stage immiscibility event. This process can explain observed field relationships between two similar peralkaline varieties of the MRG, which are interpreted to represent magma mingling. Late magmatic and hydrothermal events are responsible for wide-spread redistribution of REEs and their occurrence as secondary REE-F minerals replacing biotite.

Following the conclusion of this study, it is clear the MRC is complex and has plenty of room for additional work to better understand its evolution from a magmatic to a hydrothermal system as well as its relationship to the Pikes Peak batholith. While zircon is a valuable mineral to use for magmatic changes, melt inclusion data on many of these rock units can provide additional information regarding magmatic chemistry that zircon cannot provide. Thomas et al. (2006) mentions the most highly reactive melts remain

highly reactive until equilibrium is obtained, so oftentimes the trace of this highly evolved magma can only be captured in melt inclusions. Analysis of these melt inclusions not only will help constrain magma chemistry of each rock unit, it might also reveal additional orders of immiscibility that have yet to be uncovered. Unfortunately, melt inclusions can only be studied in magmatic rocks (Thomas et al. 2006) and will not provide additional information on the hydrothermal alteration processes. Further understanding the relationship between rock units within the complex could be achieved using Ti in zircon thermometry in order to better understand temperature variations (Fu, et al., 2008). Additionally, U-Pb dating can be done on zircons. U-Pb dating may not give meaningful results due to the old age and the closeness in dates between the PPG (1.08 Ga) and MRG (1.04 Ga). Since the complex is interpreted to be relatively similar in age, the error bars of individual age dates might be larger than the age difference of different rock units within the MRG.

Further research investigating the peralkaline rocks of the MRG should be done in order to better understand the evolution of this unit. The peralkaline MRG is composed of at least two discrete peralkaline rock units, which seem to be variably evolved. The distribution of these two (or more) peralkaline sub-units could be mapped and sampled to further understand the distribution and melt evolution in the peralkaline systems. This can be further applied to better understand trends between miaskitic to agpaitic rocks, similar to trends documented by Marks et al. (2011). Other complexes within the Pikes Peak batholith should be evaluated when attempting to better understand the peralkalinity, such as the Lake George ring complex. This area displays a sharp transition between sodic and potassic plutons, and a better understanding of that complex could shed light on the peralkalinity of the MRG.

REFERENCES

- Aja, S.U., Wood, S.A. and Williams-Jones, A.E., 1995, The Aqueous Geochemistry of Zr and the Solubility of Some Zr-Bearing Minerals: *Applied Geochemistry*, v. 10, p. 603-620.
- Anderson, J.L., 1983, Proterozoic Anorogenic Granite Plutonism of North America: *Geological Society of America Memoir 161*, p. 133-154.
- Ayers, J.C., Zhang, L., Luo, Y., and Peters, T.J., 2012, Zircon Solubility in Alkaline Aqueous Fluids at Upper Crustal Conditions: *Geochimica et Cosmochimica Acta*, v. 96, p. 18-28.
- Barker, F., Wones, D.R., Sharp, W.N., and Desborough, G.A., 1975, The Pikes Peak Batholith, Colorado Front Range, and a Model for the Origin of the Gabbro-Anorthosite-Syenite-Potassic Granite Suite: *Precambrian Research*, v.2, p. 97-160.
- Belousova, E.A., Griffin, W.L., and Pearson, N.J., 1998, Trace Element Composition and Cathodoluminescence Properties of southern African Kimberlitic Zircons: *Mineral Magazine*, v. 62, p. 355-366.
- Černý, P. and Ercit, S.T., 2005, The Classification of Granitic Pegmatites Revisited: *The Canadian Mineralogist*, v. 43, p. 2005-2025.
- Corfu, F., Hanchar, J.M., Hoskin, P.W.O., and Kinny, P., 2003, Atlas of Zircon Textures: *Reviews in Mineralogy and Geochemistry, Mineralogical Society of America and Geochemical Society*, v. 53, p. 469-500.
- Cross, W. and Hillebrand, W., 1882, Notes on Some Interesting Minerals Occurring Near Pikes Peak, Colorado: *American Journal of Science*, v. 24, p. 281-286.
- De Hoog, J. C. M., Lissenberg, C. J., Brooker, R. A., Hinton, R., Trail, D., and Hellebrand, E., 2014, Hydrogen incorporation and charge balance in natural zircon: *Geochimica et Cosmochimica Acta*, v. 141, p. 472-486.
- Finlowbates, T. and Stumpfl, E.F., 1981, The Behavior or So-Called Immobile Elements in Hydrothermally Altered Rocks Associated with Volcanogenic Submarine-Exhalative Ore-Deposits: *Mineralium Desposita*, v. 16, p. 319-328.
- Foord, E.E., 1982, Amazonite-bearing pegmatites of the Lake George Intrusive Center: *Geologic Association of Canada Annual Meeting Field Trip Guidebook*, v. 12, p. 51-56.
- Foord, E.E. and Sharp, W.N., 1984, Zinc and Y-group-bearing Sanaite from St. Peters Dome, and New Data on Senaite from Dattas, Minas Gerais, Brazil: *Mineralogical Magazine*, v. 48, p. 97-106.
- Frost, C.D. and Frost, R.B., 1997, Reduced Rapakivi-type Granites: The Tholeiite Connection: *Geology*, v. 25, n. 7, p. 647-650.
- Fu, B., Page, F.Z., Cavosie, A.J., Fournelle, J., Kita, N.T., Lackey, J.S., Wilde, S.A., and Valley, J.W., 2008, Ti-in-zircon Thermometry: Applications and Limitations: *Contributions to Mineralogy and Petrology*, v. 156, p. 197-215.

- Gagnevin, D., Daly, J.S., and Krons, A., 2010, Zircon Texture and Chemical Composition as a Guide to Magmatic Processes and Mixing in a Granitic Environment and Coeval Volcanic System: *Contributions to Mineralogy and Petrology*, v. 159, p. 579-596.
- Geisler, T., Schaltegger, U., and Tomaschek, F., 2007, Re-equilibration of zircon in aqueous fluids and melts: *Elements*, v. 3, p. 43-50.
- Geological Society of London, 2011, Rare Earth Elements: *The Geological Society of London: A briefing note*, p. 1-13.
- Gross, E.B., 1962, Alkalic Granites and Pegmatites of the Mount Rosa Area, El Paso and Teller Counties, Colorado: Unpublished University of Michigan Ph.D. Thesis, 176 p.
- Gross, E.B. and Heinrich, E.W., 1965, Petrology and Mineralogy of the Mount Rosa Area, El Paso and Teller Counties, Colorado. I. the Granites: *The American Mineralogist*, v. 50, p. 1273-1295.
- Gross, E.B. and Heinrich, E.W., 1966, Petrology and Mineralogy of the Mount Rosa Area, El Paso and Teller Counties, Colorado. II. Pegmatites: *The American Mineralogist*, v. 51, p. 299-322.
- Guitreau, M., Mukasa, S.B., Blichert-Toft, J., and Fahnestock, M.F., 2016, Pikes Peak Batholith (Colorado, USA) Revisited: A SIMS and LA-ICP-MS Study on Zircon U-Pb ages Combined with Solution Hf Isotopic Compositions: *Precambrian Research*, v. 280, p. 179-194.
- Gysi, A.P. and Williams-Jones, A.E., 2013, Hydrothermal Mobilization of Pegmatite-Hosted REE and Zr at Strange Lake, Canada: A reaction Path Model: *Geochimica et Cosmochimica Acta*, v. 122, p. 324-352.
- Gysi, A., Williams-Jones, A.E., and Collins, P., 2016, Lithogeochemical Vectors for Hydrothermal Processes in the Strange Lake Peralkaline Granitic REE-Zr-Nb Deposit: *Economic Geology*, v. 11, p. 1241-1276.
- Heinrich, E.W., 1948, Pegmatites of Eight Mile Park, Freemont County, Colorado: *American Mineralogist*, v. 33, p. 420-448.
- Hoffman, P.F., 1988, United Plates of America, The Birth of a Craton: Early Proterozoic Assembly and Growth of Laurentia: *Annual Review of Earth and Planetary Sciences*, v. 16, p. 543-603.
- Hoshino, M., Kimata, M., Nishidia, N., Shimizu, M., and Akasaka, T., 2010, Crystal Chemistry of Zircon from Granitic Rocks, Japan: Genetic Implication of HREE, U, and Th Enrichment: *Journal of Mineralogy and Geochemistry*, v. 187, n. 2, p. 167-188.
- Hoshino, M., Watanabe, Y., Murakami, H., Kon, Y., and Tsunematsu, M., 2012, Formation Process of Zircon Associated with REE-Fluorocarbonate and Niobium Minerals in the Nechalacho REE Deposit, Thor Lake, Canada: *Resource Geology*, v. 63, n. 1, p. 1-26.
- Hoskin, P.W.O., Kinny, P.D., Wyborn, D., and Chappell, B.W., Identifying Accessory Mineral Saturation During Differentiation in Granitoid Magmas: an Integrated Approach: *Journal of Petrology*, v. 41, n. 9, p. 1365-1396.
- Hoskin, P. W. O. and Schaltegger, U., 2003, The composition of zircon and igneous and metamorphic petrogenesis: *Reviews in Mineralogy and Geochemistry*, v. 53, p. 27-62.

- Hutchinson, R.M., 1976, Granite-tectonics of the Pikes Peak batholith, in Epis, R.C., and Weimer, R.J., eds., *Studies in Colorado field geology: Colorado School of Mines Professional Contributions*, v. 8, p. 32-43.
- Jahns, R.H. and Burnham, C.W., 1969, Experimental studies of pegmatite genesis: I. A model for the derivation and crystallization of granitic pegmatites: *Economic Geology*, v. 64, p. 843-864.
- Karlstrom, K.E. and Bowring, S.A., 1987, Early Proterozoic Assembly of Tectonostratigraphic Terranes in Southwestern North America: *Journal of Geology*, v. 96, p. 561-576.
- Keller, J.W., Siddoway, C.S., Morgan, M.L., Route, E.E., Grizzell, M.T., Sacerdoti, R., and Strevenson, A., 2005, Geologic map of the Manitou Springs 7.5-minute quadrangle, El Paso and Teller counties, Colorado: USGS open-file report 03-19. Denver, CO: U.S. Geological Survey.
- Kirkland, C.L., Smithies, R.H., Taylor, R.J.M., Evans, N., and McDonald, B., 2015, Zircon Th/U Ratios in Magmatic Environs: *Lithos*, v. 212, p. 397-414.
- London, D., 2008, Pegmatites, *The Canadian Mineralogist Special Publication 10*, 347 p.
- London, D., 2009, The origin of Primary Textures in Granitic Pegmatites: *The Canadian Mineralogist*, v. 47, p. 697-724.
- Markl, G., Marks, M.A.W., and Frost, R.B., 2010, One the Controls of Oxygen Figacity in the Generation and Crystallization of Peralkaline Melts: *Journal of Petrology*, v. 51, n. 9, p. 1831-1847.
- Marks, M.A.W., Hettman, K., Schilling, J., Frost, B.R., and Markl, G, 2011, The Mineralogical Diversity of Alkaline Igneous Rocks: Critical Factors for the Transition from Miaskitic to Agpaitic Phase Assemblages: *Journal of Petrology*, v. 52, n. 3, p. 439-455.
- Martin, R.F. and De Vito, C., 2005, The Patterns of Enrichment in Felsic Pegmatites Ultimately Depend on Tectonic Setting: *The Canadian Mineralogist*, v. 43, p. 2027-2048.
- McKenzie, D., 1985, The extraction of magma from the cruse and mantle: *Earth Planet Science Letters*, v. 74, p. 81-91.
- Morgan VI, G.B. and London, D., 1999, Crystallization of the Little Three layered pegmatite-aplite dike, Ramona District, California: *Contributions to Mineralogy and Petrology*, v. 136, p. 310-330.
- Nasdala, L., Irmer, G., and Wolf, D., 1995, The Degree of Metamictization in Zircon: A Raman Spectroscopic Study: *European Journal of Mineralogy*, v. 7, p. 471-478.
- Nasdala, L., Beran, A., Libowitzky, E., and Wolf, D., 2001, The incorporation of hydroxyl groups and molecular water in natural zircon (ZrSiO₄): *American Journal of Science*, v. 301, p. 831-857.
- Pearce, J.A. and Cann, J.R., 1973, Tectonic Setting of Basin Volcanic-Rocks Determined Using Trace-Element Analysis: *Earth Planet Science Letters*, v. 19(2), P. 290-300.

- Pérez-Soba, C., Villaseca, C., González Del Tánago, J., and Nasdala, L., 2007, The Compositions of Zircon in the Peraluminous Hercynian Granites of the Spanish Central System Batholith: *The Canadian Mineralogist*, v. 45, p. 209-527.
- Persson, P.M., 2017, Petrology and Mineralogy of the Mount Rosa Complex, El Paso County, Colorado: Unpublished Colorado School of Mines Masters Thesis.
- Petrella, L., Williams-Jones, A.E., Goutier, J., and Walsh, J., 2014, The Nature and Origin of the Rare Earth Element Mineralization in the Misery Syenitic Intrusion, Northern Quebec, Canada: *Economic Geology*, v. 109, n. 6, p. 1643-1666.
- Reed, J.C., Jr., Bickford, M.E., Premo, W.R., Aleinikoff, J.N., and Pallister, J.S., 1978, Evolution of the Early Proterozoic Colorado Province: Constraints from U-Pb Geochronology: *Geology*, v. 15, p. 861-865.
- Robinson, K., Gibbs, G. V., and Ribbe, P. H., 1971, The structure of zircon: a comparison with garnet: *The American Mineralogist*, v. 56, p. 782-790.
- Rubin, J.N., Henry, C.D., and Price, J.G., 1989, Hydrothermal Zircons and Zircon Overgrowths, Sierra Blanca Peaks, Texas: *American Mineralogist*, v. 74, p. 865-869.
- Rubin, J.N., Henry, C.D. and Price, J.G., 1993, The Mobility of Zirconium and Other “Immobile” Elements During Hydrothermal Alteration: *Chemical Geology*, v. 110, p. 29-47.
- Salvi, S. and Williams-Jones, A.E., 1996, The Role of Hydrothermal Processes in Concentrating High-Field Strength Elements in the Strange Lake Peralkaline Complex, Northeastern Canada: *Geochimica et Cosmochimica Acta*, v. 60, n. 11, p. 1917-1932.
- Schaltegger, U., 2007, Hydrothermal zircon: *Elements*, v. 3, p. 51 and 79.
- Sheard, E.R., Williams-Jones, A.E., Heiligmann, M., Pederson, C., and Trueman, D.L., 2012, Controls on the Concentration of Zirconium, Niobium, and the Rare Earth Elements in the Thor Lake Rare Metal Deposit, Northwest Territories, Canada: *Economic Geology*, v. 107, p. 81-104.
- Sims, P.K., & Stein, H.J., 2003, Tectonic evolution of the Proterozoic Colorado province, Southern Rocky Mountains: A summary and appraisal, *Rocky Mountain Geology*, v. 38, No. 2, 183-204.
- Smith, D.R., Noblett, J., Wobus, R.A., Unruh, D., and Chamberlain, K.R., 1999, A Review of the Pikes Peak Batholith, Front Range, Central Colorado: A “Type Example” of A-type Granitic Magmatism: *Rocky Mountain Geology*, v. 34, n. 2, p. 389-312.
- Thomas, R., 1994, Estimation of the viscosity and the water content of silicate melts from melt inclusion data: *European Journal of Mineralogy*, v. 6, p. 511-535.
- Thomas, R., Förster, H.J., Rickers, K., and Webster, J.D., 2005, Formation of Extremely F-rich Hydrous Melt Fractions and Hydrothermal Fluids During Differentiation of Highly Evolved tin-granite Magmas: a melt/fluid-inclusion Study: *Contributions to Mineralogy and Petrology*, v. 148, p. 582-601.
- Thomas, R. Webster, J.D., Rhede, D., Seifert, W., Rickers, K., Förster, H.J., Heinrich, W., and Davidson, P., 2006, The Transition from Peraluminous to Peralkaline Granitic Melts: Evidence from Melt Inclusions and Accessory Minerals: *Lithos*, v. 91, p. 137-149.

- Thomas, R. and Davidson, P., 2008, Water and melt/melt immiscibility, the essential components in the formation of pegmatites; evidence from melt inclusions: *Z Geology Weiss*, v. 36, p. 347-364.
- Thomas, R., Davidson, P., and Schmidt, C., 2011, Extreme alkali bicarbonate and carbonate-rich fluid inclusions in granite pegmatite from the Precambrian Ronne granite, Bornholm Island, Denmark: *Contributions to Mineralogy and Petrology*, v. 161, p. 315-329.
- Thomas, R., Davidson, P., and Beurlen, H., 2012, The competing models for the origin and internal evolution of granitic prgmatites in the light of melt and fluid inclusion research: *Miner Petrol*, v. 106, p. 55-73.
- Tromans, D., 2006, Solubility of Crystalline and Metamict Zircon: A thermodynamic Analysis: *Journal of Nuclear Meterials*, v. 357. P. 221-233.
- U.S. Geological Survey, 2014, Mineral Commodity Summaries 2014: *U.S. Geological Survey*, p. 128-129.
- Van Gosen, B.S., Verplanck, P.L., Long, K.R., Gambogi, J., and Seal II, R.R., 2014, The rare-earth elements – vital to modern technologies and lifestyles: *USGS Mineral Resources Program*, Fact Sheet 2014-3078
- Vásquez, P. and Franz, G., 2008, The Triassic Cobquecura (Central Chile): An example of a fayalite-bearing A-type intrusive massif at a continental margin: *Tectonophysics*, v. 459. P. 66-84.
- Van Lichtervelde, M., Holtz, F., and Hanchar, J.M., 2010, Solubility of Manganotantalite, Zircon, and Hafnon in Highly Fluxed Peralkaline to Peraluminous Pegmatitic Melts: *Contributions to Mineralogy and Petrology*, v. 160, p. 17-32.
- Veksler, I.V., Dorfman, A.M., Kamenetsky, M., Dulski, P., and Dingwell, D.B., 2005, Partitioning of Lanthanides and T Between Immiscible Silicate and Fluoride Melts, Fluorine and Cryolite and the Origin of the Lanthanide Tetrad Effect in Igneous Rocks: *Geochimica et Cosmochimica Acta*, v. 69, p. 2847-2860.
- Webber, K.L., Simmons, W.B., Falster, A.U., 1998, Cooling rates and Crystallization Dynamics of Shallow Level Pegmatites, California, USA (abstract): *International Mineral Association 17th Meeting*, Abstract: A145.
- Yang, W., Niu, H, Shan, Q., Sun, W., Zhang, H., Li, N., Jiang, Y., and Yu, X, 2014, Geochemistry of Magmatic and Hydrothermal Zircon from the Highly Evolved Baerzhe Alkaline Granite: Implications for Zr-REE-Nb Mineralization: *Mineralium Desposita*, v. 49, p. 451-470.
- Zhang, Y. and Xu, Z., 2016, Zircon Saturation and Zr Diffusion in Rhyolitic Melts, and Zircon Growth Geospeedometer: *American Mineralogist*, v. 101, p. 1252-1267.
- Zito, G. and Hanson, S.L., 2014, Minerals from the Mirolitic Pegmatities in the Stove Mountain Area, Colorado Springs, Colorado: *Rocks & Minerals*, 89:3, p. 224-237, DOI: 10.1080/.00357529.2014.878181.

APPENDIX A

EMPA ZIRCON DATA

Sample	Pikes Peak Granite																																			
	PP-MR01 Zircon 1						PP-MR01 Zircon 2						PP-MR01 Zircon 4						PP-MR01 Zircon 5						PP-MR01 Zircon 8											
Wt%O																																				
SiO ₂	31.95	31.99	31.39	32.18	31.67	32.09	31.77	32.05	29.66	29.70	32.41	32.11	32.48	32.31	31.80	32.22	32.71	32.03	32.12	31.77	32.40	30.72	32.55	29.87	29.90	31.29	32.59	32.27	32.60	32.33	32.84					
ZrO ₂	63.48	63.25	60.34	63.55	62.52	64.05	63.52	64.65	56.69	56.73	64.55	63.33	64.31	63.72	61.73	64.09	65.10	64.25	63.74	63.54	65.54	60.35	65.02	59.16	57.37	62.23	65.48	63.53	65.95	63.50	65.84					
Al ₂ O ₃	bdl	bdl	bdl	bdl	bdl	bdl	bdl	bdl	0.25	0.10	bdl	bdl	bdl	bdl	bdl	bdl	bdl	bdl	0.01	bdl	bdl	0.12	bdl	bdl	0.07	0.12	0.01	bdl	bdl	bdl	bdl					
MgO	bdl	bdl	bdl	bdl	bdl	bdl	bdl	bdl	0.02	0.03	bdl	bdl	bdl	bdl	bdl	bdl	bdl	bdl	bdl	bdl	bdl	0.04	bdl	0.07	0.05	0.02	0.01	bdl	bdl	bdl	bdl					
ThO ₂	0.06	0.07	0.05	0.08	0.11	bdl	0.04	bdl	0.49	1.01	0.07	0.10	0.08	0.07	0.17	0.04	bdl	bdl	0.11	bdl	0.05	0.30	0.06	0.25	0.07	0.06	0.04	0.14	0.06	0.07	bdl					
UO ₂	0.09	0.10	0.31	0.11	0.15	0.11	bdl	0.07	0.53	0.76	0.07	0.14	0.10	0.11	0.12	0.03	bdl	bdl	0.15	0.07	0.03	0.27	0.09	0.36	0.35	0.23	0.04	0.16	0.04	0.09	0.05					
SnO ₂	bdl	bdl	bdl	bdl	bdl	bdl	0.02	0.01	bdl	bdl	bdl	bdl	bdl	bdl	bdl	bdl	bdl	bdl	0.02	bdl	bdl	bdl	bdl	bdl	bdl	0.02	bdl	0.02	0.01	bdl						
CaO	bdl	bdl	0.05	bdl	bdl	bdl	bdl	0.01	0.71	0.69	0.03	0.01	bdl	0.01	0.01	0.01	bdl	bdl	0.07	bdl	0.01	0.85	0.01	0.81	0.71	0.46	0.06	bdl	bdl	bdl	bdl					
HfO ₂	1.55	1.74	3.65	1.75	1.71	1.72	1.56	1.44	1.26	1.15	1.21	1.23	1.34	1.37	1.33	1.29	1.36	1.60	1.45	1.60	1.53	1.20	1.35	1.43	2.53	1.88	1.62	1.40	1.48	1.56	1.56					
Yb ₂ O ₃	0.11	0.12	0.16	0.11	0.10	0.08	0.05	0.09	0.58	0.39	0.14	0.22	0.20	0.20	0.34	0.09	0.10	0.06	0.19	0.11	0.05	0.19	0.13	0.22	0.23	0.15	0.07	0.13	0.10	0.11	0.11					
Er ₂ O ₃	0.07	0.07	0.08	0.04	0.08	0.06	0.03	0.05	0.30	0.17	0.08	0.12	0.11	0.10	0.22	0.06	0.06	0.04	0.12	0.04	0.03	0.09	0.07	0.09	0.09	0.12	0.05	0.10	0.05	0.06	0.06					
Gd ₂ O ₃	bdl	bdl	bdl	bdl	bdl	bdl	bdl	bdl	0.08	bdl	bdl	bdl	bdl	bdl	0.06	bdl	bdl	bdl	bdl	bdl	bdl	bdl	bdl	bdl	bdl	bdl	bdl	bdl	bdl	bdl	bdl					
Dy ₂ O ₃	0.04	bdl	0.05	0.03	0.04	0.03	0.04	0.02	0.29	0.22	0.03	0.07	0.06	0.08	0.14	0.04	0.05	0.03	0.05	bdl	0.04	0.25	0.04	0.27	0.32	0.12	0.03	0.04	0.03	0.04	0.04					
FeO	bdl	bdl	0.28	bdl	bdl	bdl	0.08	0.08	1.79	1.81	0.11	0.07	0.09	bdl	bdl	bdl	bdl	bdl	0.01	0.23	0.17	1.39	0.10	1.64	1.56	0.53	0.15	0.01	0.01	0.08	0.04					
Sm ₂ O ₃	bdl	bdl	bdl	bdl	bdl	bdl	bdl	bdl	bdl	bdl	bdl	bdl	bdl	bdl	bdl	bdl	bdl	bdl	bdl	bdl	bdl	bdl	bdl	bdl	bdl	bdl	bdl	bdl	bdl	bdl	bdl					
MnO	0.01	bdl	0.04	bdl	bdl	bdl	bdl	bdl	0.52	0.55	0.02	bdl	bdl	bdl	bdl	bdl	bdl	bdl	bdl	bdl	bdl	0.74	0.01	0.90	1.02	0.31	bdl	bdl	bdl	bdl	bdl					
Pr ₂ O ₃	bdl	bdl	bdl	bdl	bdl	bdl	bdl	bdl	bdl	bdl	bdl	bdl	bdl	bdl	bdl	bdl	bdl	bdl	bdl	bdl	bdl	bdl	bdl	bdl	bdl	bdl	0.06	bdl	bdl	bdl	bdl					
Nd ₂ O ₃	bdl	bdl	bdl	bdl	bdl	bdl	bdl	bdl	bdl	bdl	bdl	bdl	bdl	bdl	bdl	bdl	bdl	bdl	bdl	bdl	bdl	bdl	bdl	bdl	bdl	bdl	bdl	bdl	bdl	bdl	bdl					
Ce ₂ O ₃	bdl	bdl	bdl	bdl	bdl	bdl	bdl	bdl	0.03	bdl	bdl	bdl	bdl	bdl	bdl	bdl	bdl	bdl	bdl	bdl	bdl	bdl	bdl	bdl	bdl	bdl	bdl	bdl	bdl	bdl	bdl					
Y ₂ O ₃	0.36	0.43	0.22	0.34	0.40	0.29	0.15	0.37	2.11	1.07	0.52	0.76	0.69	0.66	1.37	0.40	0.27	0.14	0.73	0.23	0.17	0.73	0.33	0.63	0.50	0.48	0.23	0.54	0.25	0.29	0.22					
P ₂ O ₅	bdl	bdl	0.11	bdl	bdl	bdl	bdl	bdl	0.15	bdl	bdl	bdl	0.09	bdl	0.07	bdl	bdl	bdl	bdl	bdl	bdl	bdl	bdl	bdl	0.08	0.12	bdl	bdl	bdl	bdl	bdl					
TOTAL	97.62	97.79	96.64	98.07	96.65	98.33	97.29	98.79	95.43	94.32	99.26	98.19	99.55	98.70	97.35	98.18	99.69	98.17	98.73	97.65	99.97	97.24	99.78	95.58	94.80	98.06	100.42	98.35	100.59	98.16	100.74					

[illegible]

	Mount Rosa Granite																															
Sample	PP-MR2016-07 Zircon 1								PP-MR2016-07 Zircon 2								PP-MR2016-07 Zircon 6								PP-MR2016-07 Zircon 7							
Wt%O																																
SiO ₂	32.30	32.28	32.47	30.85	29.68	32.02	28.63	32.76	32.54	32.70	32.34	32.69	32.39	32.36	32.68	32.47	32.43	29.63	32.78	29.36	32.05	32.35	32.46	32.91	32.17	32.54	32.61					
ZrO ₂	64.61	63.61	65.61	61.68	59.52	63.53	57.05	65.45	64.64	64.99	64.76	65.05	65.88	63.71	65.46	63.95	64.25	58.35	65.18	56.31	63.27	64.05	64.05	64.88	63.64	64.70	64.32					
Al ₂ O ₃	bdl	0.01	0.01	0.36	0.20	0.01	1.06	bdl	0.02	0.01	0.01	0.01	bdl	0.01	bdl	0.02	bdl	0.01	bdl	0.63	0.03	0.03	0.03	0.01	0.02	0.01	0.04					
MgO	bdl	bdl	bdl	0.02	0.03	bdl	0.04	bdl	bdl	bdl	bdl	bdl	bdl	bdl	bdl	bdl	bdl	bdl	bdl	0.03	bdl	bdl	bdl	bdl	bdl	bdl	bdl					
ThO ₂	bdl	0.12	0.06	0.12	0.10	bdl	0.11	0.05	0.04	0.04	0.06	0.05	bdl	0.08	0.04	bdl	bdl	0.09	bdl	0.29	0.05	0.11	0.09	bdl	0.04	0.06	0.07					
UO ₂	0.10	0.10	bdl	0.64	0.71	0.15	0.71	bdl	0.04	0.09	0.15	0.14	0.04	0.08	0.11	0.14	0.07	0.32	0.03	0.82	0.12	0.10	0.11	0.05	0.12	0.10	0.20					
SnO ₂	0.02	bdl	bdl	0.03	bdl	0.02	bdl	bdl	bdl	bdl	0.02	bdl	bdl	bdl	bdl	bdl	bdl	bdl	bdl	0.03	bdl	bdl	bdl	bdl	bdl	bdl	0.02					
CaO	bdl	bdl	bdl	0.10	0.33	bdl	0.71	bdl	bdl	bdl	bdl	bdl	bdl	bdl	bdl	bdl	bdl	0.05	0.01	0.07	bdl	bdl	bdl	bdl	bdl	bdl	0.01					
HfO ₂	1.82	1.31	1.41	1.46	1.31	2.16	2.75	1.61	1.32	1.20	1.43	1.46	1.26	1.23	1.35	1.89	1.89	2.67	1.16	2.71	1.83	1.47	1.25	1.20	1.91	1.08	1.35					
Yb ₂ O ₃	0.05	0.19	0.03	0.13	0.23	0.09	0.44	0.07	0.13	0.19	0.15	0.17	0.07	0.22	0.16	0.11	0.07	0.24	0.10	0.32	0.13	0.15	0.16	0.12	0.07	0.23	0.20					
Er ₂ O ₃	0.04	0.11	0.04	0.03	0.07	0.04	0.12	0.06	0.11	0.10	0.06	0.05	bdl	0.13	0.06	0.06	0.03	0.08	0.07	0.13	0.05	0.12	0.09	0.08	0.06	0.09	0.09					
Gd ₂ O ₃	bdl	0.05	bdl	bdl	bdl	bdl	bdl	bdl	0.05	bdl	bdl	bdl	bdl	bdl	bdl	bdl	bdl	bdl	bdl	0.05	bdl	bdl	bdl	bdl	bdl	bdl	bdl					
Dy ₂ O ₃	bdl	0.04	bdl	0.16	0.25	0.02	0.28	0.02	0.06	0.04	0.04	bdl	bdl	0.08	0.03	bdl	bdl	0.17	0.04	0.26	bdl	0.04	0.04	0.03	0.04	0.04	bdl					
FeO	0.03	0.02	0.09	0.87	1.76	bdl	1.66	0.02	0.05	0.07	bdl	0.01	0.03	0.07	0.05	0.07	0.05	1.56	0.02	1.27	0.18	bdl	0.10	0.06	bdl	0.02	0.14					
Sm ₂ O ₃	bdl	bdl	bdl	bdl	bdl	bdl	bdl	bdl	bdl	bdl	bdl	bdl	bdl	bdl	bdl	bdl	bdl	bdl	bdl	bdl	bdl	bdl	bdl	bdl	bdl	bdl	bdl					
MnO	bdl	bdl	bdl	0.58	0.93	bdl	0.91	bdl	0.01	bdl	bdl	bdl	bdl	0.01	bdl	bdl	bdl	0.51	bdl	0.74	bdl	bdl	bdl	bdl	bdl	bdl	bdl					
Pr ₂ O ₃	bdl	bdl	0.04	bdl	bdl	bdl	bdl	bdl	0.04	bdl	bdl	bdl	bdl	bdl	bdl	bdl	bdl	bdl	bdl	bdl	bdl	bdl	bdl	bdl	bdl	bdl	bdl					
Nd ₂ O ₃	bdl	bdl	bdl	bdl	bdl	bdl	bdl	bdl	bdl	bdl	bdl	bdl	bdl	bdl	bdl	bdl	bdl	bdl	bdl	0.06	bdl	bdl	bdl	bdl	bdl	bdl	bdl					
Ce ₂ O ₃	bdl	bdl	bdl	bdl	bdl	bdl	bdl	bdl	bdl	bdl	bdl	bdl	bdl	bdl	bdl	bdl	bdl	bdl	bdl	0.07	bdl	bdl	bdl	bdl	bdl	bdl	bdl					
Y ₂ O ₃	0.12	0.83	0.13	0.28	0.24	0.17	0.27	0.25	0.62	0.64	0.21	0.21	0.15	0.86	0.41	0.28	0.17	0.54	0.40	0.97	0.33	0.64	0.67	0.42	0.16	0.29	0.27					
P ₂ O ₅	bdl	bdl	bdl	bdl	bdl	bdl	bdl	bdl	bdl	bdl	bdl	bdl	bdl	bdl	bdl	bdl	bdl	bdl	bdl	0.13	bdl	bdl	bdl	bdl	bdl	bdl	bdl					
TOTAL	99.03	98.74	99.84	97.19	95.26	98.25	94.70	100.24	99.65	100.09	99.18	99.88	99.84	98.79	100.36	98.96	98.95	94.05	99.82	94.12	98.05	98.95	99.07	99.82	98.16	99.18	99.27					

Mount Rosa Granite (cont.)											
Sample	PP-MR2016-13 Zircon 2	PP-MR2016-13 Zircon 3	PP-MR2016-13 Zircon 4	PP-MR2016-13 Zircon 6	PP-MR25 Zircon 2	PP-MR25 Zircon 3		PP-MR25 Zircon 5		PP-MR25 Zircon 7	
Wt%O											
SiO ₂	30.74	31.98	32.80	32.73	32.25	31.85	32.08	31.93	32.57	32.16	32.01
ZrO ₂	61.73	64.38	66.89	64.80	64.18	62.92	63.42	63.42	67.04	64.17	63.15
Al ₂ O ₃	0.20	0.01	0.01	0.01	0.18	bdl	bdl	bdl	bdl	bdl	bdl
MgO	bdl	bdl	bdl	bdl	bdl	bdl	bdl	bdl	bdl	bdl	bdl
ThO ₂	0.05	bdl	bdl	bdl	bdl	bdl	bdl	0.05	bdl	0.04	bdl
UO ₂	0.25	bdl	bdl	bdl	0.24	0.13	0.09	0.12	bdl	0.07	0.08
SnO ₂	bdl	bdl	bdl	bdl	bdl	bdl	bdl	bdl	bdl	bdl	bdl
CaO	0.26	0.01	0.03	0.04	0.01	bdl	bdl	bdl	bdl	0.01	0.01
HfO ₂	1.10	1.96	1.89	1.55	1.18	1.35	1.35	1.38	1.65	1.37	1.31
Yb ₂ O ₃	0.49	0.22	0.16	0.22	0.30	0.38	0.33	0.47	0.12	0.30	0.34
Er ₂ O ₃	0.14	0.04	bdl	0.06	0.07	0.19	0.14	0.21	bdl	0.12	0.15
Gd ₂ O ₃	bdl	bdl	bdl	bdl	bdl	bdl	bdl	0.05	bdl	bdl	bdl
Dy ₂ O ₃	0.17	0.02	bdl	0.06	bdl	0.14	0.07	0.12	bdl	0.09	0.11
FeO	1.15	0.02	0.01	0.01	0.06	bdl	bdl	0.01	0.04	bdl	bdl
Sm ₂ O ₃	bdl	bdl	bdl	bdl	bdl	bdl	bdl	bdl	bdl	bdl	bdl
MnO	0.39	0.01	bdl	bdl	bdl	bdl	bdl	bdl	bdl	bdl	bdl
Pr ₂ O ₃	bdl	bdl	bdl	bdl	bdl	bdl	bdl	bdl	bdl	bdl	bdl
Nd ₂ O ₃	bdl	bdl	bdl	bdl	bdl	bdl	bdl	bdl	bdl	bdl	bdl
Ce ₂ O ₃	bdl	bdl	bdl	bdl	bdl	bdl	bdl	bdl	bdl	bdl	bdl
Y ₂ O ₃	0.47	0.13	0.07	0.40	0.21	0.71	0.55	0.75	0.06	0.56	0.55
P ₂ O ₅	0.32	bdl	bdl	bdl	0.12	0.18	0.14	0.23	bdl	0.08	0.15
TOTAL	97.36	98.80	101.82	99.88	98.69	97.78	98.10	98.63	101.28	98.88	97.78

	Mafic Dike																			
Sample	PP-MR58 Zircon 2						PP-MR58 Zircon 3					PP-MR58 Zircon 5				PP-MR58 Zircon 6				
Wt%O																				
SiO ₂	32.40	32.60	32.55	32.44	32.38	29.45	31.75	28.41	27.31	27.51	29.22	32.76	32.13	31.58	31.40	31.90	29.32	28.20	31.39	31.00
ZrO ₂	62.74	64.69	64.46	64.72	63.32	58.02	60.49	58.02	55.97	53.23	52.38	65.84	64.59	60.20	59.12	59.33	51.18	49.83	57.88	56.09
Al ₂ O ₃	0.01	bdl	bdl	bdl	0.01	0.17	bdl	0.57	0.71	0.95	0.02	bdl	bdl	bdl	bdl	0.02	0.20	0.69	0.01	0.01
MgO	bdl	bdl	bdl	bdl	bdl	bdl	bdl	0.01	bdl	0.03	bdl	bdl	bdl	bdl	bdl	bdl	bdl	bdl	bdl	bdl
ThO ₂	bdl	bdl	bdl	bdl	bdl	bdl	bdl	bdl	bdl	bdl	bdl	bdl	bdl	bdl	bdl	bdl	bdl	bdl	bdl	bdl
UO ₂	bdl	bdl	bdl	bdl	bdl	bdl	bdl	bdl	bdl	bdl	bdl	bdl	bdl	bdl	bdl	bdl	bdl	bdl	bdl	bdl
SnO ₂	bdl	bdl	bdl	bdl	bdl	bdl	bdl	bdl	bdl	bdl	bdl	bdl	bdl	bdl	bdl	bdl	bdl	bdl	bdl	bdl
CaO	bdl	bdl	bdl	bdl	bdl	0.24	0.53	0.51	0.52	0.55	1.19	bdl	bdl	0.07	0.63	0.01	0.95	0.46	0.14	0.30
HfO ₂	1.71	1.49	1.73	1.71	1.63	1.52	1.00	0.95	0.95	0.89	0.85	1.21	1.81	1.27	1.14	1.28	0.99	1.18	1.10	1.05
Yb ₂ O ₃	0.24	0.17	0.18	0.18	0.30	0.31	0.28	0.35	0.33	0.54	0.36	0.13	0.20	0.25	0.34	0.18	0.31	0.32	0.31	0.40
Er ₂ O ₃	0.18	0.14	0.13	0.13	0.19	0.32	0.26	0.38	0.34	0.59	0.49	0.04	0.12	0.24	0.40	0.13	0.31	0.43	0.33	0.44
Gd ₂ O ₃	0.08	bdl	0.10	0.11	0.06	0.17	0.20	0.30	0.33	0.43	0.42	bdl	bdl	0.28	0.32	0.19	0.35	0.44	0.34	0.34
Dy ₂ O ₃	0.18	0.11	0.16	0.16	0.10	0.32	0.34	0.44	0.42	0.73	0.78	0.04	0.08	0.32	0.50	0.24	0.62	0.69	0.40	0.50
FeO	0.03	0.04	0.05	0.06	0.03	0.74	0.31	1.53	2.78	2.45	1.18	0.32	0.23	0.14	0.13	0.07	1.18	1.43	0.17	0.16
Sm ₂ O ₃	0.04	bdl	bdl	bdl	bdl	bdl	bdl	0.11	0.06	0.12	0.08	bdl	bdl	bdl	bdl	0.14	0.11	0.19	0.09	0.04
MnO	bdl	bdl	0.01	bdl	bdl	0.01	0.03	0.02	0.02	0.03	0.64	bdl	bdl	0.02	0.04	bdl	0.40	0.07	0.04	0.05
Pr ₂ O ₃	bdl	bdl	bdl	bdl	bdl	bdl	bdl	bdl	bdl	0.06	bdl	bdl	bdl	bdl	bdl	0.07	0.05	bdl	bdl	bdl
Nd ₂ O ₃	bdl	bdl	bdl	bdl	bdl	0.05	0.04	0.19	0.15	0.21	0.15	bdl	bdl	0.08	bdl	0.58	0.23	0.30	0.18	0.06
Ce ₂ O ₃	bdl	bdl	bdl	bdl	bdl	0.03	0.07	0.09	0.10	0.10	0.28	bdl	bdl	0.09	0.04	0.91	0.41	0.26	0.17	0.11
Y ₂ O ₃	1.57	0.95	1.09	1.08	1.32	2.43	3.02	3.50	3.51	5.48	4.99	0.33	0.72	3.38	3.27	1.96	4.44	5.36	3.99	5.48
P ₂ O ₅	bdl	bdl	bdl	bdl	bdl	bdl	bdl	bdl	bdl	bdl	bdl	bdl	bdl	bdl	bdl	bdl	bdl	bdl	bdl	bdl
TOTAL	95.75	98.46	98.62	98.77	97.69	92.07	95.27	91.16	89.16	89.49	88.64	92.18	98.11	96.26	95.19	92.10	89.35	82.80	92.49	93.83

Sample	Type-(I) Pegmatite																																																
	AS-19 Zircon 1										AS-19 Zircon 2										AS-19 Zircon 3										AS-19 Zircon 4										AS-19 Zircon 5								
Wt%	32.06	32.70	28.86	28.35	32.93	32.76	30.53	32.78	32.71	32.03	32.23	28.96	27.73	32.31	32.47	28.69	28.92	31.83	31.98	28.80	32.72	29.79	32.60	32.44	28.93	32.64	29.39	32.18	32.09	28.76	32.39	32.53	32.13	28.47	32.62	32.33	28.68	28.89	32.06	32.09	32.28	28.54	32.20	32.68					
SiO ₂	64.18	66.36	56.11	56.18	66.12	66.14	61.03	65.83	65.67	64.36	64.46	57.70	53.52	63.75	64.64	56.95	57.26	62.86	63.43	56.65	65.25	59.12	64.92	64.90	57.35	65.27	59.12	63.64	64.04	56.86	64.07	65.07	64.63	55.84	65.36	64.53	56.47	57.24	64.45	63.93	64.20	56.38	64.17	64.98					
ZrO ₂	bdil	bdil	0.25	0.15	bdil	bdil	0.13	bdil	bdil	bdil	bdil	0.08	0.15	bdil	bdil	0.07	0.16	bdil	bdil	0.05	bdil	0.06	bdil	bdil	0.16	bdil	0.13	bdil	bdil	0.09	bdil	bdil	bdil	0.23	bdil	bdil	0.16	0.09	bdil	bdil	bdil	0.11	bdil	bdil					
Al ₂ O ₃	bdil	bdil	0.02	0.03	bdil	bdil	bdil	0.03	bdil	bdil	bdil	0.03	0.06	bdil	bdil	0.07	0.03	bdil	bdil	0.06	bdil	0.04	bdil	bdil	0.03	bdil	0.04	bdil	bdil	bdil	0.03	bdil	bdil	bdil	0.02	bdil	bdil	0.04	0.04	bdil	bdil	bdil	0.02	bdil	bdil				
MgO	0.11	bdil	0.22	0.41	0.04	bdil	0.08	bdil	0.05	0.14	0.10	0.32	0.50	0.08	0.07	0.41	0.36	0.20	0.13	0.20	bdil	0.13	0.05	0.07	0.27	bdil	0.09	0.13	0.12	0.32	0.11	bdil	0.09	0.36	bdil	0.08	0.41	0.39	0.15	0.11	0.13	0.53	bdil	bdil					
ThO ₂	0.10	bdil	0.29	0.29	bdil	bdil	0.22	0.03	0.07	0.10	0.10	0.27	0.30	0.07	0.12	0.26	0.26	0.12	0.09	0.28	0.07	0.24	0.13	0.13	0.28	0.07	0.26	0.08	0.08	0.24	0.15	0.10	0.13	0.22	0.09	0.05	0.31	0.22	0.10	0.10	0.08	0.29	0.27	0.14					
UO ₂	bdil	bdil	0.27	0.29	bdil	bdil	bdil	bdil	bdil	bdil	bdil	0.09	0.30	bdil	bdil	0.12	0.14	bdil	bdil	0.02	0.05	bdil	0.13	bdil	0.02	0.30	bdil	0.02	bdil	bdil	0.11	bdil	0.02	bdil	0.08	bdil	bdil	0.21	0.16	bdil	bdil	0.02	0.16	0.02	bdil				
SnO ₂	bdil	bdil	0.62	0.72	0.01	bdil	0.45	0.01	bdil	bdil	bdil	0.49	0.92	bdil	bdil	0.88	0.59	bdil	bdil	0.81	bdil	0.69	bdil	bdil	0.80	bdil	0.76	bdil	bdil	0.44	bdil	bdil	0.52	bdil	bdil	0.80	0.65	bdil	bdil	bdil	0.66	bdil	bdil						
CaO	1.07	0.96	0.95	0.93	1.08	0.97	0.83	1.15	1.01	1.07	1.06	0.80	0.87	0.91	0.91	0.88	0.86	1.07	1.03	0.84	0.98	0.87	0.89	0.88	0.83	0.99	0.82	1.04	1.04	0.83	0.95	0.89	1.05	0.87	0.91	0.92	0.92	0.85	1.07	1.02	0.92	0.93	0.95	0.93					
HfO ₂	0.59	0.20	0.83	0.79	0.07	0.11	0.51	0.10	0.13	0.62	0.48	0.69	0.99	0.35	0.39	0.78	0.65	0.68	0.60	0.69	0.17	0.46	0.35	0.32	0.54	0.18	0.53	0.60	0.54	0.85	0.27	0.35	0.52	0.85	0.27	0.18	0.57	0.68	0.46	0.50	0.41	0.91	0.44	0.33					
Yb ₂ O ₃	0.33	0.09	0.51	0.50	0.03	0.06	0.24	0.04	0.06	0.35	0.27	0.53	0.61	0.21	0.24	0.51	0.45	0.38	0.36	0.38	0.07	0.29	0.21	0.18	0.35	0.10	0.32	0.32	0.31	0.64	0.15	0.19	0.31	0.63	0.16	0.14	0.43	0.50	0.27	0.31	0.26	0.53	0.18	0.18					
Er ₂ O ₃	0.07	bdil	0.17	0.20	bdil	bdil	bdil	bdil	bdil	0.08	0.09	0.16	0.21	0.06	0.05	0.17	0.14	0.05	0.12	0.15	bdil	0.11	bdil	0.07	0.12	bdil	0.08	0.06	0.06	0.21	bdil	bdil	bdil	0.19	bdil	0.08	0.15	0.15	0.05	0.09	0.07	0.22	bdil	0.06					
Gd ₂ O ₃	0.14	bdil	0.49	0.53	0.05	0.03	0.19	0.02	0.02	0.13	0.11	0.48	0.65	0.14	0.10	0.52	0.44	0.17	0.16	0.44	0.04	0.36	0.12	0.11	0.48	0.05	0.34	0.12	0.12	0.60	0.08	0.15	0.15	0.57	0.08	0.06	0.53	0.47	0.10	0.13	0.13	0.55	0.07	0.11					
Dy ₂ O ₃	0.01	0.04	1.35	1.49	0.02	0.03	1.07	0.09	0.11	bdil	bdil	1.04	1.45	bdil	bdil	1.37	1.14	0.02	bdil	1.39	0.08	1.43	bdil	bdil	1.51	0.03	1.32	bdil	bdil	0.91	0.03	0.04	bdil	1.04	0.02	0.08	1.66	1.28	bdil	bdil	0.02	1.16	0.18	0.06					
FeO	bdil	bdil	0.07	0.06	bdil	bdil	bdil	bdil	bdil	bdil	bdil	bdil	bdil	bdil	bdil	bdil	bdil	bdil	bdil	bdil	bdil	0.04	bdil	bdil	bdil	bdil	bdil	bdil	bdil	bdil	bdil	bdil	bdil	bdil	bdil	bdil	bdil	bdil	bdil	bdil	bdil	bdil	bdil	bdil	bdil				
Sm ₂ O ₃	bdil	bdil	0.33	0.34	bdil	bdil	0.32	bdil	bdil	bdil	bdil	0.35	0.47	bdil	bdil	0.46	0.38	0.01	bdil	0.49	bdil	0.45	bdil	bdil	0.46	0.01	0.44	bdil	bdil	0.28	bdil	bdil	bdil	0.29	bdil	bdil	0.42	0.37	bdil	bdil	bdil	0.39	bdil	bdil					
MnO	bdil	bdil	bdil	bdil	bdil	bdil	bdil	bdil	bdil	bdil	bdil	bdil	bdil	bdil	bdil	bdil	bdil	bdil	bdil	bdil	bdil	bdil	bdil	bdil	bdil	bdil	bdil	bdil	bdil	bdil	bdil	bdil	bdil	bdil	bdil	bdil	bdil	bdil	bdil	bdil	bdil	bdil	bdil	bdil	bdil				
Pr ₂ O ₃	bdil	bdil	bdil	bdil	bdil	bdil	bdil	bdil	bdil	bdil	bdil	bdil	bdil	bdil	bdil	bdil	bdil	bdil	bdil	bdil	bdil	bdil	bdil	bdil	bdil	bdil	bdil	bdil	bdil	bdil	bdil	bdil	bdil	bdil	bdil	bdil	bdil	bdil	bdil	bdil	bdil	bdil	bdil	bdil	bdil				
Nd ₂ O ₃	bdil	bdil	0.03	0.03	bdil	bdil	bdil	bdil	bdil	bdil	bdil	bdil	0.03	bdil	bdil	bdil	bdil	bdil	bdil	bdil	bdil	bdil	bdil	bdil	bdil	0.03	bdil	bdil	bdil	bdil	bdil	bdil	bdil	bdil	bdil	bdil	bdil	bdil	bdil	bdil	bdil	bdil	bdil	bdil	bdil	bdil			
Ce ₂ O ₃	bdil	bdil	bdil	bdil	bdil	bdil	bdil	bdil	bdil	bdil	bdil	bdil	bdil	bdil	bdil	bdil	bdil	bdil	bdil	bdil	bdil	bdil	bdil	bdil	bdil	bdil	bdil	bdil	bdil	bdil	bdil	bdil	bdil	bdil	bdil	bdil	bdil	bdil	bdil	bdil	bdil	bdil	bdil	bdil	bdil				
Y ₂ O ₃	0.84	0.19	2.38	2.54	0.10	0.13	0.64	0.11	0.16	0.86	0.73	2.37	2.58	0.67	0.60	2.04	2.29	1.01	0.87	1.37	0.26	1.24	0.64	0.63	1.73	0.22	1.40	0.86	0.78	2.74	0.45	0.63	0.79	2.82	0.44	0.68	2.12	2.42	0.80	0.87	0.87	2.35	0.42	0.49					
P ₂ O ₅	0.20	0.12	0.36	0.34	bdil	bdil	0.25	bdil	bdil	0.19	0.22	0.36	0.27	bdil	0.09	0.30	0.44	0.30	0.27	0.42	bdil	0.08	bdil	0.08	0.24	bdil	0.29	0.12	0.20	0.44	bdil	bdil	0.16	0.42	bdil	bdil	0.26	0.33	0.16	0.18	0.13	0.37	0.19	bdil					
TOTAL	99.64	100.66	94.09	94.16	100.44	100.25	96.50	100.15	99.92	99.82	99.74	94.67	91.63	98.53	99.63	94.50	94.48	98.62	98.98	93.07	99.82	95.53	99.88	99.74	94.40	99.60	95.26	99.08	99.31	94.35	98.68	100.02	99.90	93.45	99.96	99.24	94.14	94.69	99.59	99.29	99.48	94.13	99.07	99.99					

Sample	Type-(II) Pegmatite																																																														
	AS-MR38-01 Zircon 2								AS-MR38-01 Zircon 5								AS-MR38-01 Zircon 6								AS-MR38-01 Zircon 7								AS-MR38-03 Zircon 1								AS-MR38-03 Zircon 2								AS-MR38-03 Zircon 3								AS-MR38-03 Zircon 4						
Wt%SiO ₂	31.89	32.40	31.88	31.86	31.82	32.22	31.67	31.48	28.39	30.85	24.61	31.53	25.98	31.84	31.26	23.47	32.03	31.51	21.61	16.00	28.61	28.27	27.61	28.06	26.66	26.45	28.19	27.08	27.96	30.62	27.79	29.21	27.62	27.03	31.12	23.42	30.41	31.49	26.64	29.63	29.86	29.82	31.37	26.87	30.87	29.75	30.80	30.57	31.62	28.92	26.32												
ZrO ₂	62.89	63.99	63.28	63.42	64.00	64.75	64.05	62.62	56.47	61.41	52.55	63.58	49.68	63.25	63.28	45.89	64.45	63.06	39.63	14.08	53.10	53.09	51.37	52.07	47.01	48.77	52.26	48.68	51.62	57.81	52.11	53.67	50.43	49.52	57.90	50.84	57.63	57.73	49.91	58.60	58.14	57.35	59.45	54.38	56.44	57.97	57.42	57.12	56.73	53.76	53.23												
Al ₂ O ₃	0.04	0.04	0.02	0.01	0.01	0.01	0.01	bdil	0.30	bdil	0.49	bdil	0.55	bdil	bdil	0.67	bdil	bdil	1.40	0.35	0.81	0.74	1.21	1.15	1.25	0.98	0.63	0.61	0.56	0.54	0.48	0.56	0.97	0.70	0.52	1.51	0.39	0.37	0.62	0.55	0.40	0.51	0.51	1.10	0.48	0.40	0.50	0.46	0.55	0.31	1.32												
MgO	bdil	bdil	bdil	bdil	bdil	bdil	bdil	bdil	0.01	bdil	0.01	bdil	0.02	bdil	bdil	0.01	bdil	bdil	bdil	bdil	0.02	0.03	0.03	0.02	0.03	0.02	0.02	0.04	0.01	bdil	0.01	0.01	0.04	bdil	bdil	bdil	bdil	bdil	bdil	bdil	bdil	bdil	bdil	bdil	bdil	bdil	bdil	bdil	bdil	bdil	bdil	bdil	bdil										
ThO ₂	bdil	bdil	bdil	bdil	0.04	0.07	bdil	0.11	0.39	0.21	0.50	0.16	0.88	bdil	0.05	1.03	bdil	0.11	5.01	1.26	2.50	2.45	2.80	3.46	6.68	3.76	3.47	5.87	2.09	0.22	3.01	1.58	5.83	4.95	0.06	1.10	0.61	0.39	0.24	0.77	0.39	0.56	bdil	0.02	bdil	0.16	bdil	0.04	0.08	0.50	1.54												
UO ₂	bdil	bdil	0.06	0.03	0.04	bdil	bdil	bdil	0.03	bdil	0.10	bdil	0.08	bdil	0.03	0.08	bdil	0.04	bdil	bdil	bdil	bdil	bdil	bdil	bdil	bdil	bdil	bdil	bdil	bdil	bdil	bdil	bdil	bdil	bdil	bdil	bdil	bdil	bdil	bdil	bdil	bdil	bdil	bdil	bdil	bdil	bdil	bdil	bdil	bdil	bdil	bdil	bdil	bdil									
SnO ₂	bdil	bdil	0.02	0.02	0.01	bdil	bdil	bdil	0.02	0.02	bdil	bdil	bdil	bdil	bdil	bdil	bdil	bdil	0.10	0.13	0.46	0.46	0.41	0.36	0.17	0.30	0.37	0.19	0.46	0.90	0.38	0.56	0.23	0.29	0.93	0.59	0.78	0.79	0.26	0.74	0.79	0.76	0.83	0.59	0.86	0.83	0.90	0.95	0.74	0.60	0.57												
CaO	bdil	bdil	0.14	0.13	0.03	0.38	0.05	0.41	0.28	0.10	0.53	0.09	0.11	1.08	0.26	0.86	0.90	1.14	1.13	1.25	0.83	1.06	1.02	1.27	1.25	1.03	1.31	1.31	0.75	0.85	0.80	0.41	1.25	1.10	0.99	0.86	0.03	0.86	0.89	0.53	1.04	0.24	0.07	0.64	0.07	0.07	0.08	1.06	0.90	0.90	0.90	0.90											
Na ₂ O	2.14	2.14	1.45	1.51	1.01	0.93	2.15	1.56	1.80	1.12	2.81	1.66	1.68	2.84	1.13	2.83	2.62	2.50	2.69	2.79	2.72	2.65	2.69	2.72	2.65	2.69	2.65	2.69	2.65	2.69	2.65	2.69	2.65	2.69	2.65	2.69	2.65	2.69	2.65	2.69	2.65	2.69	2.65	2.69	2.65	2.69	2.65	2.69	2.65	2.69	2.65	2.69											
Y ₂ O ₃	0.25	0.27	0.27	0.30	0.43	0.12	0.72	0.46	1.14	0.66	1.30	0.43	1.05	0.36	0.53	1.55	1.53	0.58	0.80	0.62	1.32	1.26	1.21	1.27	0.89	1.45	1.21	1.09	1.82	1.67	1.80	1.92	0.55	0.06	0.72	1.45	0.81	0.96	1.28	1.10	0.85	0.96	0.80	1.24	1.24	1.16	1.33	1.08	0.84	1.34													
Er ₂ O ₃	0.11	0.11	0.12	0.12	0.09	0.02	0.13	0.24	0.75	0.35	0.94	0.21	0.73	0.20	0.28	1.11	0.05	0.28	0.35	0.16	0.17	0.16	0.17	0.15	0.10	0.24	0.16	0.14	0.27	0.17	0.23	0.24	0.06	0.16	0.07	0.58	0.15	0.20	0.22	0.26	0.16	0.19	0.16	0.28	0.11	0.12	0.12	0.13	0.12	0.07	0.29												
Gd ₂ O ₃	bdil	bdil	bdil	bdil	bdil	bdil	bdil	0.08	0.22	0.10	0.35	0.05	0.29	0.06	0.06	0.44	0.07	bdil	bdil	bdil	bdil	bdil	bdil	bdil	bdil	bdil	bdil	bdil	bdil	bdil	bdil	bdil	bdil	bdil	bdil	bdil	bdil	bdil	bdil	bdil	bdil	bdil	bdil	bdil	bdil	bdil	bdil	bdil	bdil	bdil	bdil	bdil	bdil	bdil	bdil								
Dy ₂ O ₃	0.04	0.05	0.04	0.04	0.02	bdil	bdil	0.10	0.57	0.17	0.79	0.10	0.71	0.08	0.11	0.98	0.03	0.12	0.38	0.25	0.22	0.31	0.18	0.21	0.38	0.21	0.20	0.24	0.08	0.20	0.18	0.19	0.24	0.12	0.55	0.15	0.13	0.26	0.22	0.15	0.16	0.10	0.25	0.09	0.10	0.11	0.11	0.10	0.16	0.28													
FeO	0.06	0.07	0.01	0.02	0.01	0.01	0.02	0.16	0.98	0.04	1.62	0.07	1.40	0.17	0.03	1.36	0.10	0.20	9.17	39.42	26.55	2.78	2.57	4.00	2.11	2.22	2.21	2.51	2.17	0.43	2.51	1.22	2.10	2.33	0.52	2.71	0.71	0.79	0.26	1.06	0.45	0.67	1.08	1.78	0.47	0.50	0.48	0.60	0.58	1.86	1.75												
Sm ₂ O ₃	bdil	bdil	bdil	bdil	bdil	bdil	bdil	bdil	bdil	bdil	bdil	bdil	bdil	bdil	bdil	bdil	bdil	bdil	bdil	bdil	bdil	bdil	bdil	bdil	bdil	bdil	bdil	bdil	bdil	bdil	bdil	bdil	bdil	bdil	bdil	bdil	bdil	bdil	bdil	bdil	bdil	bdil	bdil	bdil	bdil	bdil	bdil	bdil	bdil	bdil	bdil	bdil	bdil	bdil	bdil	bdil							
MnO	bdil	bdil	bdil	bdil	bdil	bdil	bdil	bdil	0.02	bdil	0.02	bdil	0.03	bdil	bdil	0.02	bdil	bdil	0.31	0.15	0.53	0.54	0.58	0.48	0.42	0.50	0.58	0.48	0.48	0.23	0.58	0.38	0.57	0.50	0.41	0.09	0.35	0.32	0.49	0.31	0.34	0.31	0.41	0.21	0.33	0.34	0.31	0.28	0.36	0.53	0.19												
Ni ₂ O ₃	bdil	bdil	bdil	bdil	bdil	bdil	bdil	bdil	bdil	bdil	bdil	bdil	bdil	bdil	bdil	bdil	bdil	bdil	bdil	bdil	bdil	bdil	bdil	bdil	bdil	bdil	bdil	bdil	bdil	bdil	bdil	bdil	bdil	bdil	bdil	bdil	bdil	bdil	bdil	bdil	bdil	bdil	bdil	bdil	bdil	bdil	bdil	bdil	bdil	bdil	bdil	bdil	bdil	bdil	bdil	bdil	bdil						
Pd ₂ O	bdil	bdil	bdil	bdil	bdil	bdil	bdil	bdil	bdil	bdil	0.02	bdil	0.02	bdil	bdil	bdil	0.02	bdil	0.07	bdil	0.02	bdil	0.06	bdil	bdil	bdil	bdil	bdil	bdil	bdil	bdil	bdil	bdil	bdil	bdil	bdil	bdil	bdil	bdil	bdil	bdil	bdil	bdil	bdil	bdil	bdil	bdil	bdil	bdil	bdil	bdil	bdil	bdil	bdil	bdil	bdil	bdil						
Ce ₂ O ₃	bdil	bdil	bdil	bdil	bdil	bdil	bdil	bdil	bdil	0.02	bdil	bdil	0.03	bdil	bdil	0.02	bdil	0.23	0.10	0.10	0.05	0.13	0.18	0.18	0.08	0.08	bdil	bdil	bdil	bdil	bdil	bdil	bdil	bdil	bdil	bdil	bdil	bdil	bdil	bdil	bdil	bdil	bdil	bdil	bdil	bdil	bdil	bdil	bdil	bdil	bdil	bdil	bdil	bdil	bdil	bdil	bdil	bdil	bdil				
Y ₂ O ₃	0.26	0.27	0.36	0.39	0.35	0.19	0.35	0.57	3.17	0.90	4.74	0.62	4.73	0.47	0.68	6.27	0.14	0.69	2.17	0.12	1.03	0.62	1.66	0.53	0.95	2.46	0.49	0.54	1.49	0.58	0.56	1.08	0.56	0.51	0.34	3.92	0.62	0.83	1.04	0.80	0.69	0.89	0.37	1.50	0.31	0.30	0.30	0.29	0.35	1.79													
P ₂ O ₅	bdil	bdil	bdil	bdil	0.06	0.06	0.08	0.05	0.20	0.14	0.25	0.09	0.14	0.05	0.12	0.28	0.08	0.17	bdil	bdil	bdil	bdil	bdil	bdil	bdil	bdil	bdil	bdil	bdil	bdil	bdil	bdil	bdil	bdil	bdil	bdil	bdil	bdil	bdil	bdil	bdil	bdil	bdil	bdil	bdil	bdil	bdil	bdil	bdil	bdil	bdil	bdil	bdil	bdil	bdil	bdil	bdil	bdil	bdil				
Total	97.79	99.57	97.46	97.68	97.79	98.17	98.32	98.83	95.45	96.49	90.26	96.64	88.36	98.37	98.12	85.12	92.87	98.41	85.16	72.38	95.25	94.36	93.66	95.67	90.38	91.21	94.07	91.29	92.26	94.89	93.20	93.37	93.32	91.12	94.47	90.51	95.26	96.76	92.28	97.50	94.87	95.10	97.83	93.19	93.87	94.32	94.89	94.07	94.96	92.70	92.85												

Sample	Type-(II) Pegmatite (Cont.)																															
	AS-MR38-04 Zircon 1				AS-MR38-04 Zircon 3				AS-MR38-04 Zircon 4				AS-MR38-04 Zircon 5				AS-MR38-05 Zircon 1		AS-MR38-05 Zircon 2		AS-MR38-05 Zircon 3		AS-MR38-05 Zircon 4		AS-MR38-07 Zircon 1		AS-MR38-07 Zircon 2		AS-MR38-07 Zircon 3		AS-MR38-07 Zircon 4	
Wt%O	29.03	31.11	30.78	25.60	31.47	32.65	32.65	32.61	31.34	31.48	32.81	32.99	31.71	31.72	30.26	29.50	30.12	30.51	30.14	29.98	27.98	30.47	30.79	29.37	29.41	29.87	30.38	30.49	29.68	27.70	28.95	
SiO ₂	54.97	57.30	56.42	54.40	57.14	58.45	58.21	57.83	57.56	59.49	57.30	57.76	59.21	57.20	62.30	59.31	60.69	62.59	63.21	61.10	52.14	59.36	57.63	61.04	55.68	59.99	58.28	56.93	56.66	52.81	53.31	
Al ₂ O ₃	0.83	0.36	0.59	1.28	0.53	0.46	0.51	0.48	0.51	0.38	0.37	0.53	0.33	0.49	bdl	bdl	bdl	bdl	bdl	bdl	0.71	0.43	0.62	bdl	0.75	0.20	0.08	0.22	0.65	0.84	0.78	
MgO	bdl	bdl	bdl	bdl	bdl	bdl	bdl	bdl	bdl	bdl	bdl	bdl	bdl	bdl	bdl	bdl	bdl	bdl	bdl	bdl	0.01	bdl	bdl	bdl	bdl	bdl	bdl	bdl	0.02	0.01	0.01	
ThO ₂	0.28	bdl	0.06	0.63	0.06	0.06	bdl	0.05	bdl	bdl	bdl	bdl	0.05	bdl	bdl	bdl	0.05	bdl	bdl	bdl	0.72	bdl	0.19	bdl	0.19	bdl	0.06	bdl	0.64	1.09	0.98	
UO ₂	0.13	bdl	bdl	0.21	bdl	bdl	bdl	bdl	bdl	bdl	bdl	bdl	bdl	bdl	bdl	bdl	bdl	bdl	bdl	bdl	bdl	bdl	bdl	bdl	bdl	bdl	bdl	bdl	bdl	bdl	bdl	
SnO ₂	0.79	0.82	0.75	0.68	0.83	0.80	0.83	0.81	0.87	1.20	0.89	0.72	1.18	0.81	1.86	2.36	1.50	2.33	2.18	1.14	0.33	0.86	1.18	1.72	1.07	1.02	1.87	0.95	0.26	0.28	0.26	
CaO	0.50	0.06	0.09	0.92	0.07	0.28	0.09	0.15	0.17	0.10	0.06	0.09	0.08	0.09	0.06	0.03	0.18	0.01	0.03	0.30	0.39	0.14	0.08	0.05	0.14	0.15	0.09	0.07	0.30	0.29	0.29	
HfO ₂	3.15	3.58	3.63	3.23	3.84	3.73	3.90	3.74	3.82	1.87	5.48	3.64	1.93	3.75	2.33	3.87	3.78	2.28	1.98	3.12	3.63	3.01	3.66	3.14	2.93	3.59	4.59	3.86	3.50	3.18	3.96	
Yb ₂ O ₃	0.21	0.53	0.35	0.44	0.34	0.10	0.07	0.11	0.07	0.08	0.05	0.05	0.06	0.08	0.05	0.10	0.11	0.05	0.08	0.05	0.99	0.14	0.17	0.11	0.18	0.12	0.26	0.49	0.90	1.53	1.14	
Er ₂ O ₃	0.16	0.08	0.07	0.38	0.08	0.03	0.04	0.07	0.03	bdl	0.03	0.05	bdl	0.04	0.03	0.03	0.07	bdl	0.02	0.03	0.55	bdl	0.03	bdl	0.04	bdl	0.09	0.10	0.50	0.87	0.65	
Gd ₂ O ₃	0.05	bdl	bdl	0.26	bdl	bdl	bdl	bdl	bdl	bdl	bdl	bdl	bdl	bdl	bdl	bdl	bdl	bdl	bdl	bdl	0.17	bdl	bdl	bdl	bdl	bdl	bdl	bdl	0.12	0.22	0.16	
Dy ₂ O ₃	0.33	0.22	0.17	0.68	0.21	0.19	0.22	0.23	0.18	0.17	0.18	0.17	0.23	0.20	bdl	bdl	0.04	bdl	0.02	0.02	0.51	0.28	0.27	0.02	0.31	0.11	0.12	0.14	0.42	0.68	0.56	
FeO	0.77	0.33	0.31	0.92	0.35	0.35	0.40	0.36	0.47	0.29	0.41	0.52	0.34	0.44	bdl	bdl	bdl	bdl	bdl	bdl	0.81	0.49	0.22	0.06	1.21	0.05	0.16	0.13	0.56	0.87	0.73	
Sm ₂ O ₃	bdl	bdl	bdl	bdl	bdl	bdl	bdl	bdl	bdl	bdl	bdl	bdl	bdl	bdl	bdl	bdl	bdl	bdl	bdl	bdl	bdl	bdl	bdl	bdl	bdl	bdl	bdl	bdl	bdl	bdl	bdl	
MnO	0.45	0.60	0.61	0.22	0.68	0.76	0.77	0.70	0.69	0.68	0.60	0.64	0.67	0.73	bdl	bdl	bdl	bdl	0.02	0.03	0.29	0.98	0.84	0.08	1.04	0.36	0.23	0.22	0.34	0.29	0.29	
Pr ₂ O ₃	bdl	bdl	bdl	bdl	bdl	bdl	bdl	bdl	bdl	bdl	bdl	bdl	bdl	bdl	bdl	bdl	bdl	bdl	bdl	bdl	bdl	bdl	bdl	bdl	bdl	bdl	bdl	bdl	bdl	bdl	bdl	
Nd ₂ O ₃	0.04	bdl	bdl	0.05	bdl	bdl	bdl	bdl	bdl	bdl	bdl	bdl	bdl	bdl	bdl	bdl	bdl	bdl	bdl	bdl	bdl	bdl	bdl	bdl	bdl	bdl	bdl	bdl	bdl	bdl	bdl	
Ce ₂ O ₃	0.04	bdl	bdl	0.07	bdl	bdl	bdl	bdl	bdl	bdl	bdl	bdl	bdl	bdl	bdl	bdl	bdl	bdl	bdl	bdl	bdl	bdl	bdl	bdl	bdl	bdl	bdl	bdl	bdl	bdl	0.03	bdl
Y ₂ O ₃	1.20	0.19	0.12	3.10	0.13	0.09	0.09	0.20	0.11	0.06	0.06	0.10	0.08	0.09	0.06	0.07	0.12	0.08	0.13	0.05	2.95	0.05	0.66	bdl	0.73	0.03	0.48	1.67	2.66	3.61	3.20	
P ₂ O ₅	bdl	bdl	bdl	bdl	bdl	bdl	bdl	bdl	bdl	bdl	bdl	bdl	bdl	bdl	bdl	bdl	bdl	bdl	bdl	bdl	0.78	0.38	0.26	bdl	0.30	0.27	0.05	0.06	0.81	1.15	0.90	
TOTAL	92.90	95.02	93.80	93.10	95.60	97.76	97.68	97.22	95.64	95.69	98.10	97.14	95.79	95.50	96.80	95.10	96.40	97.61	97.71	95.56	92.88	96.45	96.50	95.35	93.88	95.49	96.55	95.27	97.81	95.45	96.13	

Sample	Type-(II) Pegmatite (Cont.)																																																																																																																																																																																																																																																																																																																																																																																																																																																																																																																																																																																																																																																																																																																																																																																																																																																																																																																																
	AS-MR38-08 Zircon 1				AS-MR38-08 Zircon 2				AS-MR38-08 Zircon 3				AS-MR38-08 Zircon 4				AS-MR38-08 Zircon 5				AS-MR38-09 Zircon 1				AS-MR38-09 Zircon 2				AS-MR38-09 Zircon 3				AS-MR38-09 Zircon 5				AS-MR38-10 Zircon 1				AS-MR38-10 Zircon 2				AS-MR38-10 Zircon 3																																																																																																																																																																																																																																																																																																																																																																																																																																																																																																																																																																																																																																																																																																																																																																																																																																																																																				
Wt%O	30.40	30.57	29.36	30.42	30.60	30.44	29.97	29.44	31.26	30.38	30.32	31.23	30.46	30.96	31.43	30.90	31.42	31.48	30.97	30.63	31.20	30.81	29.24	30.69	29.44	29.93	29.87	29.89	29.50	29.73	29.56	29.61	29.20	30.41	30.13	30.18	29.84	30.66	30.23	30.14	29.26	32.37	32.35	32.45	32.44	32.18	32.30	31.68	31.41	32.17	32.32	32.40	32.57	32.24	32.90	32.30	32.70	32.44	32.00	32.37																																																																																																																																																																																																																																																																																																																																																																																																																																																																																																																																																																																																																																																																																																																																																																																																																																																																					
SiO ₂	56.01	56.99	55.14	55.57	55.72	55.70	55.09	55.38	56.84	55.69	55.43	58.41	55.13	58.22	58.39	58.72	57.54	57.45	57.73	57.72	58.68	56.94	53.39	57.49	54.82	54.20	53.72	54.01	53.75	54.06	54.12	53.41	53.72	55.20	55.08	54.46	55.19	56.86	55.76	54.09	63.10	63.44	63.17	63.24	63.65	63.84	61.37	60.19	63.27	63.99	61.45	65.03	62.80	64.21	64.96	64.93	62.81	62.18	61.61																																																																																																																																																																																																																																																																																																																																																																																																																																																																																																																																																																																																																																																																																																																																																																																																																																																																						
Al ₂ O ₃	0.73	0.74	0.75	0.72	0.70	0.69	0.67	0.67	0.14	0.63	0.67	0.21	0.64	0.65	0.67	0.65	0.64	0.63	0.59	0.27	0.65	0.13	0.90	0.68	0.85	0.85	0.85	0.88	0.75	0.83	0.80	0.77	0.86	0.79	0.85	0.76	0.86	0.80	0.80	0.79	0.80	bdl	bdl	bdl	bdl	bdl	bdl	bdl	bdl	bdl	bdl	bdl	bdl	bdl	bdl	bdl	bdl	bdl	bdl	bdl	bdl	bdl	bdl	bdl	bdl	bdl	bdl	bdl	bdl	bdl	bdl	bdl	bdl	bdl	bdl	bdl	bdl	bdl	bdl	bdl	bdl	bdl	bdl	bdl	bdl	bdl	bdl	bdl	bdl	bdl	bdl	bdl	bdl	bdl	bdl	bdl	bdl	bdl	bdl	bdl	bdl	bdl	bdl	bdl	bdl	bdl	bdl	bdl	bdl	bdl	bdl	bdl	bdl	bdl	bdl	bdl	bdl	bdl	bdl	bdl	bdl	bdl	bdl	bdl	bdl	bdl	bdl	bdl	bdl	bdl	bdl	bdl	bdl	bdl	bdl	bdl	bdl	bdl	bdl	bdl	bdl	bdl	bdl	bdl	bdl	bdl	bdl	bdl	bdl	bdl	bdl	bdl	bdl	bdl	bdl	bdl	bdl	bdl	bdl	bdl	bdl	bdl	bdl	bdl	bdl	bdl	bdl	bdl	bdl	bdl	bdl	bdl	bdl	bdl	bdl	bdl	bdl	bdl	bdl	bdl	bdl	bdl	bdl	bdl	bdl	bdl	bdl	bdl	bdl	bdl	bdl	bdl	bdl	bdl	bdl	bdl	bdl	bdl	bdl	bdl	bdl	bdl	bdl	bdl	bdl	bdl	bdl	bdl	bdl	bdl	bdl	bdl	bdl	bdl	bdl	bdl	bdl	bdl	bdl	bdl	bdl	bdl	bdl	bdl	bdl	bdl	bdl	bdl	bdl	bdl	bdl	bdl	bdl	bdl	bdl	bdl	bdl	bdl	bdl	bdl	bdl	bdl	bdl	bdl	bdl	bdl	bdl	bdl	bdl	bdl	bdl	bdl	bdl	bdl	bdl	bdl	bdl	bdl	bdl	bdl	bdl	bdl	bdl	bdl	bdl	bdl	bdl	bdl	bdl	bdl	bdl	bdl	bdl	bdl	bdl	bdl	bdl	bdl	bdl	bdl	bdl	bdl	bdl	bdl	bdl	bdl	bdl	bdl	bdl	bdl	bdl	bdl	bdl	bdl	bdl	bdl	bdl	bdl	bdl	bdl	bdl	bdl	bdl	bdl	bdl	bdl	bdl	bdl	bdl	bdl	bdl	bdl	bdl	bdl	bdl	bdl	bdl	bdl	bdl	bdl	bdl	bdl	bdl	bdl	bdl	bdl	bdl	bdl	bdl	bdl	bdl	bdl	bdl	bdl	bdl	bdl	bdl	bdl	bdl	bdl	bdl	bdl	bdl	bdl	bdl	bdl	bdl	bdl	bdl	bdl	bdl	bdl	bdl	bdl	bdl	bdl	bdl	bdl	bdl	bdl	bdl	bdl	bdl	bdl	bdl	bdl	bdl	bdl	bdl	bdl	bdl	bdl	bdl	bdl	bdl	bdl	bdl	bdl	bdl	bdl	bdl	bdl	bdl	bdl	bdl	bdl	bdl	bdl	bdl	bdl	bdl	bdl	bdl	bdl	bdl	bdl	bdl	bdl	bdl	bdl	bdl	bdl	bdl	bdl	bdl	bdl	bdl	bdl	bdl	bdl	bdl	bdl	bdl	bdl	bdl	bdl	bdl	bdl	bdl	bdl	bdl	bdl	bdl	bdl	bdl	bdl	bdl	bdl	bdl	bdl	bdl	bdl	bdl	bdl	bdl	bdl	bdl	bdl	bdl	bdl	bdl	bdl	bdl	bdl	bdl	bdl	bdl	bdl	bdl	bdl	bdl	bdl	bdl	bdl	bdl	bdl	bdl	bdl	bdl	bdl	bdl	bdl	bdl	bdl	bdl	bdl	bdl	bdl	bdl	bdl	bdl	bdl	bdl	bdl	bdl	bdl	bdl	bdl	bdl	bdl	bdl	bdl	bdl	bdl	bdl	bdl	bdl	bdl	bdl	bdl	bdl	bdl	bdl	bdl	bdl	bdl	bdl	bdl	bdl	bdl	bdl	bdl	bdl	bdl	bdl	bdl	bdl	bdl	bdl	bdl	bdl	bdl	bdl	bdl	bdl	bdl	bdl	bdl	bdl	bdl	bdl	bdl	bdl	bdl	bdl	bdl	bdl	bdl	bdl	bdl	bdl	bdl	bdl	bdl	bdl	bdl	bdl	bdl	bdl	bdl	bdl	bdl	bdl	bdl	bdl	bdl	bdl	bdl	bdl	bdl	bdl	bdl	bdl	bdl	bdl	bdl	bdl	bdl	bdl	bdl	bdl	bdl	bdl	bdl	bdl	bdl	bdl	bdl	bdl	bdl	bdl	bdl	bdl	bdl	bdl	bdl	bdl	bdl	bdl	bdl	bdl	bdl	bdl	bdl	bdl	bdl	bdl	bdl	bdl	bdl	bdl	bdl	bdl	bdl	bdl	bdl	bdl	bdl	bdl	bdl	bdl	bdl	bdl	bdl	bdl	bdl	bdl	bdl	bdl	bdl	bdl	bdl	bdl	bdl	bdl	bdl	bdl	bdl	bdl	bdl	bdl	bdl	bdl	bdl	bdl	bdl	bdl	bdl	bdl	bdl	bdl	bdl	bdl	bdl	bdl	bdl	bdl	bdl	bdl	bdl	bdl	bdl	bdl	bdl	bdl	bdl	bdl	bdl	bdl	bdl	bdl	bdl	bdl	bdl	bdl	bdl	bdl	bdl	bdl	bdl	bdl	bdl	bdl	bdl	bdl	bdl	bdl	bdl	bdl	bdl	bdl	bdl	bdl	bdl	bdl	bdl	bdl	bdl	bdl	bdl	bdl	bdl	bdl	bdl	bdl	bdl	bdl	bdl	bdl	bdl	bdl	bdl	bdl	bdl	bdl	bdl	bdl	bdl	bdl	bdl	bdl	bdl	bdl	bdl	bdl	bdl	bdl	bdl	bdl	bdl	bdl	bdl	bdl	bdl	bdl	bdl	bdl	bdl	bdl	bdl	bdl	bdl	bdl	bdl	bdl	bdl	bdl	bdl	bdl	bdl	bdl	bdl	bdl	bdl	bdl	bdl	bdl	bdl	bdl	bdl	bdl	bdl	bdl	bdl	bdl	bdl	bdl	bdl	bdl	bdl	bdl	bdl	bdl	bdl	bdl	bdl	bdl	bdl	bdl	bdl	bdl	bdl	bdl	bdl	bdl	bdl	bdl	bdl	bdl	bdl	bdl	bdl	bdl	bdl	bdl	bdl	bdl	bdl	bdl	bdl	bdl	bdl	bdl	bdl	bdl	bdl	bdl	bdl	bdl	bdl	bdl	bdl	bdl	bdl	bdl	bdl	bdl	bdl	bdl	bdl	bdl	bdl	bdl	bdl	bdl	bdl	bdl	bdl	bdl	bdl	bdl	bdl	bdl	bdl	bdl	bdl	bdl	bdl	bdl	bdl	bdl	bdl	bdl	bdl	bdl	bdl	bdl	bdl	bdl	bdl	bdl	bdl	bdl	bdl	bdl	bdl	bdl	bdl	bdl	bdl	bdl	bdl	bdl	bdl	bdl	bdl	bdl	bdl	bdl	bdl	bdl	bdl	bdl	bdl	bdl	bdl	bdl	bdl	bdl	bdl	bdl	bdl	bdl	bdl	bdl	bdl	bdl	bdl	bdl	bdl	bdl	bdl	bdl	bdl	bdl	bdl	bdl	bdl	bdl	bdl	bdl	bdl	bdl	bdl	bdl	bdl	bdl	bdl	bdl	bdl	bdl	bdl	bdl	bdl	bdl	bdl	bdl

APPENDIX B
ADDITIONAL BRIGHT PHASE SCANS

